

University of Windsor

Scholarship at UWindor

Electronic Theses and Dissertations

Theses, Dissertations, and Major Papers

2012

The Quantitative Assessment of Retained Austenite in Induction Hardened Ductile Iron

Hao Ma

University of Windsor

Follow this and additional works at: <https://scholar.uwindsor.ca/etd>

Recommended Citation

Ma, Hao, "The Quantitative Assessment of Retained Austenite in Induction Hardened Ductile Iron" (2012). *Electronic Theses and Dissertations*. 197.

<https://scholar.uwindsor.ca/etd/197>

This online database contains the full-text of PhD dissertations and Masters' theses of University of Windsor students from 1954 forward. These documents are made available for personal study and research purposes only, in accordance with the Canadian Copyright Act and the Creative Commons license—CC BY-NC-ND (Attribution, Non-Commercial, No Derivative Works). Under this license, works must always be attributed to the copyright holder (original author), cannot be used for any commercial purposes, and may not be altered. Any other use would require the permission of the copyright holder. Students may inquire about withdrawing their dissertation and/or thesis from this database. For additional inquiries, please contact the repository administrator via email (scholarship@uwindsor.ca) or by telephone at 519-253-3000ext. 3208.

The Quantitative Assessment of Retained Austenite
in Induction Hardened Ductile Iron

by
Hao Ma

A Thesis
Submitted to the Faculty of Graduate Studies
through Engineering Materials
in Partial Fulfillment of the Requirements for
the Degree of Master of Applied Science at the
University of Windsor

Windsor, Ontario, Canada

2012

© 2012 Hao Ma

The Quantitative Assessment of Retained Austenite
in Induction Hardened Ductile Iron

by

Hao Ma

APPROVED BY:

C. Rangan, Outside Program Reader
Department of Physics

V. Stoilov, Program Reader
Department of Mechanical, Automotive, and Materials Engineering

R. Bowers, Co-Advisor
Department of Mechanical, Automotive, and Materials Engineering

D.O. Northwood, Co-Advisor
Department of Mechanical, Automotive, and Materials Engineering

Xichen Sun, Industrial Advisor
Chrysler LLC, CTC

N.Zamani, Chair of Defence
Department of Mechanical, Automotive, and Materials Engineering

18 May 2012

AUTHOR'S DECLARATION OF ORIGINALITY

I hereby certify that I am the sole author of this thesis and that no part of this thesis has been published or submitted for publication.

I certify that, to the best of my knowledge, my thesis does not infringe upon anyone's copyright nor violate any proprietary rights and that any ideas, techniques, quotations, or any other material from the work of other people included in my thesis, published or otherwise, are fully acknowledged in accordance with the standard referencing practices. Furthermore, to the extent that I have included copyrighted material that surpasses the bounds of fair dealing within the meaning of the Canada Copyright Act, I certify that I have obtained a written permission from the copyright owner(s) to include such material(s) in my thesis and have included copies of such copyright clearances to my appendix.

I declare that this is a true copy of my thesis, including any final revisions, as approved by my thesis committee and the Graduate Studies office, and that this thesis has not been submitted for a higher degree to any other University or Institution.

ABSTRACT

This study focused on induction hardened ductile iron which has a variability in both the microstructure of the surface hardened case, principally the amount of retained austenite (RA), and the level of residual stress (RS). Retained austenite and residual stress can have a significant effect on mechanical properties. In order to determine what level of retained austenite is acceptable, it will need to be measured by an acceptable metallographic procedure and through the use of X-ray diffraction (XRD), although XRD has proven much more accurate in assessment than optical metallography, However, because of the complexity as well as availability of the XRD equipment, it is not well suited to analysis of camshafts during high volume manufacture or heat treatment of camshafts. Therefore, an acceptable correlation is needed between the two methods of measurement. During this study a correlation has been obtained between the RA values obtained by x-ray diffraction with those obtained by optical metallography. This data for ductile iron expands the database that was available for steels to higher carbon-content ferrous alloys. Finally, a correlation is made between RA content and RS level in order to define a robust process window.

DEDICATION

This thesis is dedicated to Dr. Derek O Northwood and Dr. Randy J Bowers, who have always provided generous help and encouraged me to strive for excellence during my study period.

ACKNOWLEDGEMENTS

First I would like to thank my advisor Dr. Derek O. Northwood and co-advisor Dr. Randy Bowers for their careful supervision and strict requirement towards my M.A.Sc degree. Also to my committee members, Dr. Vesselin Stoilov and Dr. Chitra Rangan who provided valuable knowledge and guidance for this research.

Secondly, I would like to acknowledge Dr Xichen Sun and Peter J.Bauerle from the Chrysler LLC Technology Center, for the testing, camshafts casting and heating facilities.

Thirdly, I would also like to acknowledge Mr Andy Jenner, Matt Louise and Gang Li for their remarkable and generous support at the University of Windsor laboratories. Also I would particularly like to thank my dear friend Zaidao Yang for his help in experiments and literature reviews.

Finally I would like to mention Dr. Derek O. Northwood, Dr. Randy J Bowers and University of Windsor graduate scholarships for financial support for my M.A.Sc degree.

TABLE OF CONTENTS

AUTHOR’S DECLARATION OF ORIGINALITY	iii
ABSTRACT.....	iv
DEDICATION	v
ACKNOWLEDGEMENTS	vi
LIST OF TABLES	x
LIST OF FIGURES	xi
LIST OF ABBREVIATIONS.....	xv
CHAPTER I: INTRODUCTION	1
1.1 Motivation:	2
1.2 Research Scope:	4
CHAPTER II: LITERATURE REVIEW	5
2.1 Steel.....	5
2.2 Cast Irons	7
2.2.1 Gray Cast Iron.....	8
2.2.2 White Cast Iron	10
2.2.3 Mottled Cast Iron	11
2.2.4 Malleable Cast Iron.....	12
2.2.5 Ductile (Nodular) Cast Iron	12
2.2.6 Austempered Ductile Iron (ADI)	13
2.3 Induction Hardening Ductile Iron (IHDI).....	16
2.4 Theoretical Background of Induction Heating.....	16
2.4.1 Electromagnetic Phenomena:.....	16
2.4.2 Skin Effect:	17
2.4.3 Electromagnetic Proximity Effect:	19
2.4.4 Electromagnetic Ring Effect:.....	20
2.4.5 Thermal Phenomena and Dynamics in Induction Heating	21
2.4.6 Quenching after Induction Hardening.....	22
2.5 Applications of Induction Heat Treatment	24
2.6 Fast cooling of Austenite:	26

2.6.1	Time-Temperature-Transformation (TTT) Diagram	26
2.6.2	Continuous Cooling Transformation (CCT) Diagram	27
2.6.3	Microstructures Produced During Cooling:	28
2.7	Residual Stress and Induction Hardening	31
2.8	Retained Austenite and Residual Stress Measurement	34
2.9	Previous Studies:	37
CHAPTER III: EXPERIMENTAL DETAILS		43
3.1	Overview of the Experimental Procedures and Measurements:	43
3.2	Material and Casting:	44
3.2.1	Casting Details:	45
3.2.2	Microstructure of as-cast samples:	46
3.3	Induction Hardening:	46
3.4	Sample Preparation:	47
3.5	Measurement of Retained Austenite (RA) and Residual Stress (RS) by XRD	48
3.5.1	Residual Stress Measurement:	48
3.5.2	Retained Austenite Measurement	49
3.6	Metallography:	50
3.7	Image Analysis:	53
3.8	Hardness Test:	56
CHAPTER IV: MICROSTRUCTURE CHARACTERIZATION		57
4.1	Graphite Content:	57
4.2	Induction Hardened Ductile Iron Microstructures:	59
4.3	Retained Austenite Analysis:	70
4.4	Summary	73
CHAPTER V: ANALYSIS OF RELATIONSHIPS BETWEEN RA, RS AND HARDNESS		74
5.1	RA and RS by XRD:	74
5.2	Relationship between RS (XRD) and RA by Optical Microscopy	80
5.3	Relationship between RA Values Obtained From OM and XRD	82
5.4	Relationship between Hardness and RA content	85

CHAPTER VI:CONCLUSIONS AND RECOMMENDATIONS.....	88
6.1 Recommendations for Future Work:	90
REFERENCES	92
VITA AUCTORIS	98
PUBLICATIONS AND PRESENTATIONS	99

LIST OF TABLES

Table 2. 1 Typical induction hardened parts and applications [27]	24
Table 2. 2 Etchant used in previous studies [12]	38
Table 3. 1 Chemical composition (Wt. %) of induction hardened ductile iron	44
Table 4. 1 Graphite content of 18 samples by image analysis	58
Table 4. 2 Volume % retained austenite for 18 samples by OM.	70
Table 5. 1 RA content for 18 samples measured by laboratories A and B	74
Table 5. 2 RS for 18 samples measured by laboratories A and B	76
Table 5. 3 RS/RA ratios for all 18 samples of lab A and B	79
Table 5. 4 Macrohardness values (HRC) for all the 18 samples.	85

LIST OF FIGURES

Figure 2.1 The iron-carbon diagram [14].....	6
Figure 2.2 Classification of cast iron [19]	8
Figure 2.3 Pearlitic gray cast iron 4% picral etch.500X [9]	9
Figure 2.4 Pearlitic white cast iron, 4% picral etch. 250X [9].....	10
Figure 2.5 Mottled pearlitic cast iron. 4% picral etch. 250X [9]	11
Figure 2.6 Pearlitic malleable cast iron. 4% picral. 500X [9].....	12
Figure 2.7 Pearlitic ductile (nodular) cast iron. 4% Picral. 500X[9].	13
Figure 2.8 ADI ausferrite microstructure[25]	14
Figure 2.9 Schematic representation of a) ductile cast iron, b) ADI [25].....	15
Figure 2.10 A conventional induction heating system consists of a cylindrical steel bar surrounded by a multi-turn induction coil [27].....	17
Figure 2.11 Distribution of magnetic field intensity (H) and relative magnetic permeability (μ_r) along the radius of a homogeneous carbon steel cylinder [2]	18
Figure 2.12 Current density distributions because of skin effect [2]	19
Figure 2.13 Current distribution in bus bars due to proximity effect [2].....	20
Figure 2.14 Ring effect in round conductors [2].....	20
Figure 2.15 Effect of selected quenchants on the cooling curves of a 25.4 mm diam steel bar. All quenchants flowing at 0.5 m/s [27].....	23
Figure 2.16 Various commercial applications of induction hardening ductile iron a) gears b) sprockets c) engine blocks d) camshafts.....	25
Figure 2.17 Typical TTT curve for low-silicon ductile iron[42]	27
Figure 2.18 Continuous Cooling Transformation (CCT) diagram of a low-alloyed ductile iron[43]	28
Figure 2.19 Microstructure of induction hardening ductile iron camshaft showing (a) needle-like martensite (b) white retained austenite.....	30

Figure 2.20 Stresses at the surface of a carbon steel cylinder during heating and quenching. Martensite formation results in a final compressive residual stress state [27].	31
Figure 2.21 Typical hardness and residual stress profile in induction-hardened 1045 steel[27]	33
Figure 2.22 Definition of the axis and the direction of residual stress measurement[58]	33
Figure 2.23 Carburized X-ray specimen of EX 32, 0.100 mm case depth 2 pct nital +zelphiran chloride (a) optical micrograph (b) electron micrograph. Surface martensite is the light-etching lenticular microconstituent in (a) and the untempered, carbon-free lenticular microconstituent in (b).....	39
Figure 2.24 Measurement of retained austenite, metallography vs X-ray[12].	40
Figure 2.25 Residual stress and retained austenite distributions in as-carburized and shot peened carburized steel[64]	41
Figure 3.1 Effect of alloying elements on the microstructure of cast iron[65].....	45
Figure 3.2 Microstructure of as-cast ductile iron sample.....	46
Figure 3.3 Induction hardening of ductile iron camshaft.....	47
Figure 3.4 Profile of ductile iron camshaft	47
Figure 3.5 Shape and geometry of camshaft lobe, (a) sample B2 with mark X to indicate the position for RA and RS measurements; (b) cam lobe dimensions and geometry; (c) Dimension and geometry of cam lobe section.....	48
Figure 3.6 The measurement of residual stress using X-ray Diffraction Method	49
Figure 3.7 XRD pattern for retained austenite measurements	50
Figure 3.8 Optical microscope with a digital imaging system.....	51
Figure 3.9 Micrographs showing graphite distribution in the matrix	51
Figure 3.10 Induction hardened lobe 1 (a) 50x (b) 1000x, lobe 2 which shows pearlite clearly (c) 50x (d) 1000x.....	52
Figure 3.11 Steps showing how to determine graphite content (a) open ImagePro-Plus; (b) Import a picture and click Measure-Count/Size;(c) select the color of graphite(dark); (d)select measurement-Per area(Obj./Total); (e)select “count” ; (f) select view-statistics.	54

Figure 3.12 Optical image analysis for graphite nodule percentage. (a) original micrograph which shows graphite distribution in the matrix ; (b) after software processing; the area ratio of the red part in the matrix is calculated.....	55
Figure 3.13 Retained austenite determination: (a) image: 2% Nital etching (b) image analysis.....	56
Figure 3.14 Rockwell hardness testing machine.....	56
Figure 4.1 Micrographs shows graphite distribution in (a) B2 (b) C2, which shows that B2 has a higher graphite density than C2	57
Figure 4.2 Average graphite content for A,B and C camshafts	58
Figure 4.3 Optical micrographs of as-cast samples.	59
Figure 4.4 Optical micrographs of samples containing RA from 7%-9%, a-b) Sample A1, 7.1 % RA, c-d)Sample B1, 8.2%RA e-f)Sample B2, 8.9% RA	61
Figure 4.5 Optical micrographs of samples containing RA from 9%-11%, a-b) Sample A3, 9.8 % RA, c-d)Sample C5, 10.3%RA e-f)Sample B2, 10.9% RA	62
Figure 4.6 Optical micrographs of samples containing RA from 11%-13%, a-b) Sample A5, 11.7 % RA, c-d)Sample C2, 12.3%RA e-f)Sample B2, 12.9% RA.....	63
Figure 4.7 Optical micrographs of samples containing RA from 13%-15%, a-b) Sample B6, 13.7 % RA, c-d)Sample C5, 14.1%RA e-f)Sample C4, 15.0% RA.....	64
Figure 4.8 Optical micrographs of samples containing RA from 15%-17%, a-b) Sample A2, 15.2 % RA, c-d)Sample A3, 16.1%RA e-f)Sample B4, 16.9% RA	65
Figure 4.9 Optical micrographs of samples containing RA from 17%-19%, a-b) Sample B4, 17.8 % RA, c-d)Sample A3, 18.3%RA e-f)Sample A2, 18.9% RA	66
Figure 4.10 Optical micrographs of samples containing RA from 19%-21%, a-b) Sample A2, 19.4 % RA, c-d)Sample A5, 20.6%RA e-f)Sample B4, 21.0% RA	67
Figure 4.11 Optical micrographs of samples containing RA from 21%-23%, a-b) Sample A3, 21.2 % RA, c-d)Sample B4, 22.3%RA e-f)Sample B4, 23.0% RA.....	68
Figure 4.12 Optical micrographs of samples containing RA from 23%-27%, a-b) Sample A3, 23.3 % RA, c-d)Sample B4 , 23.6%RA e-f)Sample B4, 26.1% RA.....	69
Figure 4.13 Average retained austenite content for camshafts A, B and C	70
Figure 4.14 Relationship between average retained austenite content and graphite content in camshaft A, B and C	71

Figure 4.15 (a) RA% of all 18 samples, (b) retained austenite content in three camshafts	72
Figure 5.1 Relationship of RA values measured from two independent laboratories named A and B	75
Figure 5.2 Relationship of RS measured by two independent laboratories A and B.....	76
Figure 5.3 Comparison of RA and RS values between laboratories A and B	77
Figure 5.4 Relationships between RA (XRD) and RS (XRD) for (a) Laboratory A (b) Laboratory B.	78
Figure 5.5 Relationships between RS/RA ratios in laboratories A and B	80
Figure 5.6 The relationship between RS (XRD) and RA (OM) for RS data obtained in (a) Laboratory A (b) Laboratory B.....	81
Figure 5.7 Relationship between RA (XRD) and RA (OM)	83
Figure 5.8 RA (XRD), as calculated using Equation 5.9, as a function of RA (OM)	84
Figure 5.9 Hardness (HRC) of all 18 samples	85
Figure 5.10 Average hardness of camshafts A, B and C	86
Figure 5.11 Relationship between hardness and % RA	87

LIST OF ABBREVIATIONS

AISI	American Iron and Steel Institute
ICAT	Inter Critical Austenitizing Temperature
ASTM	American Society for Testing and Materials
CCR	critical cooling rate
CCT	continuous cooling transformation
CTC	Chrysler LLC Technology Center
TTT	Time-Temperature-Transformation
DBTT	ductile-to-brittle transition temperature
HRC	Rockwell C Hardness
HV	Vickers Hardness
ID	inner diameter
M_s	martensite start temperature
M_f	martensite finish temperature
XRD	x-ray diffraction
YS	yield strength
RA	Retained Austenite
RS	Residual Stress
OM	Optical Metallography
IHDI	Induction Hardened Ductile Iron

CHAPTER I

INTRODUCTION

Ductile iron, previously known as nodular iron or spheroidal-graphite (SG) cast iron, is cast iron in which the graphite is present as nodules. Ductile iron castings are used for many structural applications, particularly those requiring strength and toughness combined with good machinability and low cost [1]. Many applications, such as the camshaft, use cast iron because of its good sliding and wear properties, which are in part a result of the free graphite and porosity.

Induction hardening has become increasingly popular in the last several decades, because it has the ability to create high heat intensity very quickly at well-defined locations, which leads to low process cycle times with repeatable quality [2]. Compared to traditional heat treatment sources, induction heating is not only energy efficient but also environmentally friendly, and, as noted by Bhadeshia [3], is likely to become the process of choice for the surface hardening of bearings.

Since the camshafts are quenched in cooling water directly after induction hardening, martensite will form because of the fast cooling rate. However, the martensite finish temperature is always below the room temperature or the water temperature, so a fully martensitic microstructure will not be obtained. Thus the existence of a noticeable amount of untransformed, or retained, austenite will be unavoidable and a compressive stress will form [3-4]. Retained austenite can have a large effect on mechanical properties [4]. From one perspective, it can improve the contact fatigue life in gears and bearings because contact stresses promote decomposition of the retained austenite [5]. From another perspective, it will reduce the surface hardness and decrease the load-carrying

capacity and wear resistance. It can also introduce dimensional instability during usage [6,7].

There are many ways of measuring retained austenite such as dilatometric and saturation magnetization intensity methods. The current works uses two different methods, namely X-ray diffraction and optical metallography, which are well-established techniques. According to the literature, X-ray diffraction can measure retained austenite contents greater than 1% by volume with excellent precision [8]. However, due to the high cost of X-ray diffraction equipment, optical metallographic methods have been widely used when the retained austenite content exceeds 10%. A comparison of these two particular methods has been a topic of research interest for a long time [9].

1.1 Motivation:

The application of induction hardening ductile iron is a very practical one in the modern industry. Because some components in the automotive or manufacturing industry are usually subjected to very heavy loading, a high hardness surface with a case which is deep, and is capable of handling extremely high loads, is needed. After the induction hardening process, ductile iron usually has a soft core but an extremely tough outer layer, which could give very high fatigue strength.

Given the desired heat treatment procedures, the mechanical and tribological properties of induction hardened ductile iron can be altered over a very wide range by different phase fractions. The phases achievable in induction hardened ductile iron microstructures include retained austenite, martensite, lamellar pearlite, and nodular graphite. With a combination of these phases, induction hardened ductile iron can be made very hard or very tough, or some balance as required for particular applications. For

example, a crankshaft experiences different cycles of stresses and the stress could drive some retained austenite into martensite, which will cause dimensional instability. Thus the amount of retained austenite should be controlled to an acceptable level in order not to adverse dimensional changes. The main advantages of induction hardening ductile iron compared to traditional forged or wrought steel are [10, 11]:

- Twice to three times the fatigue strength compared to conventional ductile irons.
- The hardness, toughness and ductility level is easily obtainable and can be tailored for any specific application.
- Induction heating eliminates the inconsistencies associated with other methods.
- Induction hardened ductile iron exhibits superior sliding wear resistance compared to steel and ductile irons.
- Production rates can be maximized because induction works so quickly.
- The product quality of induction hardened ductile iron is better than ductile iron because the part to be heated never has direct contact with the heating elements.
- Induction hardened ductile iron has an extended fixture life because it rapidly delivers site-specific heat to desired areas of part.
- Induction hardening is environmentally sound and can reduce the energy consumption when compared with other treatments. For instance, this process converts up to 90% of the energy into heat, which is much higher than other treatments.

1.2 Research Scope:

According to Eldis [12], measurement of the retained austenite contents in carburized steels by X-ray diffraction and automated quantitative metallography gives similar results. However, in the literature, there is little data for the comparison of these two different methods for ductile iron.

Previous studies [6] have found a difference of roughly 15% between metallographic results and XRD results in measuring RA content. However, because of the complexity as well as the availability of the XRD equipment, it is not well suited to the analysis of camshafts during high volume manufacture or the heat treatment of camshafts. Therefore, an acceptable correlation is needed between the two methods of measurement, in addition to the development of a formal metallographic procedure for the measurement of retained austenite. A metallographic method should be used for inspection of production parts, with XRD under the guidelines of ASTM Standard E975 being used for further validation. Once this method has been established, the appropriate standard can be modified to reflect a percentage of retained austenite that will not compromise the fatigue properties of the case hardened zone of the camshaft.

CHAPTER II

LITERATURE REVIEW

Although this research is specifically about induction hardened ductile iron, it is necessary to have a basic knowledge of steels and cast iron. A brief introduction to steels and ductile iron, with their microstructures and properties, is given first. This is followed by a more detailed review of the structures, properties, and applications of induction hardened ductile iron.

2.1 Steel

Steel is an alloy made by combining iron and another element, usually carbon. When carbon is used, its content is usually between 0.2% and 1.5% by weight. Carbon and other elements behave as an agent for hardening by preventing dislocations in the iron atom crystal lattice from sliding past one another. Varying the amount of alloying elements and the form of their presence in the steel (solute elements, precipitated phase) controls properties such as the hardness, ductility, and tensile strength of the resulting steel [13].

At least two allotropes of iron occur naturally in bulk form, body-centered cubic (bcc, α , ferrite), face-centered cubic (fcc, γ , austenite). Figure 2.1 shows the Fe-C equilibrium phase diagram up to 6.67 wt% carbon (Fe_3C) [14].

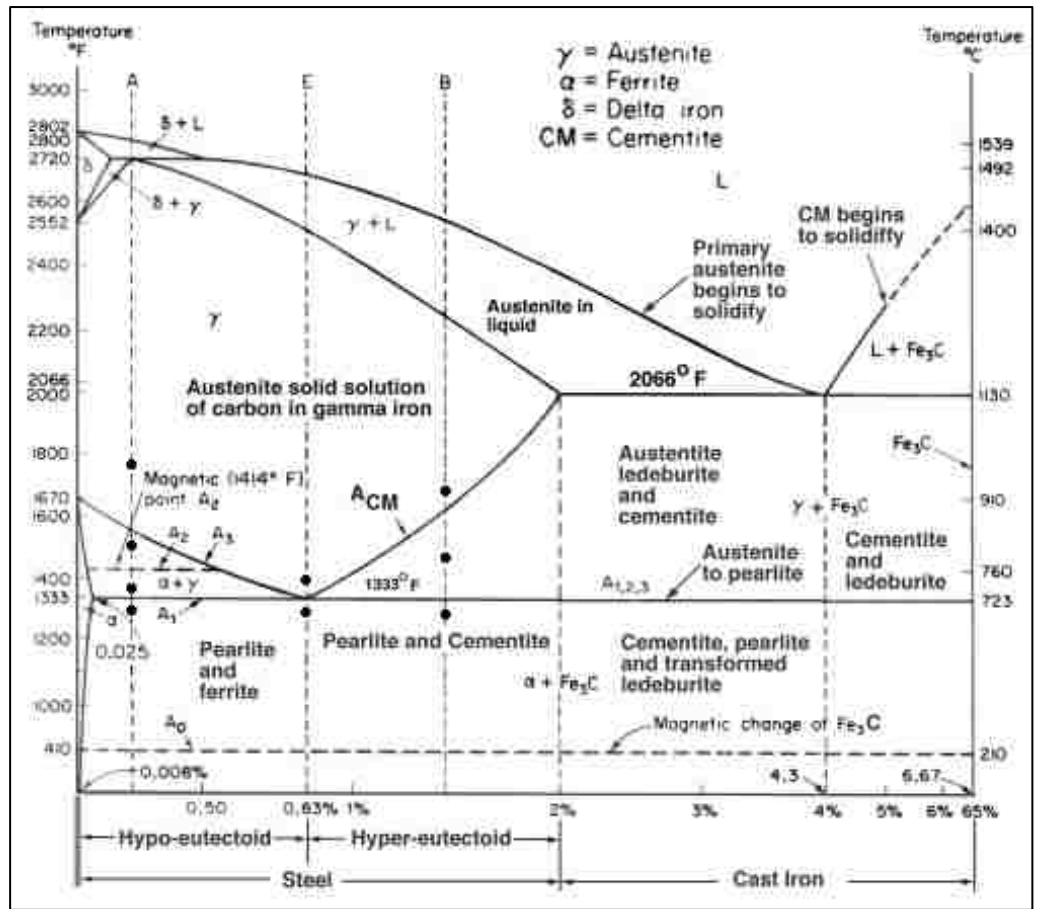


Figure 2.1 The iron-carbon diagram [14]

Austenite is a fcc high-temperature solid solution of carbon in γ -iron and can be retained at room temperature on quenching [14,15]. In quenched steels, with a decrease in cooling rate, several different kinds of phases could be formed: martensite, bainite, pearlite, ferrite and cementite.

Depending upon the carbon content of the parent austenite phase, either lath (low-carbon) or plate (high-carbon) martensite may form, as well as mixtures of the two. In general, lath martensite is associated with high toughness and ductility but low strength, while plate martensite structures have much higher strength but may be rather brittle and non-ductile. Increasing the carbon content of the austenite also depresses the martensite

start (M_s) temperature and the martensite finish (M_f) temperature, which leads to difficulties in converting all of the austenite to martensite. Under this circumstance, retained austenite is present [16].

2.2 Cast Irons

Cast irons, like steels, are essentially alloys of iron and carbon, but they usually contain more than 2% carbon. Cast irons are generally Fe-C-Si alloys that often contain other alloying elements. The induction hardened camshaft also contains Mn, Ni and Cu. The matrix microstructure usually consists of different phases such as nodular graphite, martensite, retained austenite, and ferrite. In practice, most cast irons have carbon contents between 3.0-4.5 wt%, and other additional alloying elements, Most of them should have a Carbon Equivalent content around the eutectic composition after the manufacturing process[17].

Cast iron is usually classified into families according to its graphite morphologies (or shape of the graphite inclusions) [18]. Gray iron, for instance, is grey because it contains flakes of graphite. In contrast, ductile iron contains spheroids of graphite that are nodular shaped. The families of cast irons are shown in Figure 2.2 [19].

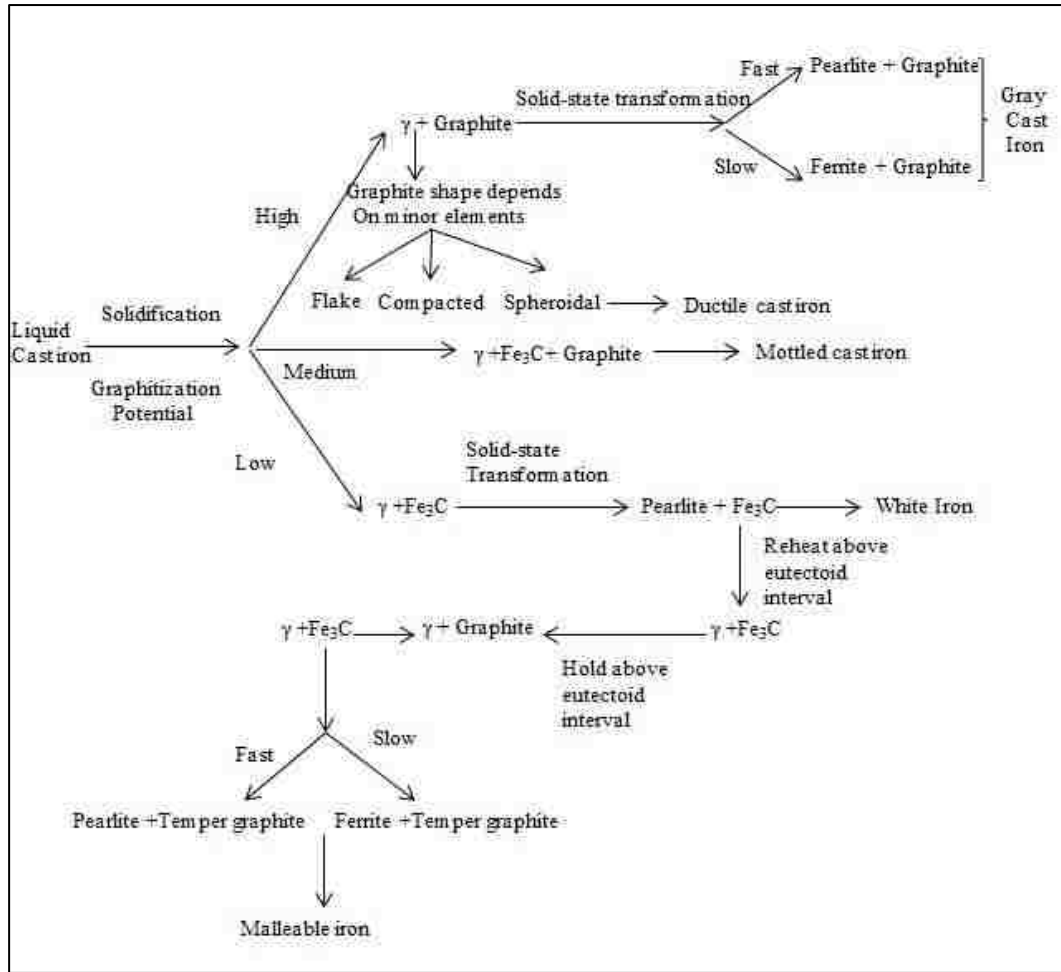


Figure 2.2 Classification of cast iron [19]

2.2.1 Gray Cast Iron

It is very easy to distinguish gray cast iron because of the presence of flake graphite. Usually the graphite flakes are surrounded by pearlite or ferrite or a mixture of both, depending on the heat treatment parameters. In addition, the matrix of heat treated gray iron may also consist of other phases such as bainite or martensite. Figure 2.3 is a typical micrograph of a pearlitic gray iron sample [9].

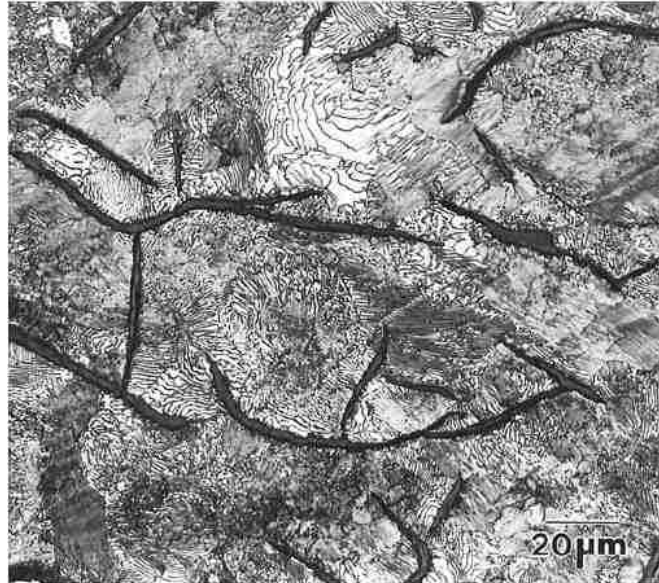


Figure 2.3 Pearlitic gray cast iron 4% picral etch. 500X [9].

It can be seen from Figure 2.3 there are long graphite flakes. The flakes appear to be separate from each other. However, in three dimensions, interconnected graphite flakes can be seen. Due to different manufacturing parameters, various lengths and morphologies of the graphite flakes are observed. The graphite flakes give rise to brittleness in gray cast iron, so it is not useful when it comes to applications involving impact or bending stresses. However, a certain level of flakes imparts a damping capacity, so gray cast iron is very useful in heavy machinery industry, especially for frames or bases. The existence of flake graphite will make the gray cast iron easily machinable [20,21]. Gray cast iron contains 1 to 3% silicon, which promotes the formation of flake graphite.

2.2.2 White Cast Iron

White cast iron has an entirely different microstructure from gray cast iron. Usually there are no graphite flakes in the white cast iron matrix. Figure 2.4 shows the microstructure of white cast iron [9].

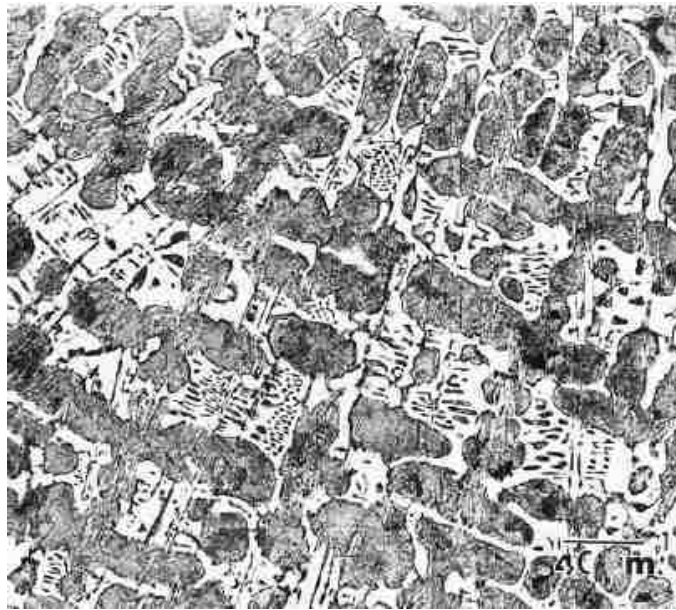


Figure 2.4 Pearlitic white cast iron, 4% picral etch. 250X [9]

It can be seen from Figure 2.4 that there are several different phases in the matrix but no graphite flakes. The larger, rounded dark areas consist of pearlite. The original dendritic structure forms in the solidification process, which results in the aligned array of these areas. Each large, rounded patch of pearlite forms between a branch or arm of a dendrite. The continuous white area is cementite. The other white areas containing small dark pools are ledeburite, which are the eutectic constituents [9]. Usually there is cementite and pearlite in ledeburite: during the solidification, it will form as cementite and austenite.

Depending on the alloy content and cooling rate of the cast iron, these round regions within the ledeburite could also be martensitic. White cast irons usually are brittle,

hard, and difficult to machine because of a significant amount of cementite. White cast irons can be used where wear and abrasion resistance is needed, such as rolls and ore crushing machinery.

2.2.3 Mottled Cast Iron

When there is a mixture of gray and white iron, the cast iron is called mottled cast iron, because it usually has a mottled or speckled appearance on a fracture surface. Figure 2.5 shows a typical microstructure of mottled pearlitic cast iron [9].

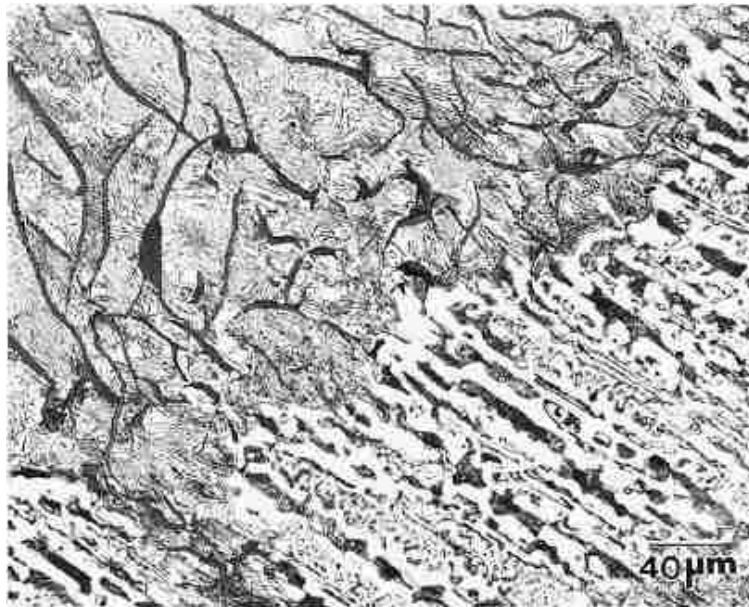


Figure 2.5 Mottled pearlitic cast iron. 4% picral etch. 250 X [9]

When looking at the microstructure, a matrix of pearlite with graphite flakes which is typical microstructure of gray cast iron is seen in the top left. A continuous amount of cementite together with pools of ledeburite and rounded regions of pearlite, which is the typical microstructure of white cast iron, is seen in the bottom right. Usually this kind of cast iron is not desirable in industry because it is actually a transition microstructure between white cast iron and gray cast iron and has undesirable mechanical properties [22].

2.2.4 Malleable Cast Iron

This kind of cast iron cannot be produced in the as-cast form. The only way to produce it is to heat treat white cast irons at a defined temperature and for a sufficient amount of time, so that the cementite in white cast iron is decomposed into carbon. Typical heat treatment procedures are 870 °C to 925 °C for 15 to 24 hours. The microstructure of malleable cast iron is shown in Figure 2.6 [9].

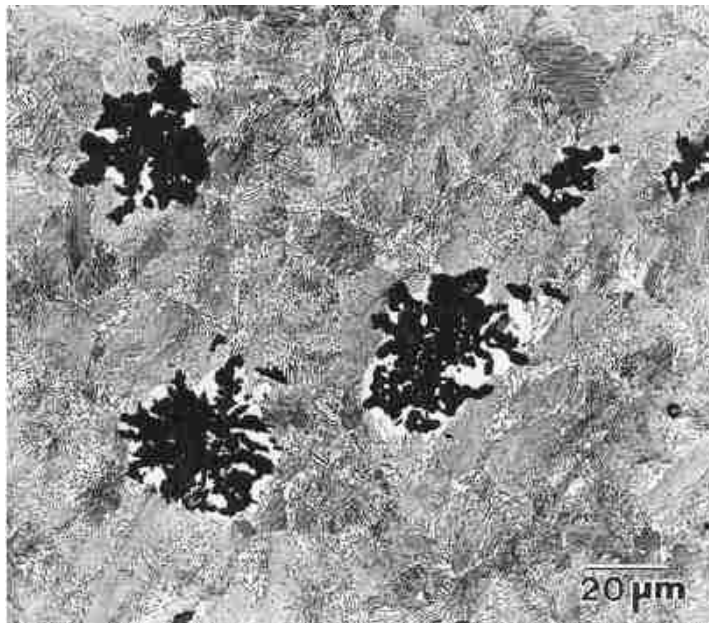


Figure 2.6 Pearlitic malleable cast iron. 4% picral. 500X [9].

Here the irregular-shaped dark areas are called “temper carbon”, which is actually graphite distributed in a pearlite matrix. It forms because of the decomposition of cementite in the original white iron, which decomposes into iron and carbon (graphite) [9,22].

2.2.5 Ductile (Nodular) Cast Iron

With the inoculation of magnesium and cerium during the production process for cast iron, the graphite will assume a nodular or spherical form. Mg and Ce act as nuclei for the graphite. A typical microstructure of ductile cast iron is shown in Figure 2.7 [9].

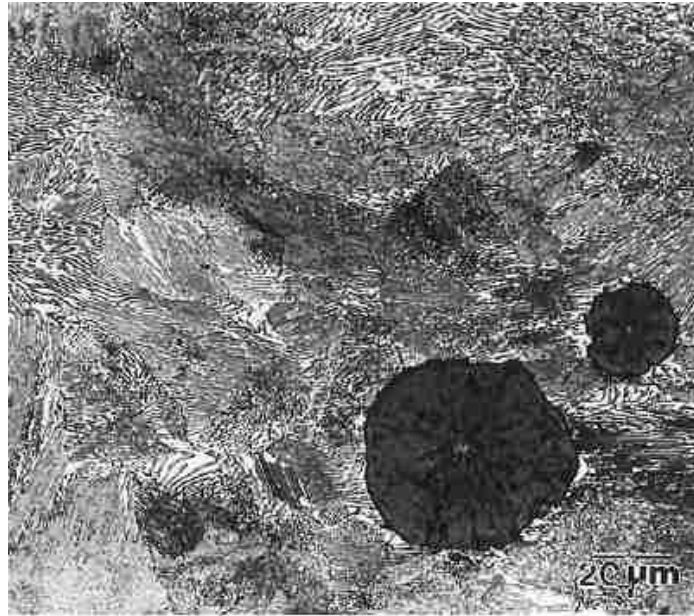


Figure 2.7 Pearlitic ductile (nodular) cast iron. 4% picral. 500X [9].

Microstructural constituents in ductile iron include pearlite, martensite, bainite and ferrite. Ductile iron is used in applications requiring good ductility and toughness. Different heat treatments produce various kinds of ductile iron including ferritic ductile iron, pearlitic ductile iron, ferrite plus pearlite ductile iron, and austenitic plus bainite ductile iron (which is also called ADI) [9, 22].

2.2.6 Austempered Ductile Iron (ADI)

ADI is a grade of iron, in which heat treatment is utilized to produce a metastable face-centered-cubic (FCC) matrix solid solution, austenite, which is stabilized at room temperature because it is saturated with 1.8-2 wt% carbon [23]. ADI's matrix is a mix of acicular (plate-like) ferrite laths and stabilized austenite. The acicular ferrite laths are termed as bainitic ferrite. This mixture of bainitic ferrite in the retained austenite phase is called the ausferrite matrix , Although ADI always contains a certain amount of acicular ferrite, pearlite, and retained austenite, other constituents such as martensite, cementite and other carbides are often present [24]. Figure 2.8 shows a typical ADI microstructure.

It can be seen that the feathery dark bainitic ferrite laths are densely packed in a stable austenite (light color) matrix. In addition, the light coloured and smooth sheaves are martensite.

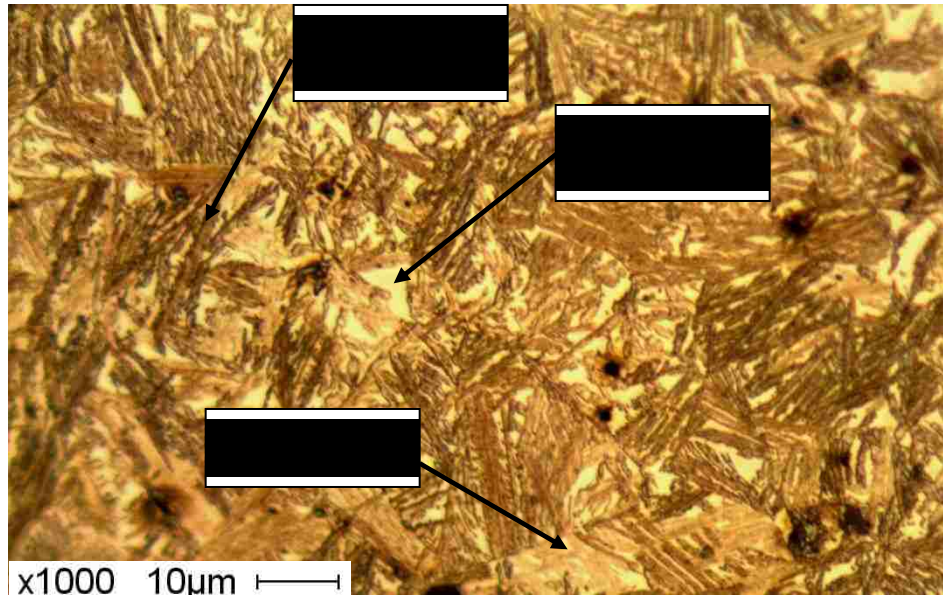


Figure 2.8 ADI ausferrite microstructure [25]

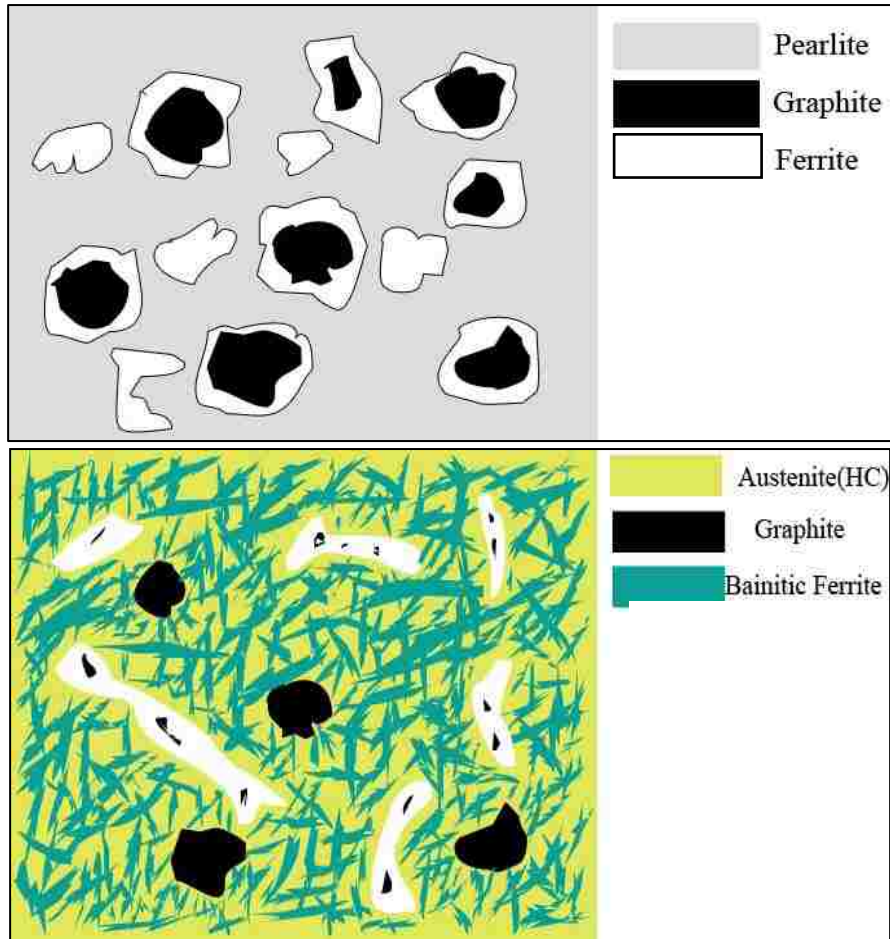


Figure 2.9 Schematic representation of a) ductile cast iron, b) ADI [25]

Figure 2.9 shows schematics of the microstructures of ductile iron (DI) and ADI in Figure 2.9 (a), which is for DI, ferrite and graphite nodules are surrounded by pearlite. The nodular graphite is surrounded by white ferrite; this microstructure is often referred to as a “bull’s eyes”. When we come to ADI (Figure 2.9b), ferrite is in the form of feathery sheaves or laths. They are densely packed inside an austenite matrix. Retained austenite usually accumulates in large areas without graphite nodules, which are usually called "islands" [25].

2.3 Induction Hardened Ductile Iron (IHDI)

For industries such as automotive and aerospace, one of the most versatile material-process combinations is cast ductile iron and induction hardening. A good example is the camshafts used in automotive applications. As it was discussed in the Introduction, cast ductile iron produces a low cost, near net shape component that is suitable for subsequent precision machining and heat treatment. Induction hardening can be economically used to heat the casting and subsequent quenching produces hard, wear resistant martensite. Machining can be performed before, or after, induction hardening [2,26].

2.4 Theoretical Background of Induction Heating

Induction heating is a complex combination of electromagnetics and heat transfer, and metallurgical phenomena. Since magnetic field intensity and temperature have a large influence on the physical properties of heated materials, heat transfer and electromagnetics are very closely interrelated. It is also a nonlinear function of factors including chemical composition, heating intensity, and temperature.

2.4.1 Electromagnetic Phenomena:

An alternating voltage is applied to an induction coil, which leads to an alternating current in the coil circuit. A time variable magnetic field is produced by the alternating coil current; it should be noted that they have the same frequency but an opposite direction. Through the Joule effect (I^2R), these currents produce a large amount of heat [2, 27]. Figure 2.10 shows a conventional induction heating system [27].



Figure 2.10 A conventional induction heating system consists of a cylindrical steel bar surrounded by a multi-turn induction coil [27].

There are several different electromagnetic phenomena taking place during the induction hardening process including the skin effect, the proximity effect and the ring effect[2, 28 ,29]. These effects produce non-uniform characteristic of the current distribution within an inductor and work piece, which, in turn, produces a non-uniform temperature profile in the work piece. These effects are discussed as in sections 2.4.2 to 2.4.4.

2.4.2 Skin Effect:

From the basic electrical theory, it is known that if a direct current (DC) flows through a conductor, the current distribution will be uniform. If an alternating current is imposed through the conductor, there will be a non-uniform current distribution. Research has shown that the current density will decrease from the surface of the conductor towards the center, and the maximum current density is located on the surface [30]. This is called skin effect. Figure 2.11 shows a typical magnetic field intensity distribution [2].

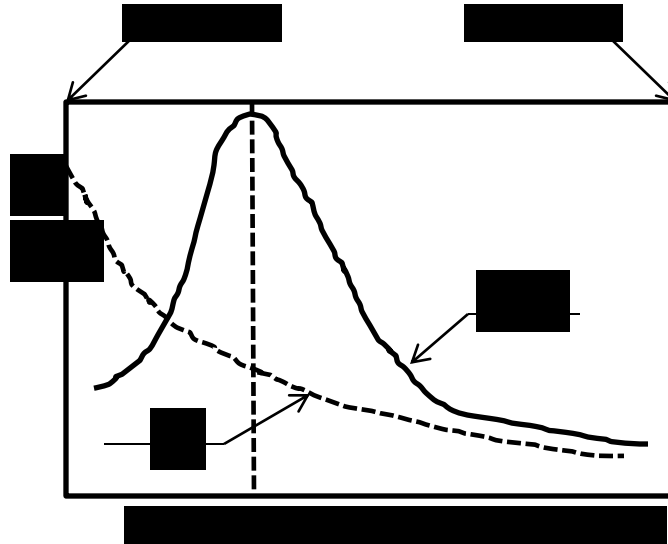


Figure 2.11 Distribution of magnetic field intensity (H) and relative magnetic permeability (μ_r) along the radius of a homogeneous carbon steel cylinder [2].

The skin effect is very important in applications using alternating current, and approximately 86% of the power will be concentrated in the surface layer of the conductor. This layer is called the penetration depth, δ . The distribution of the current density along the work piece radius can be roughly calculated using Equation 2.1 [2,27].

$$I = I_0 e^{-y/\delta} \quad \text{Equation 2.1}$$

where I is current density at distance y from the surface, A/m^2 ; I_0 is current density at the work piece surface, A/m^2 ; y is the distance from the surface toward the core, m ; and δ is penetration depth, m . The penetration depth is given by Equation 2.2 [2].

$$\delta = 503 \sqrt{\frac{\rho}{\mu_r F}} \quad \text{Equation 2.2}$$

Where

ρ = electricity resistivity of the metal,

μ_r = relative magnetic permeability,

F = frequency, HZ (cycle/sec).

From Equation 2.2, it can be seen that penetration depth varies with the square root of electrical resistivity, and inversely with square root of frequency and relative magnetic permeability [2, 31]. Figure 2.12 illustrates the skin effect by showing how the current density changes from surface to the core [2].

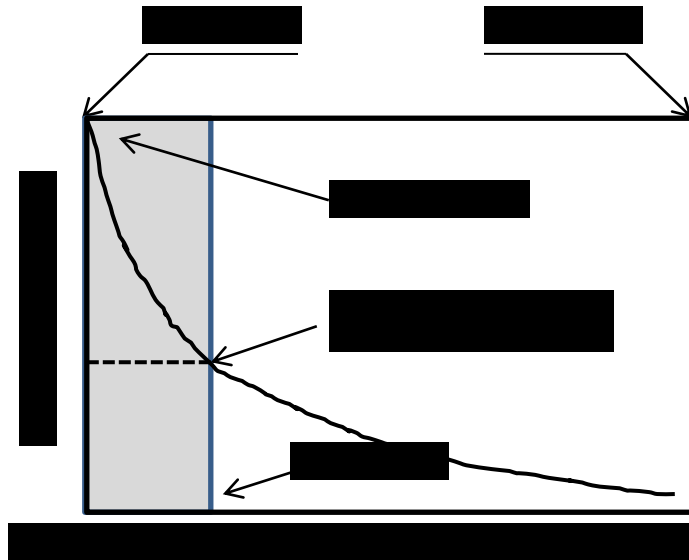


Figure 2.12 Current density distributions because of skin effect [2]

2.4.3 Electromagnetic Proximity Effect:

In practical applications, there may be more than one conductor in close proximity. Each conductor has its own magnetic field, so it brings a distortion of the current and power density distribution because of the interaction of nearby magnetic fields. If the currents flowing in the conductors are in opposite directions, all currents will be concentrated in the area, so that resulting magnetic field will be very strong. The opposite is true if the currents have the same direction. The magnetic field lines will try to eliminate each other, so the magnetic field will be quite weak [32, 33]. Figure 2.13 shows the proximity effect in steel bars [2].

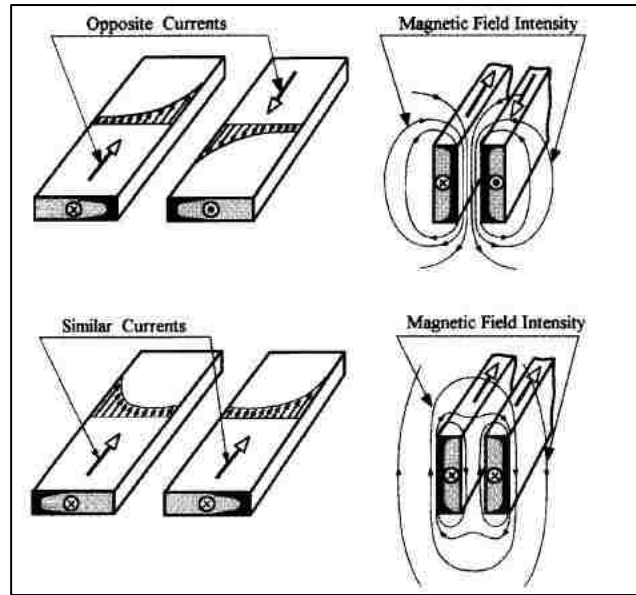


Figure 2.13 Current distribution in bus bars due to proximity effect [2]

2.4.4 Electromagnetic Ring Effect:

All of the conductors we have discussed above are straight conductors. If we bend the conductors into a ring, the current will be distributed differently. Magnetic flux lines will be concentrated inside the ring, and the density of magnetic field will be higher inside the ring. Outside the ring, the magnetic flux lines will be disseminated. As a result, most of the current will flow within the thin inside surface layer of the ring. Figure 2.14 shows this effect in round conductors [2].

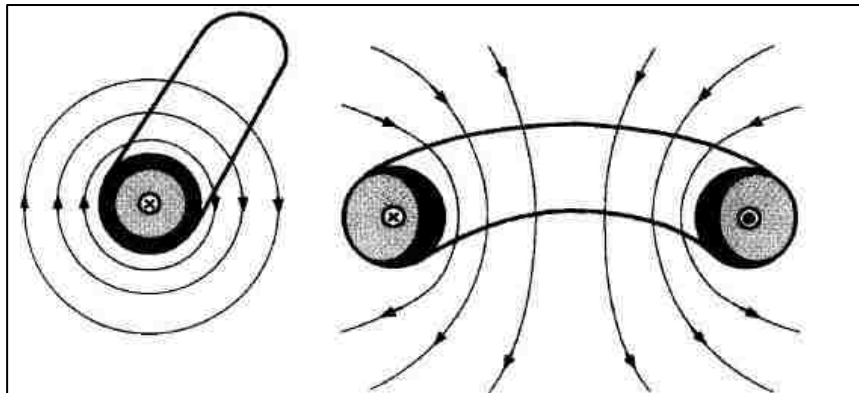


Figure 2.14 Ring effect in round conductors [2]

2.4.5 Thermal Phenomena and Dynamics in Induction Heating

In the induction heating process, all three modes of heat transfer including conduction, convection and radiation take place.

1. Thermal Conduction: Heat is transferred by conduction from the high-temperature regions. Fourier's law describes this phenomenon [2].

$$\overrightarrow{q_{cond}} = -\hat{k} \text{ grad } (T) , \quad \text{Equation 2.3}$$

where $\overrightarrow{q_{cond}}$ is heat flux by conduction, \hat{k} is thermal conductivity, and T is temperature.

2. Thermal Convection: Heat transfer by convection is carried out by fluid, gas or air. Newton's law can well describe this phenomenon, and it states that the heat transfer rate is proportional to the temperature difference between workpiece and ambient area [2]:

$$\overrightarrow{q_{conv}} = \alpha (T_s - T_a) \vec{h} , \quad \text{Equation 2.4}$$

where $\overrightarrow{q_{conv}}$ is heat flux density by convection, α is the convection surface heat transfer coefficient, T_s and T_a stands for surface temperature and ambient temperature, respectively.

3. Thermal Radiation: Here the heat is transferred from hot work piece into surrounding areas including a nonmaterial region (vacuum). It could be introduced as a phenomenon of electromagnetic energy by Stefan-Boltzmann law of thermal radiation.

When it comes to the dynamics of induction heating, it should be noted that there is no simple model. However, there are several influencing factors including electromagnetic and thermal properties of work piece, power supply features and control mode. Generally, there are three main stages involved with the induction heating dynamics when considering a carbon steel cylinder:

Stage 1: The entire work piece is magnetic. The magnetic permeability is quite large when the current penetration depth is very small, so the skin effect is pronounced, while the heat loss is relatively low. Then due to the skin effect, there is a rapid increase in temperature at the surface with no change at the core. During this stage, the electrical efficiency increases, then reaches its maximum, and shortly after it decreases.

Stage 2: When the temperature passes the Curie point, the electrical resistivity of the work piece increases to approximately two to three times its initial value. A decrease of magnetic permeability and increase of electricity resistivity cause a six- to tenfold increase in the surface and inner layers of the work piece. Thus the surface becomes nonmagnetic with magnetic internal layers.

Stage 3: The thickness of the surface layer with nonmagnetic properties exceeds the penetration depth in hot steel and the dual-properties phenomenon becomes less pronounced and will finally disappear. The power density will then have its classical exponential distribution [34].

2.4.6 Quenching after Induction Hardening

Immediately after the induction heating process, the workpieces are cooled by surrounding or immersing them in a quenchant. The aim of quenching is to control the cooling rate to obtain the desired hardness and microstructures [27]. There are many factors influencing hardness and hardenability, such as the microstructure when austenitized and the cooling rate of the etchant. Proper selection of quenchant and a full understanding of the quenching principles are required.

There are three stages in the quenching process including the vapor blanket stage, the boiling stage, and the convection stage. These three stages are discussed as follows:

- **The vapor blanket stage** occurs when induction heating samples are quenched from the austenitizing temperature. Since the heat from the workpiece surface could easily vaporize the quenchant, a thin vapor pocket is formed on the surface of the workpiece. Then, due to the poor conductivity of vapor pocket, radiation and conduction through vapor blanket becomes the main method of heat transfer. Not all quenchants produce a vapor pocket, e.g. oil.
- **The boiling stage** occurs after the first stage. When the vapor pocket collapses. There is no barrier between the quenchant and workpiece surface for direct contact. This leads to nucleation of boiling.
- **The convection stage** is the last stage of quenching. The continuous cooling of the workpiece reduces the surface temperature below the boiling temperature of the quenchant. Convection of heat between the workpiece surface and the quenchant becomes the main method of heat transfer. This stage has the lowest cooling rate.

Because of the different cooling characteristics, various kinds of quenchants are used.

Figure 2.15 compares the cooling curves of these quenchants [27]:

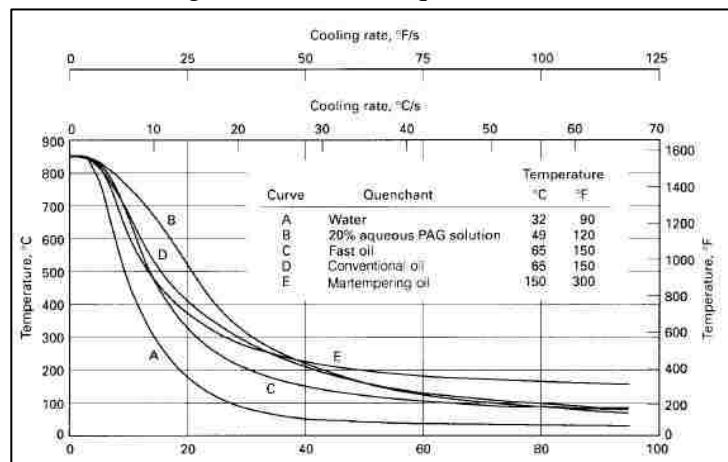


Figure 2.15 Effect of selected quenchants on the cooling curves of a 25.4 mm diam steel bar. All quenching flowing at 0.5 m/s [27]

2.5 Applications of Induction Heat Treatment

Since its introduction in the 1930s, induction heat treatment has been widely used in a large variety of commercial industrial products [27,35,36]. Initially, it was only used in the hardening of round steels parts such as shafts. Soon after that, other products with complex shapes were hardened by the newly developed induction heating process. Nowadays, it has been used for heat treating large case depths and entire cross sections. Table 2.1 lists some common industrial parts produced by induction heat treatment.

Table 2.1 Typical induction hardened parts and applications [27]

Typical parts	Transportation field	Camshafts, crankshafts, transmission shafts, splined shafts, gears
	Machine-tool field	Lathe beds, machine beds,
	Metalworking and hand-tool fields	Rolling-mill pliers, hammers, diagonal pliers
Applications	Oil-country tubular products, structural members, spring steel, Chain links	

With respect to camshafts, other methods have been used for hardening the surface, e.g., Furnace hardening, flame hardening, and liquid nitriding. With the broad use of induction hardening, it was found to have many advantages, including the following ones:

- Induction hardening focuses on the areas that need to be hardened, thus leaving a soft core for easy machining.
- It leads to the minimization of scaling in steels. Because it is a relatively rapid heating process, heavy scaling is easily avoided.

- From a mechanical property perspective, induction hardened workpieces can have higher strength, torsional and bending fatigue resistance than products produced by other techniques.
- Because the induction heating systems can be designed to be computer automated, manufacturing cells and automatic tempering operations can be performed in order to obtain parts with specific properties.

Figure 2.16 shows the various commercial applications of induction hardened ductile iron products [37,38, 39, 40]:



Figure 2.16 Various commercial applications of induction hardening ductile iron a) gears b) sprockets c) engine blocks d) camshafts

2.6 Fast cooling of Austenite:

As mentioned in section 2.1 for the iron-carbon diagram, during the induction heating process, the work piece is heated up to austenite region, then rapidly cooled (quenched). Workpieces need to be cooled to give the preferred martensitic microstructure. If the cooling is not sufficiently fast, the final microstructures may have pearlite or bainite in the martensite. Different cooling rates and their related effects on the transformation of austenite and formation of the various transformation products will be discussed in this section [2,27,41, 42].

2.6.1 Time-Temperature-Transformation (TTT) Diagram

The Time-Temperature-Transformation (TTT) diagram is also called the Isothermal Transformation (IT) diagram. It is useful in selecting through-hardening practices for ductile iron. Figure 2.17 shows a typical TTT diagram for a low-silicon ductile iron [42]. It can be seen that the time-temperature cooling relationship required to produce a specific microstructure is defined by the cooling path. The position of the transformation zone is defined by start and finish curves. A TTT diagram also determines the rate and extent of cooling required to avoid certain transformations and promote others. According to the research, alloying elements can have a huge influence on the TTT diagram. For instance, increasing the molybdenum content will shift the transformation zones to the right, allowing complete transformation to martensite at a lower cooling rate [22].

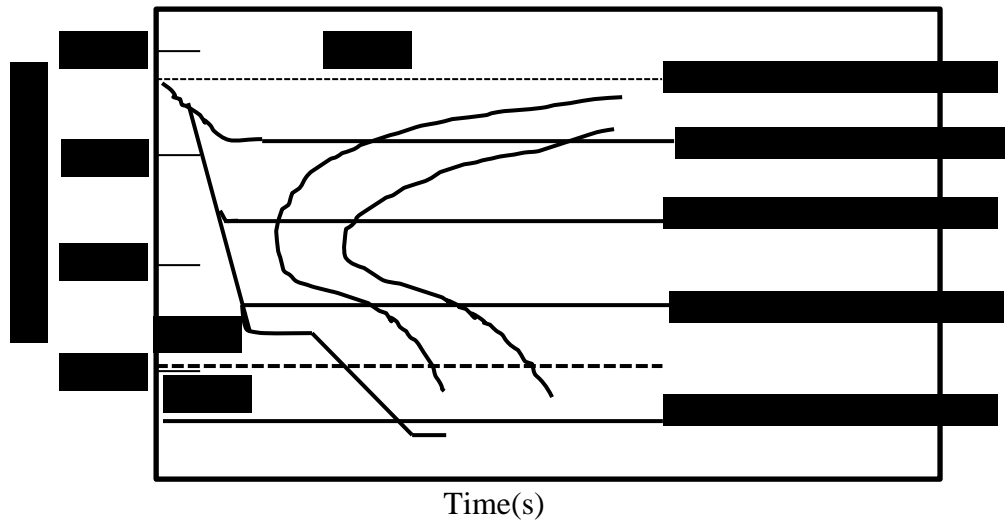


Figure 2.17 Typical TTT curve for low-silicon ductile iron [42]

2.6.2 Continuous Cooling Transformation (CCT) Diagram

Microstructures that have been produced by cooling and holding under equilibrium conditions are shown on IT diagrams. Different ductile irons have different IT diagrams. These diagrams typically have C-shape to the curve, with time for transformation decreasing below the A_1 temperature, and then increasing again below the nose of the C curve. In the induction hardening process, the cooling rate should be fast enough for ductile iron to miss the knee of this C-curve [15, 25].

CCT diagrams show the microstructures produced by different rates of cooling. They offer help in selecting quenchants with fast enough quenching speeds to produce the cooling rates needed to form martensitic microstructures. Figure 2.18 shows a typical continuous cooling transformation diagram for a low-alloyed ductile iron [43].

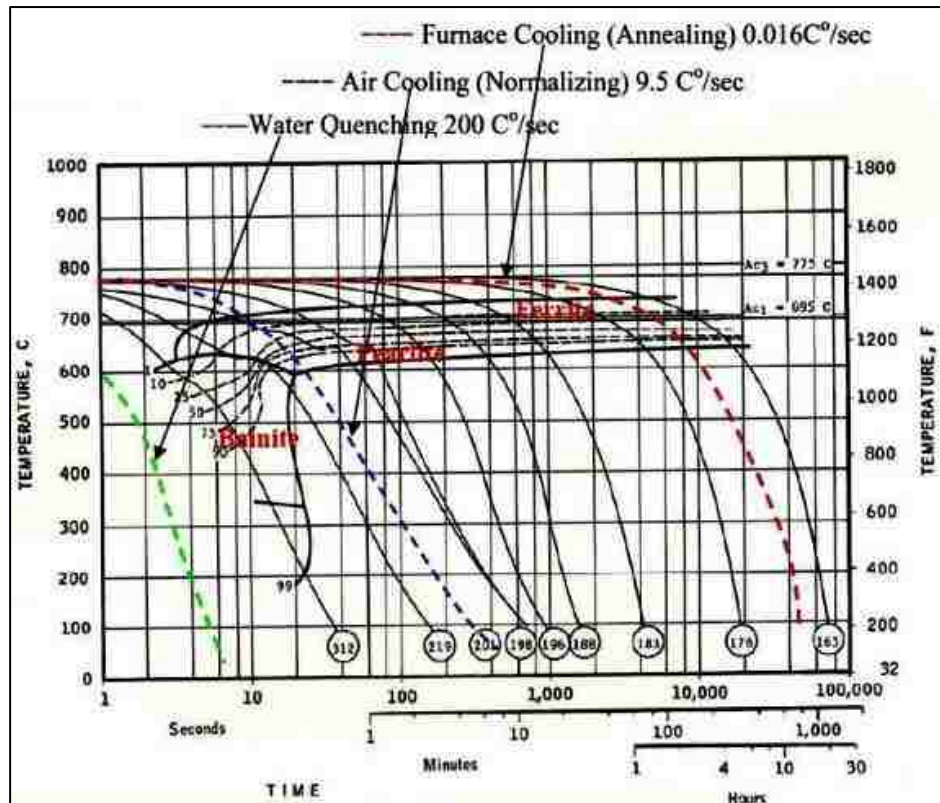


Figure 2.18 Continuous Cooling Transformation (CCT) diagram of a low-alloyed ductile iron [43].

Figure 2.18 describes what happens during the continuous cooling of the iron through the eutectoid region. The eutectoid region is the temperature range where austenite which is formed during heat treatment transforms to ferrite and pearlite. Ferrite begins to form when the iron temperature falls below the upper critical temperature and if the iron temperature stays above the lower critical temperature long enough for the transformation to take place, a ferritic microstructure would occur. If the austenite is not completely transformed by the time the temperature drops below the lower critical temperature, the austenite will transform to pearlite.

2.6.3 Microstructures Produced During Cooling:

During the cooling from austenite, there are many transformation products formed. This microstructural consistent always depends on the specific alloy and the cooling rate.

A martensitic microstructure is usually most desirable because it has the optimum mechanical properties [27,44,45]. These transformation products are usually those as detailed as follows:

Pearlite is usually produced because of the slow cooling rate. It is actually a mixture of two different phases: ferrite and cementite. Cementite is formed as lamellar plates in the ferrite matrix. Pearlite can be found in the microstructure of a quenched part when the austenization process was not complete. Actually, in induction hardened ductile iron, pearlite is not normally found unless there is interrupted or slack quenching so that the dissolution of pearlite was not completed during austenitization [27].

Martensite is a transformation product formed by fast cooling of a steel alloy below the M_s temperature, which varies greatly with composition. This phase is actually a supersaturated solution of carbon in ferrite. The martensite formation mechanism is one in which a shear stress moves iron atoms co-operatively and almost simultaneously from their original sites in the austenite structure to the nearest available site in the final structure. It is always needle-like. On the IT and CCT diagrams, there is a martensite start temperature and a martensite finish temperature, M_s and M_f . It should be noted that there is a volume increase when transforming austenite to martensite. It is very difficult to determine the M_f temperature, and the end of transformation is often defined by either 90% or 95% transformation, which is usually the case for eutectoid steels close to room temperature. Figure 2.19 (a) shows a typical martensitic microstructure in induction hardened ductile iron. The martensite is needle-like and has a gray or dark color [46, 47,48].

Retained Austenite. As indicated by the IT and CCT diagrams of ductile iron, the M_f temperature is always below room temperature. There is always a certain amount of

residual or retained austenite found at room temperature after quenching. According to Chrysler Specification (PS-5) for induction hardened ductile iron camshafts, a level of 8% retained austenite is acceptable. However, in practical manufacturing processes, there may be an excessive amount of retained austenite, which may result in premature wear or spalling of the surface of the camshaft lobes [2,15, 49, 50,51]. Figure 2.19 (b) shows a typical ductile iron sample containing retained austenite islands lying in the martensite matrix.

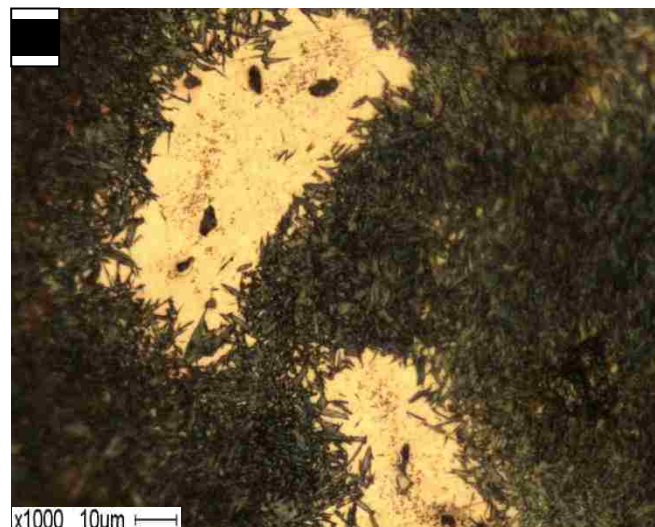
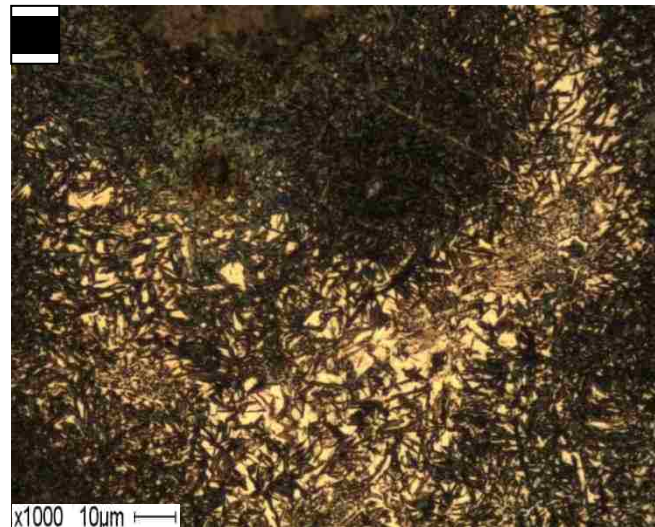


Figure 2.19 Microstructure of induction hardening ductile iron camshaft showing (a) needle-like martensite (b) white retained austenite islands in martensite matrix.

2.7 Residual Stress and Induction Hardening

In the induction hardening process, the workpiece usually has a distribution of residual stresses. Usually, there are three kinds of stresses specific to induction heating: initial, transitional and residual stresses. Initial stresses depend on operations that have taken place prior to heat treatment. Transitional stresses occur because of the heating and cooling, and they will partially or totally disappear when induction heating is finished. Residual stresses are a product of these two stresses.

Additionally, there are two kinds of stresses associated with heat treated parts: thermal stresses and stresses brought about by phase transformations [2, 27].

Thermal Stresses, they are produced first during the heating and then through the cooling of the work piece. Figure 2.20 shows the stresses at the surface of a carbon steel cylinder in the induction hardening process [27].

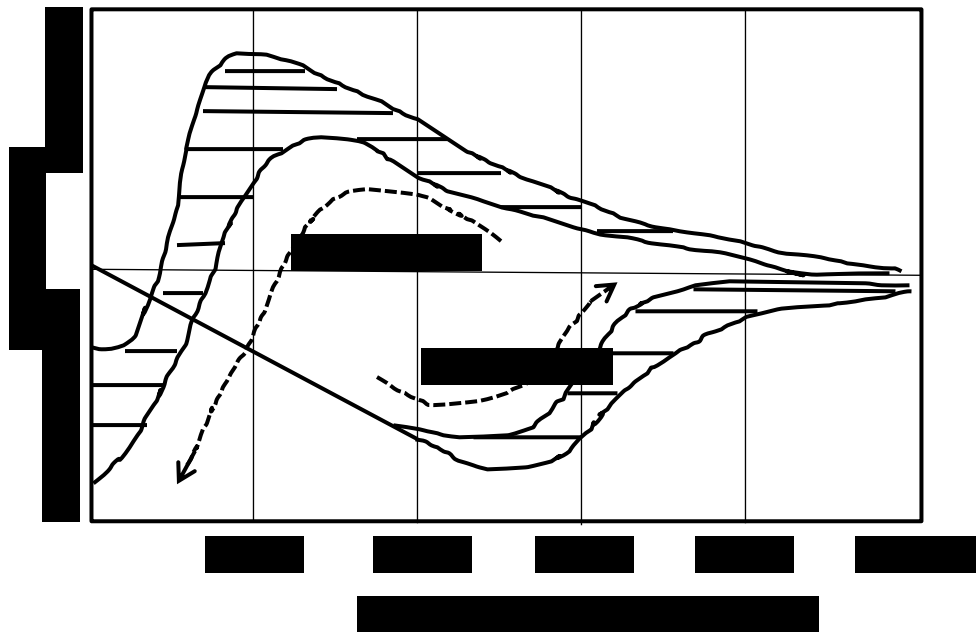


Figure 2.20 Stresses at the surface of a carbon steel cylinder during heating and quenching. Martensite formation results in a final compressive residual stress state [27].

It can be seen from Figure 2.18 that during the heating process, the surface is kept in compression until it reaches 1000 °C. At this temperature, the surface becomes plastic. During the cooling process, the work piece has tensile stress until the surface comes to the martensite formation stage. The level of stresses depends on the thermal coefficient of expansion and elastic modulus of the material. Thus, the amount of heat transfer and rate of heating determines the thermal stresses. Residual stresses on heating will have very little effect except when tensile stresses are high on the inside and the outside compressive stresses are relaxed through subsequent plastic deformation. In this case, the inside remaining tensile stress are large enough to cause the part to crack. This means that induction heating could cause cracks when heating cold-drawn bar stock, when the bar is not stress relieved uniformly, and there are still large tensile stresses inside the core.

When it comes to the cooling process, there are several different kinds of stress conditions. First of all, because of the thermal contraction, there is an increase in tensile strength for outside surface, and the volume is also decreasing at the same time. The net residual stresses in the part after cooling depend on the contraction of the core and its effect on contraction of the surface.

Stresses from Phase Transformations. These stresses occur due to microstructural changes taking place as a result of the formation of austenite, bainite or martensite. The most important change is actually the change of austenite into martensite because it will bring an approximately 4 % increase in volume [15, 52, 53] . The area that is martensitic tries to increase in size, producing a compressive stress as the core cools. If there is very little temperature variation between the surface and the center of work piece, the surfaces can quench in tension. Figure 2.21 shows a typical hardness and residual stress profile in induction-hardened steel [27].

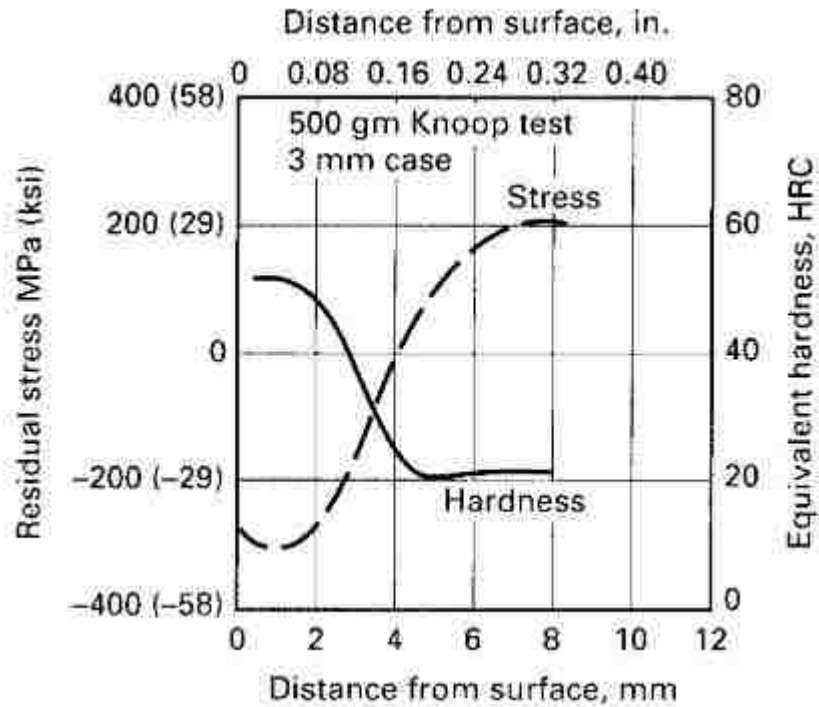


Figure 2.21 Typical hardness and residual stress profile in induction-hardened 1045 steel [27].

The residual stresses brought about by thermal phenomena and transformation volume changes are complex. The thermal stress is independent of the stress brought about by phase transformation. During the quenching process, hard martensite forms at the surface of work pieces, associated with thermal volume contraction and phase-volume expansion. However, the remainder of workpiece under the surface is still hot and ductile austenite. Later when the remaining austenite transforms into martensite, the volumetric expansion is restricted by the hard surface layer. This restriction causes the central portion to be under compression and outer surface under tension. During the final cooling of the interior core, surface contraction is hindered by the hardened surface layers. This restraint produces a compressive stress at the outer surface and a tensile stress in the inner layers.

After quenching the induction hardened work piece, a compressive stress will develop at the surface when austenite transforms into martensite. The compressive stress development depends on the nature of the hardened case and stresses developed during quenching. The magnitude of the compressive stress could increase the yield strength and improve fatigue life. However, it should be noted that there is a sharp transition to a tensile state in the transition zone between the case and unhardened core material. An increase in hardenability could change the depth at which transition from a compressive to a tensile stress occurs. In practical applications, industry usually uses an initial heat to increase the core temperature followed by increase in the rate of heating: this process not only optimizes and produces the maximum compressive stress at the surface, but can also minimize the tensile stress under the surface.

Generally speaking, the area just beneath the hardened case is a zone of potential danger, because maximum tensile residual stress is located there. For this reason, most subsurface cracks initiate there. The overall residual stress condition in the as-quenched part promotes brittleness that reduces the part reliability. Sometimes these induction hardened workpieces need to be tempered, a process where the tensile stresses are relieved and beneficial surface compressive stresses are retained.

2.8 Retained Austenite and Residual Stress Measurement

There are various methods for measuring retained austenite (RA) and residual stress (RS), including x-ray diffraction (XRD). A brief review of RA and RS measurements is given separately in this section.

Residual Stress. There are many methods for measuring residual stress including hole drilling, acoustic wave propagation, Barkhausen “noise” in magnetic materials, x-ray

diffraction (XRD), and neutron diffraction [55]. The principle for XRD residual stress measurement is that residual stress causes the interplanar spacing of the material to change [54, 55, 56] . Residual stress is evaluated from strain values using Young's modulus, Poisson's ratio, consideration of the elastic anisotropy of the material [15]. X-ray calculation of residual stress involves several steps: First, the samples are irradiated with x-rays, and the angle of maximum diffracted intensity is measured. Compressive stresses decrease the interatomic plane spacing (d-spacing). It is used as a strain gage which can give the value of strain [15, 27, 57]:

$$\varepsilon = \frac{d-d_0}{d_0} = -\cot \theta \Delta\theta \quad \text{Equation 2.5}$$

where ε is the strain, d is the stressed plane spacing, and d_0 is the unstressed plane spacing. θ is the Bragg scattering angle.

In the current research, the $\sin^2\psi$ method is used because of its accuracy. For this method, a number of d-spacings are measured, and stresses are calculated from an equation derived from Hooke's law: Equation 2.6 [58, 59]

$$\varepsilon_{\phi\psi} = \frac{1}{2}S_2(\sigma_\phi - \sigma_{33})\sin^2\psi + \frac{1}{2}S_2\sigma_{33} - S_1(\sigma_{11} + \sigma_{22} + \sigma_{33}) + \frac{1}{2}S_2\tau_\phi \sin 2\psi \quad \text{Equation 2.6}$$

where $\frac{1}{2}S_2$ and S_1 are the x-ray compliance constants of the material, variations of σ_{ij} are the stress-tensor components, σ_ϕ is the stress in the direction of the measurements, τ_ϕ is the shear stress in the direction of the measurements, ψ is the angle subtended by the bisector of the incident and diffracted beam with the specimen normal, and $\varepsilon_{\phi\psi}$ is the strain for a given ψ tilt. The definition of the axis and direction of residual stress measurement is shown schematically in Figure 2.22[58]:

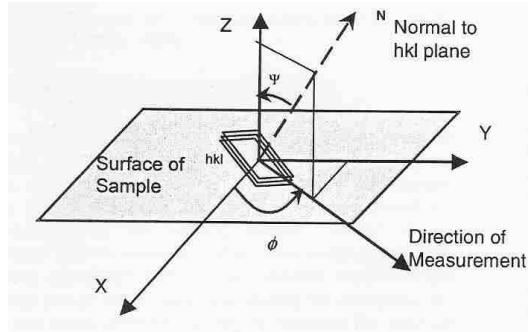


Figure 2.22 Definition of the axis and the direction of residual stress measurement [58]

Retained Austenite. There are also many ways of measuring RA including optical metallography (OM), dilatometry, the saturation magnetization intensity method, and the x-ray diffraction (XRD) method. Here the XRD and OM methods are discussed in detail:

According to ASTM Standard E975 [60], XRD can be used to measure retained austenite contents greater than 1 % by volume with excellent precision. The principle is to compare the integrated intensities of selected (hkl) plane reflections of the martensite and austenite phases. The assumption is that the integrated intensity of a phase is proportional to its volume fraction. Equation 2.7 shows the calculation of volume fraction of retained austenite by XRD [61]:

$$V_A = \frac{I_A^{hkl} / R_A^{hkl}}{I_A^{hkl} / R_A^{hkl} + I_M^{hkl} / R_M^{hkl} + I_C / R_C} \quad \text{Equation 2.7}$$

where I^{hkl} is the integrated intensity per unit length of the diffraction line (hkl) for a given phase, R^{hkl} is the theoretical relative intensity factor for a specific (hkl) line for a given phase, and I_C/R_C is the corrected intensity ratio for a carbide or graphite line.

Although there are many advantages to the XRD method because of its accuracy and the ability to measure very low austenite contents, there are also some disadvantages including high-cost and the specific requirements for sample preparation. The

metallographic method has become very popular since it has no requirements on exterior specimen geometry, and it has the potential for determining the entire austenite gradient with a single specimen preparation.

Retained austenite in induction hardening components has relatively low hardness, which has a significant influence on the residual stress, and has the potential for strain induced transformation. It can have a very strong influence on mechanical properties. There has been an interest in the measurement of retained austenite by XRD and OM methods. According to literature, for high carbon materials having a lenticular martensite matrix, agreement between X-ray and metallographic measurements has been demonstrated with austenite volume fraction as low as 3 percent.

2.9 Previous Studies:

Many researchers have tried to find a correlation between retained austenite contents measured by XRD and OM for carburized steel samples. Averbach [62] had pointed out that it had a good agreement between XRD and OM even at values as low as 3 percent of retained austenite. He argued that the necessary condition for metallographic measurement of retained austenite was that the samples should be prepared in such a way that both the operator and computer software could distinguish the austenite from other microconstituents that are present.

In addition, as noted by Klosterman [63], the most important aspect of using OM to determine RA contents is an easy distinction among the three principal microconstituents, austenite, martensite, and the surface martensite. Surface martensite forms on the specimen surface from retained austenite during specimen preparation and generally cannot be avoided, even by electropolishing techniques.

Another aspect in optical metallography is that proper etchant is needed to fully reveal the real microstructures of induction hardened samples. A large number of etchants have been tried; the requirements for an etchant are ease of use, reproducibility of results, and good delineation of microconstituents. According to previous studies [12] and our current experiments, it is found that 2 percent nital + zephiran chloride might be the most suitable etchant for most steels and alloys. Table 2.2 gives the various etchant used in previous studies [12] by researchers:

Table 2.2 Etchants used in Previous Studies [12]

No.	Name	Composition	Procedure
1	Modified picral	5 ml HCL+1g picric acid+ 100ml ethanol	Immersion
2	Picral-Nital	4 g picric acid + 1 ml HNO ₃ + 100 ml ethanol	Immersion
3	2 pct nital	2 ml HNO ₃ + 100 ml ethanol	Immersion
4	2 pct nital + zephiran chloride	2 ml HNO ₃ + 100 ml ethanol + 1 drop zephiran chloride	Immersion
5	–	CuSO ₄ solution, followed by Na ₂ S solution	Swab
6	–	50 ml saturated sodium thiosulfate solution + 1 g calcium metabisulfite followed by 30 ml 5 pct NaOH + 10 ml 3 pct H ₂ O ₂	Swab

Eldis [12] compared X-ray diffraction and quantitative metallography for carburized EX 24, EX 32 and SAE 4820 samples. After proper polishing and etching, a Quatnimet image analyzing computer was employed to determine the RA content. The computer was set to detect microconstituents whiter than a certain threshold level. In his judgement, all of the observable austenite and surface martensite was detected as a single

microconstituent. Figure 2.23 shows optical micrograph and electron micrograph done of carburized X-ray specimen of EX32, 0.100 mm case depth [12]:

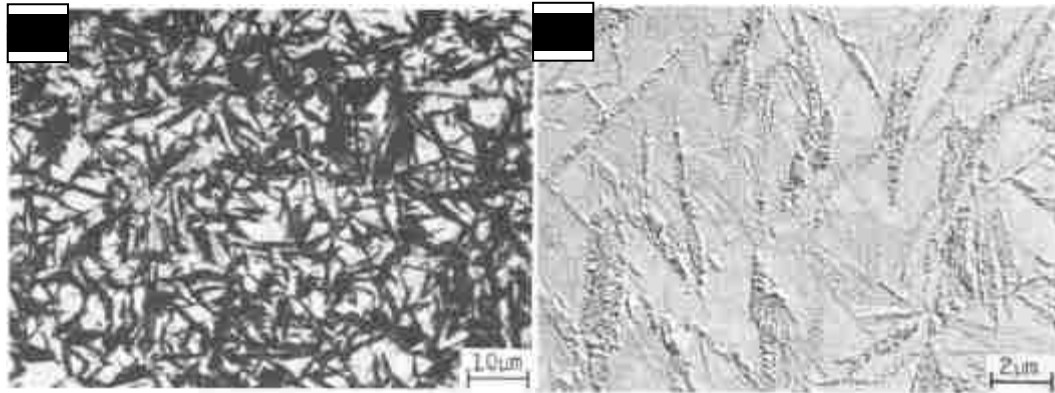


Figure 2.22 Carburized X-ray specimen of EX 32, 0.100 mm case depth, 2 pct nital +zelpheiran chloride (a) optical micrograph (b) electron micrograph. Surface martensite is the light-etching lenticular microconstituent in (a) and the untempered, carbon-free lenticular microconstituent in (b) [12].

After obtaining the retained austenite content from both methods, a correlation could be made, Figure 2.24 shows the individual austenite measurements, plotted as XRD vs metallographic results. It can be seen that the dashed line has a slope of one and represents the locus of data points if the results of the two experiment techniques were in perfect agreement. The solid line is the least-squares line through all the data. Linear regression was tried for the data of each steel individually, but there was no statistically significant difference among the slopes and intercepts. So after mathematical simulation, the data shown in Figure 2.24 could be fitted Equation 2.8 [12]:

$$\text{Pct}\gamma_{\text{Met}} = 1.12 * \text{Pct}\gamma_{\text{X-ray}} - 2.85 \quad \text{Equation 2.8}$$

where γ signifies austenite and the subscripts refer to the metallographic and X-ray techniques, respectively. This equation shows that a general trend in low austenite contents metallography reveals less austenite than X-ray diffraction, while at high austenite contents metallography detects more austenite than X-ray diffraction.

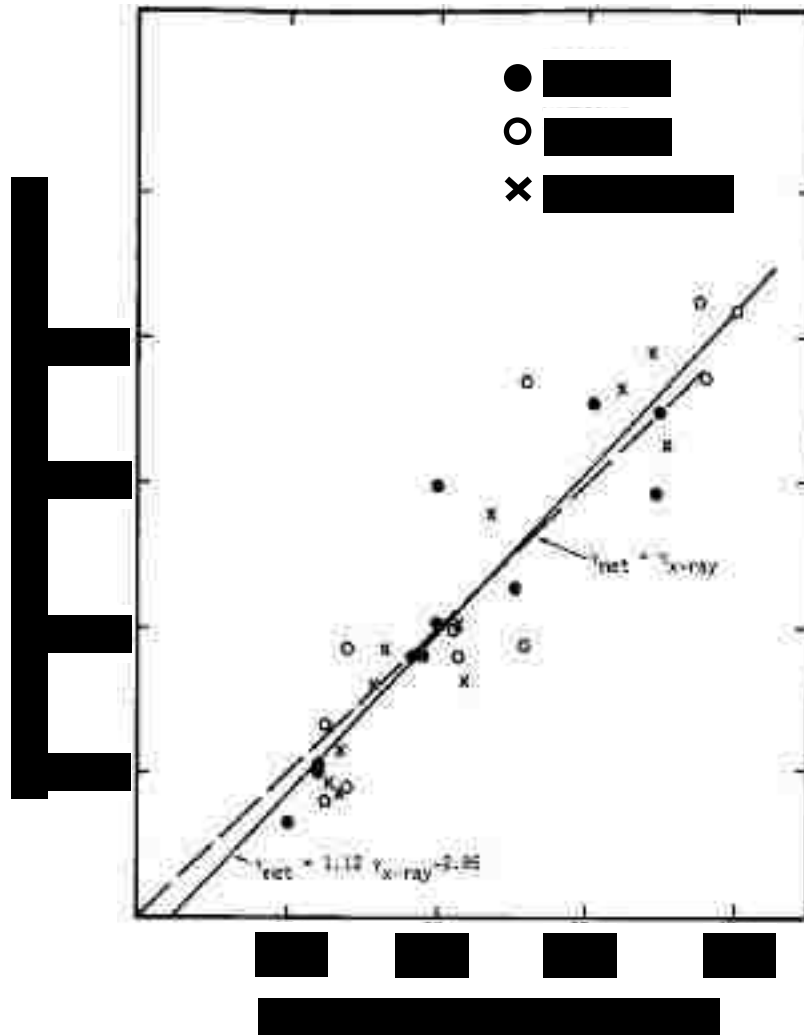


Figure 2.23 Measurement of retained austenite, metallography vs X-ray [12].

Since retained austenite has a large influence on the residual stress level, a correlation of residual stress and retained austenite content has been done by Kirk [64] which is shown in Figure 2.25.

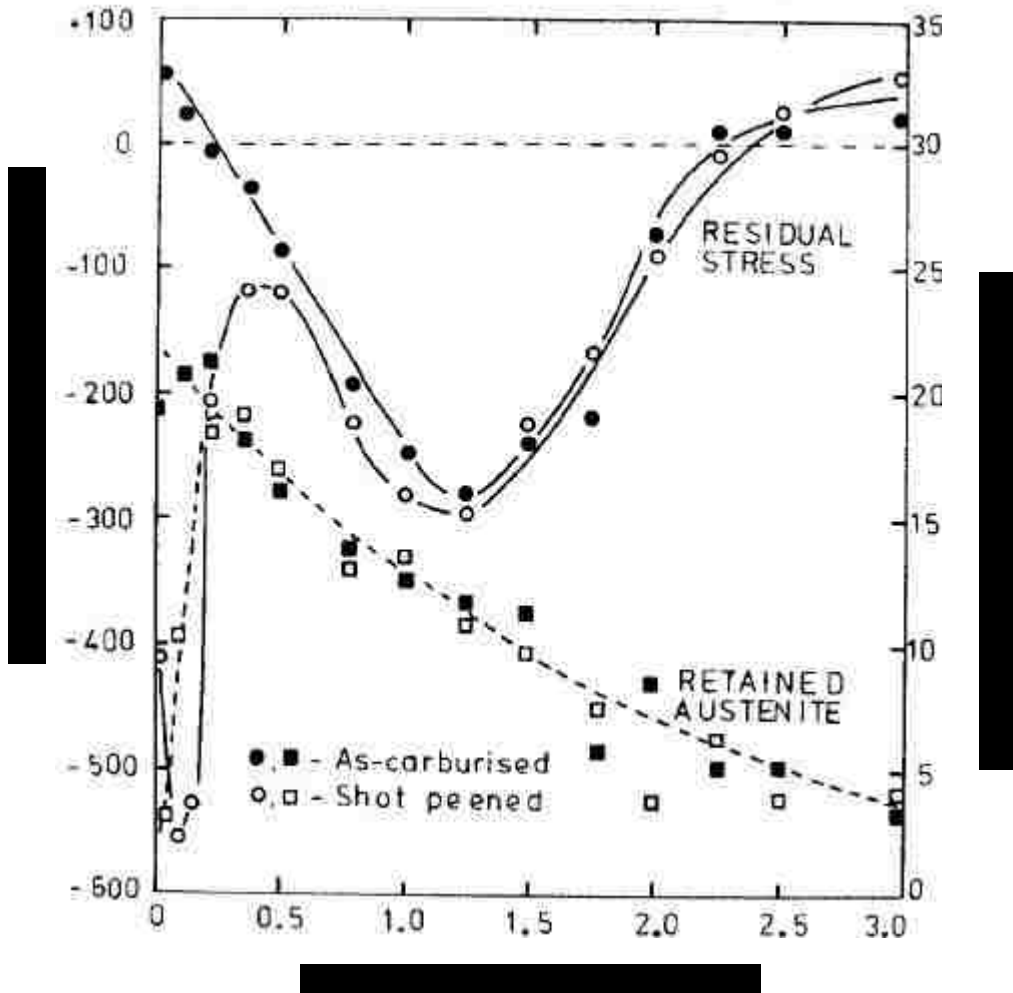


Figure 2.24 Residual stress and retained austenite distributions in as-carburized and shot peened carburized steel [64]

Although Eldis [12] obtained results for EX 24, EX 32 and SAE 4820 steels, the measurement of RA in ductile iron is less well researched. The reasons stem not only from the complex microstructures existing in ductile irons (martensite, retained austenite, pearlite, nodular graphite, bainite, and sometimes ferrite), but also from some possible manufacturing defects which might influence the XRD measurement of retained austenite content. For instance, in the case of the austempered ductile iron (ADI) discussed in section 2.2.6, yellow colored bainitic ferrite (also called ausferrite) and martensite blocks

the retained austenite islands. It causes difficulty in determining the real volume fraction of the retained austenite content in ADI.

CHAPTER III

EXPERIMENTAL DETAILS

The microstructural kinetics and properties of induction hardened ductile iron were evaluated in a series of samples. Metallographic analysis and X-ray diffraction analysis were performed on the samples, which were induction hardened for different times.

3.1 Overview of the Experimental Procedures and Measurements:

The experimental procedures can be divided into 5 main areas, namely:

1. Heat treatment design
2. Sample production
3. Sample Characterization : X-ray diffraction (XRD)
 - a. Retained Austenite (RA)
 - b. Residual Stress (RS)
4. Microstructural analysis: Retained Austenite
 - a. Optical metallography
 - b. Image analysis
5. Mechanical property analysis
 - a. Hardness testing

Two independent certified laboratories, identified as Laboratories A and B, performed XRD measurement of the RA & RS on all samples to determine any possible variation between testing facilities.

3.2 Material and Casting:

The ductile iron sample was provided by Chrysler LLC Technology Center (CTC). Its composition was determined by using optical emission spectroscopy and is given in Table 3.1.

Table 3.1 Chemical composition (Wt. %) of induction hardened ductile iron

Element	Wt.%
Carbon (C)	3.63
Manganese (Mn)	0.81
Phosphorus (P)	0.010
Sulfur (S)	0.004
Silicon (Si)	2.14
Chromium (Cr)	0.04
Nickel (Ni)	0.03
Molybdenum (Mo)	0.02
Copper (Cu)	0.93
Aluminum (Al)	0.010
Vanadium (V)	0.004
Columbium (Cb)	0.006
Titanium (Ti)	0.006
Cobalt (Co)	0.004
Tin (Sn)	0.066
Boron (B)	0.0012
Magnesium (Mg)	0.053
Tungsten (W)	0.007

The significant alloying elements, apart from C, are Si (2.14%), Mn (0.81%) and Cu (0.93%). According to Tisza [65], cast irons contain two kinds of alloying elements: graphitizing and whitening elements. Graphitizing elements promote graphite formation while whitening elements stabilize cementite and carbides. Figure 3.1 illustrates the effects of different elements on the microstructure of cast iron.

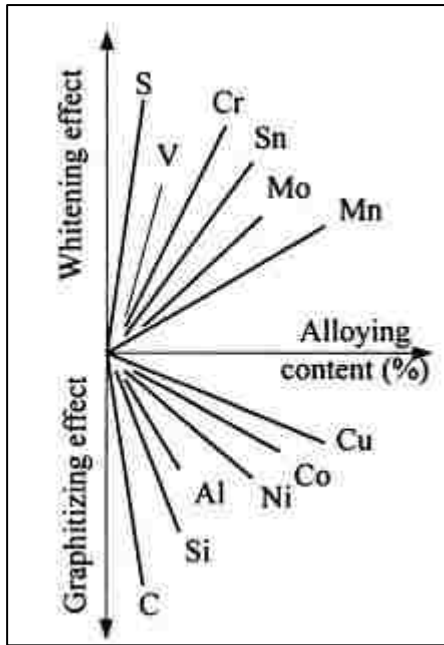


Figure 3.1 Effect of alloying elements on the microstructure of cast iron [65]

A carbon equivalent (CE %) can be calculated from the chemical composition using Equation 3.1 for ductile iron [27] :

$$CE = \%C + 0.3(\%Si) + 0.33(\%P) - 0.027(\%Mn) + 0.4(\%S) \quad \text{Equation 3.1}$$

The CE value for our ductile iron melt is 4.255%, which indicate that the camshaft should be eutectic after casting.

3.2.1 Casting Details:

A general procedure [68] for the casting of ductile iron includes the following steps.

- The raw materials include selected steel scrap, special grades of pig iron, foundry ductile iron scrap, magnesium and cerium.

- The raw materials are melted in a coreless induction furnace at a temperature of 2600 °F (1426 °C).
- Highly basic materials including sodium carbonate, calcium carbide or quicklime are added to the molten iron in a suitable vessel and then the bath is agitated to kill the sulfur in the iron.
- Cerium, in amounts from 0.5 to 1.5% in the iron-silicon-magnesium alloys (5 to 10% magnesium) is added to the melt.
- A silicon addition is added to the melt to promote the formation of well-shaped nodules.

3.2.2 Microstructure of as-cast material:

Before the induction-hardening process, optical microscopy of the as-cast ductile iron was conducted. As shown in Figure 3.2, it reveals a predominantly pearlitic or lamellar structure with dark nodular graphite and light ferrite encircling the nodular graphite.

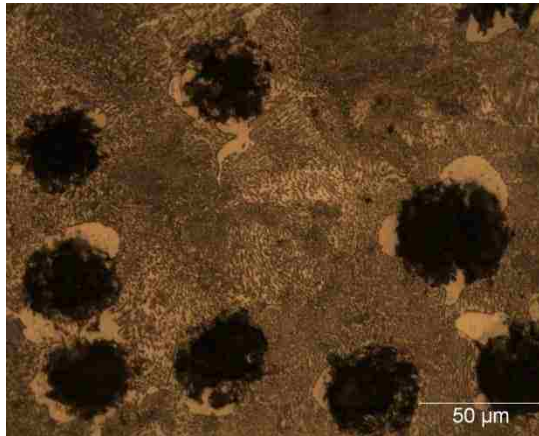


Figure 3.2 Microstructure of as-cast ductile iron sample.

3.3 Induction Hardening:

Induction hardening of the camshafts was performed at a parameter of 75 KV and 25 KHz frequency for times from 1.4 to 1.8 seconds. These process parameters were

chosen based on prior industrial experience of process windows that produce the desired surface hardened characteristics. The camshafts were quenched and the quenchant is a mix of 60% polymer and H₂O (65-110 °F). Figure 3.3 shows the experimental set-up for the induction hardening

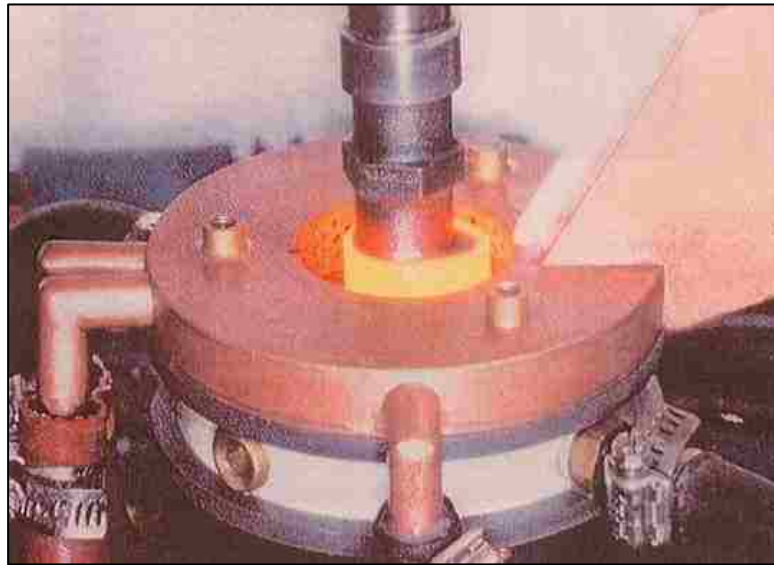


Figure 3.3 Induction hardening of ductile iron camshaft

3.4 Sample Preparation:

A photograph of ductile iron camshaft with six lobes used in this study is shown in Figure 3.4.



Figure 3.4 Profile of ductile iron camshaft

Samples were cut from all 18 lobes of the three different camshafts and were marked A1-A6, B1-B6, C1-C6. Each lobe was labeled using a black marker with an X at

the same location on the lobe for RA/RS measurements. Figure 3.5 shows an individual lobe (B2) together with its dimensions.

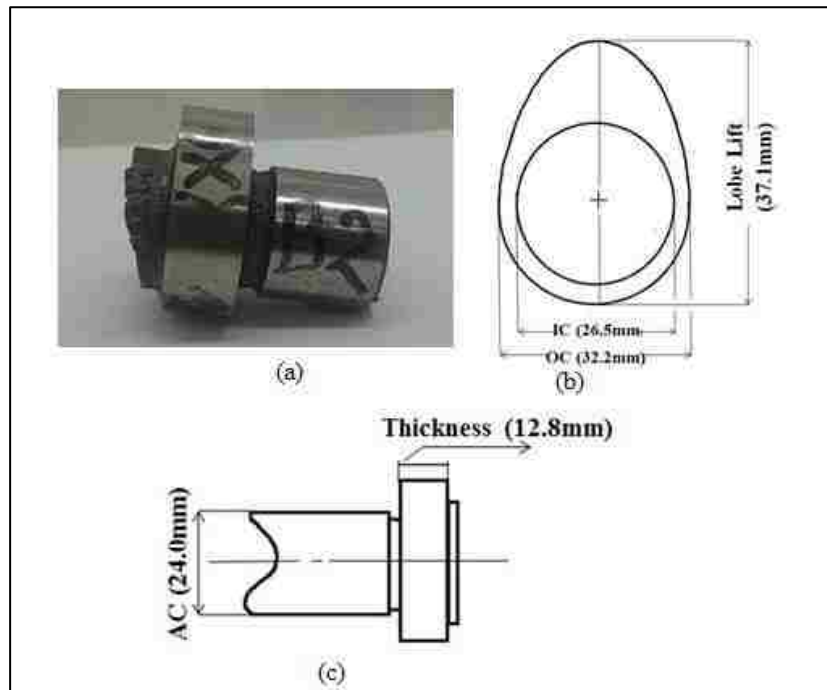


Figure 3.5 Shape and geometry of camshaft lobe, (a) sample B2 with X marked to indicate the position for RA and RS measurements; (b) cam lobe dimensions and geometry; (c) dimension and geometry of cam lobe section.

3.5 Measurement of Retained Austenite (RA) and Residual Stress (RS) by XRD

X-ray Diffraction Methods were used to determine the retained austenite (RA) and residual stress (RS) on the surface of the lobe samples. Two independent certified laboratories, identified as laboratory A and laboratory B, performed the RA & RS measurements on all samples.

3.5.1 Residual Stress Measurement:

All RS measurements were made according to ASTM Standard E915 [66]. Residual stresses in the cam lobes samples were calculated by measuring the lattice deformation of the {211} martensite peak. The x-radiation used was Cr K_{α} with a

wavelength of 0.2291nm. The target power used in Laboratory A was 40 kV and 40 mA; for Laboratory B, the power was 30 kV and 25 mA. The Bragg angle (2θ) was set at 156.4° for both laboratories. In Laboratory A, the relative position of the $\alpha(211)$ peak was measured from ψ angles of -45° to $+45^\circ$ in 5° increments. In Laboratory B, nine different Ψ values were used: $0^\circ, \pm 25.00^\circ, \pm 20.6^\circ, \pm 15.85^\circ$ and $\pm 3.74^\circ$. All the measurements were made using a 1mm collimated spot size at area marked by X as shown in Figure 3.6.



Figure 3.6 The measurement of residual stress using X-ray diffraction method

3.5.2 Retained Austenite Measurement

All RA measurements were performed according to the ASTM Standard E975 [60], using a four-peak method. The relative intensities of the $\alpha(200)$, $\alpha(211)$, $\gamma(200)$, and $\gamma(220)$ peaks were measured, and RA volume fraction was calculated using Equation 3.2 :

$$V \gamma = \frac{\frac{1}{2} \left(\frac{I_{\gamma(200)}}{R_{\gamma(200)}} + \frac{I_{\gamma(220)}}{R_{\gamma(220)}} \right)}{\frac{1}{2} \left(\frac{I_{\gamma(200)}}{R_{\gamma(200)}} + \frac{I_{\gamma(220)}}{R_{\gamma(220)}} \right) + \frac{1}{2} \left(\frac{I_{\alpha(200)}}{R_{\alpha(200)}} + \frac{I_{\alpha(211)}}{R_{\alpha(211)}} \right)} \quad \text{Equation 3.2}$$

The parameter R is proportional to the theoretical integrated intensity. It depends on interplanar spacing (hkl), the Bragg angle, θ , crystal structure, and the composition of

the phase being measured. The R values used for α (200), α (211), γ (200), and γ (220) reflections were 150.22, 19.89, 48.86, and 35.07, respectively. Figure 3.7 shows an example of a typical XRD pattern with all the four peaks indicated.

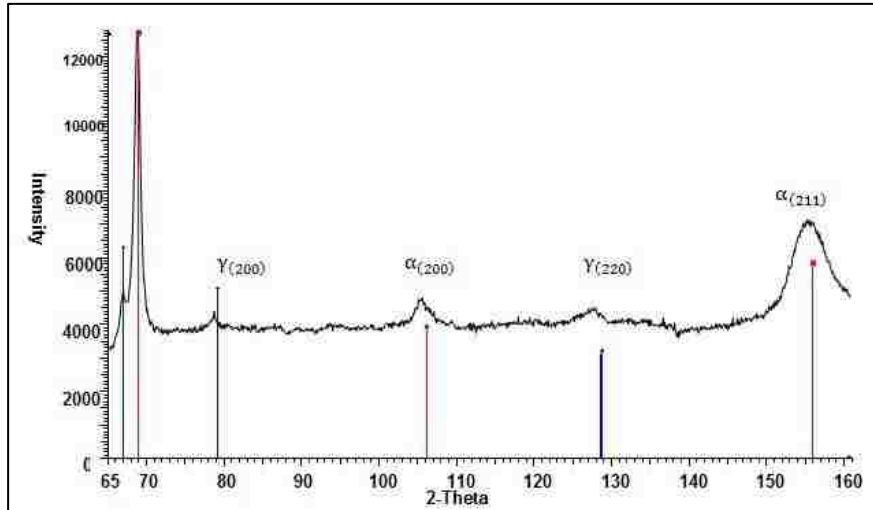


Figure 3.7 XRD pattern for retained austenite measurements

3.6 Metallography:

After the XRD determination of retained austenite and residual stress, samples were cut from the lobes at the designated areas, and hot mounted using mineral filled diallyl phthalate powder. After hot mounting, a formal metallography procedure was used which included the following steps:

- Coarse polishing with a series of SiC papers: 240, 320, 400, 600 grit.
- Intermediate polishing with 9 μm diamond paste on a Buehler ECOMET3 Polisher.
- Fine polishing with 1.0 μm and then 0.05 μm Al_2O_3 powder.

After polishing, the samples were examined optically to determine the graphite distribution. Figure 3.8 shows an optical microscope with a digital imaging system.

A typical microstructure of nodular graphite is shown in Figure 3.9. It exhibits graphite nodules, which are distributed relatively evenly in the matrix.



Figure 3.8 Optical microscope with a digital imaging system

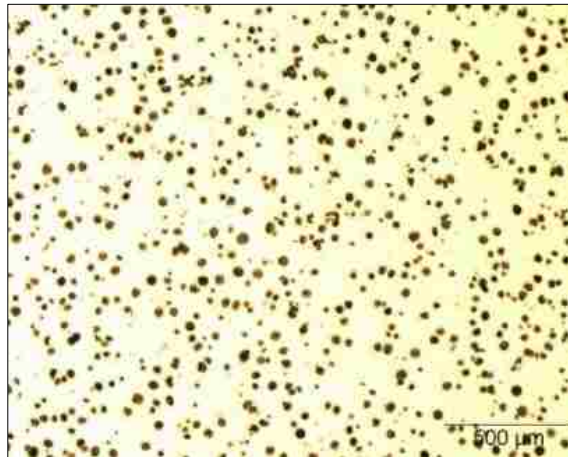


Figure 3.9 Micrographs showing graphite distribution in the matrix

The samples were then etched with 2% Nital (2ml nitric acid in 98ml ethanol) for 12 to 15 seconds to reveal the microstructure of the induction-hardened samples. Two typical microstructures are shown in Figure 3.10

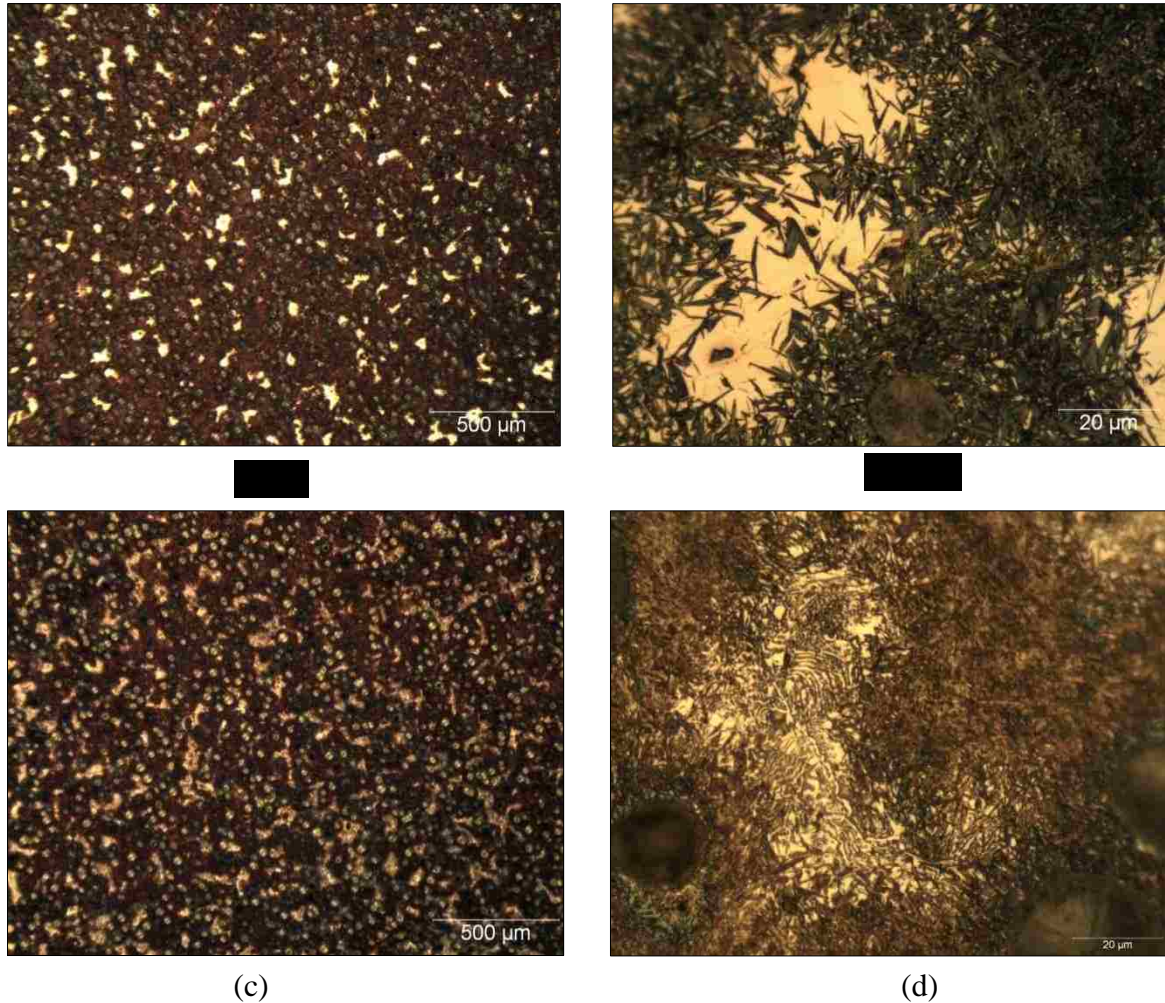


Figure 3.10 Induction hardened lobe 1 (a) 50x (b) 1000x; lobe 2 shows pearlite (c) 50x (d) 1000x.

It can be seen in Figure 3.10(a) and (b) that the microstructure of lobe 1 consists of a martensite matrix (yellow-brown), graphite nodules (black) and austenite islands (white). The retained austenite usually appears white and is isolated in the martensite matrix. There is a very intense colour difference between the retained austenite and the other phases. Usually needle-like martensite is present in the retained austenite islands. However, as a comparison, in Figure 3.10(c) and (d), the retained austenite islands are difficult to see at 50 x magnification; while at 1000x magnification, lamella pearlite (black) is seen to be distributed in the retained austenite island. According to the CCT

curve discussed in section 2.6.2, different cooling rates can produce different microstructures when cooling from austenite. The different microstructures support the idea that the non-symmetrical geometry of the camshaft produced different non-uniform thermal cycling.

3.7 Image Analysis:

A Buehler Omnimet Imaging Analysis Software and Image-Pro Plus Software were used to isolate and measure the area percentage of graphite or retained austenite phases in the different microstructures. The determination of area percentage is based on color difference. When analysing the unetched samples, the dark nodular graphite is distributed in the light matrix; so the color difference is between dark and light. The retained austenite content is also measured by the contrast differences between the white austenite phase and other colored areas. Thus the color threshold setting is especially important for obtaining an accurate result. Because there is a strong contrast difference between the retained austenite and the matrix, this content is readily calculated. Figure 3.11 shows the detailed steps in determining the graphite content of an unetched sample using Image-Pro Plus software.

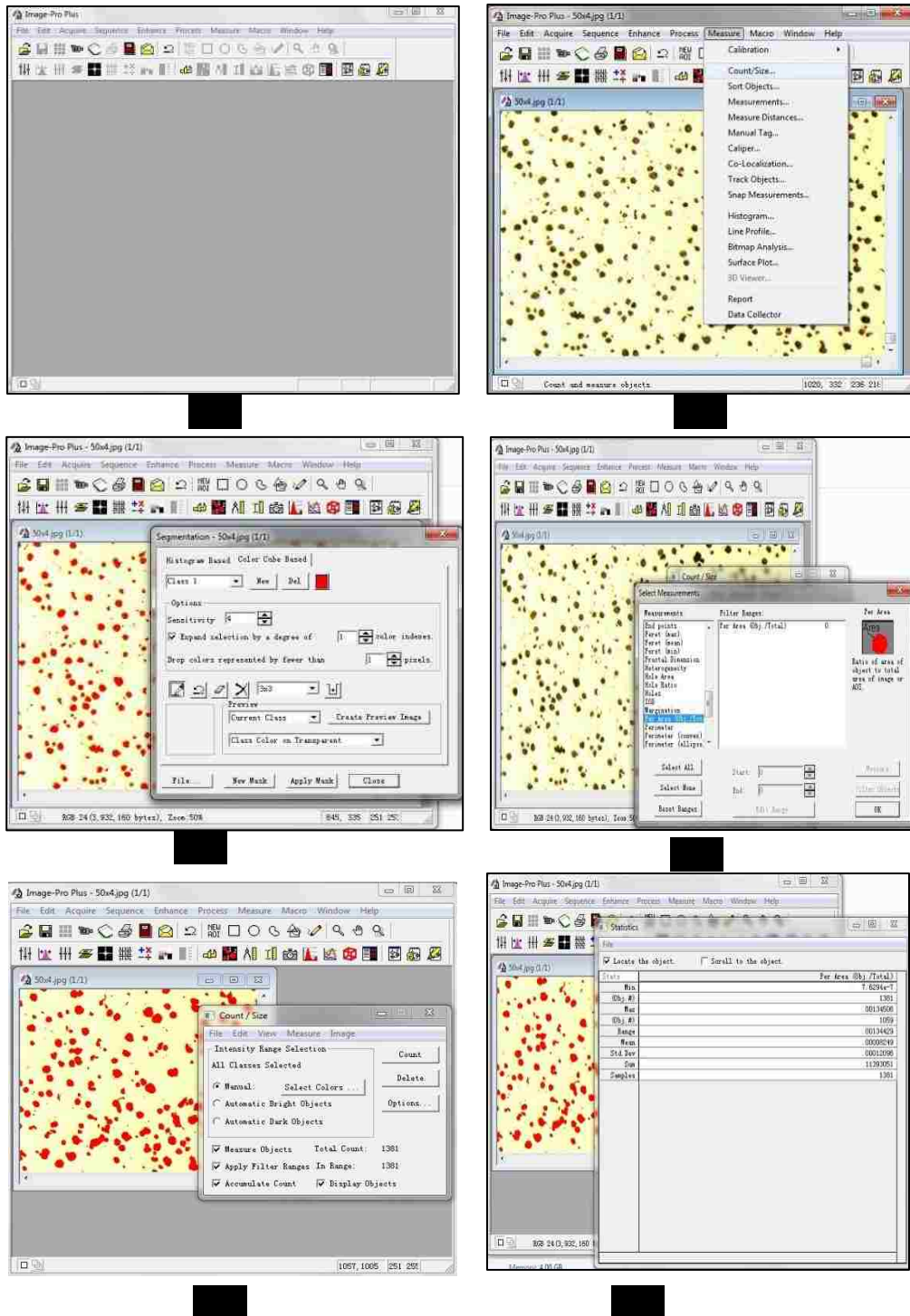


Figure 3.11 Steps showing how to determine graphite content (a) open ImagePro-Plus; (b) Import a picture and click Measure-Count/Size; (c) select the color of graphite (dark); (d) select measurement-Per area (Obj./Total); (e) select “count”; (f) select view-statistics.

50x optical images were selected for graphite content analysis because these images sampled the greatest area. However, for retained austenite content analysis, a 200x magnification was used because at 50x magnification level, it was harder for the software to recognize the colour difference.

Figure 3.12 illustrates the image analysis process. Figure 3.12(a) is an original optical micrograph of the graphite distribution in the matrix; Figure 3.12(b) is the photo after software processing. The color of the graphite is changed from black to red, and the ratio of the red part was measured by the software according to ASTM Standard E1245 [67].

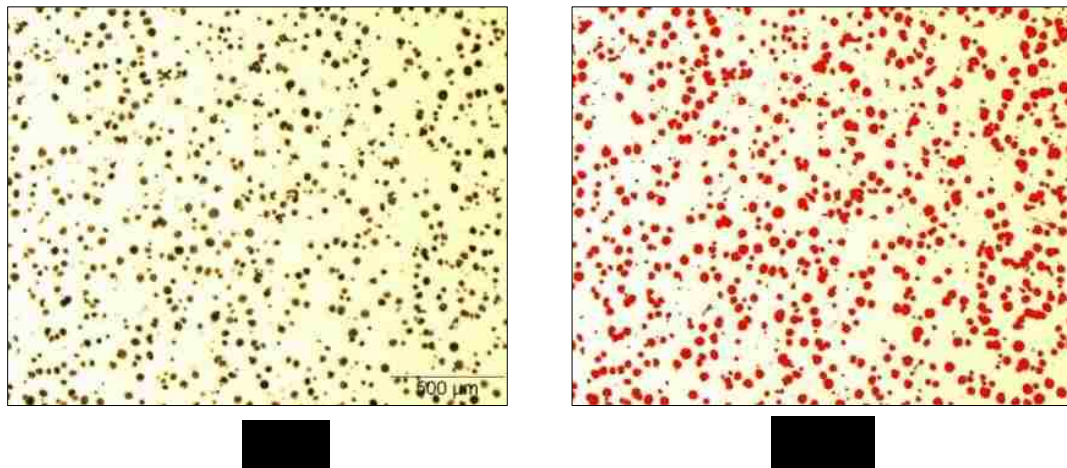


Figure 3.12 Optical image analysis for graphite nodule percentage. (a) original micrograph which shows graphite distribution in the matrix ; (b) after software processing; the area ratio of the red part in the matrix is calculated.

Figure 3.13 shows the microstructure of an etched sample that contains retained austenite, martensite and nodular graphite, and its image analysis. It can be seen that the white area of retained austenite in Figure 3.13(a) has been selected by the software and turned red in Figure 3.13(b). This is an effective way to calculate the retained austenite content.

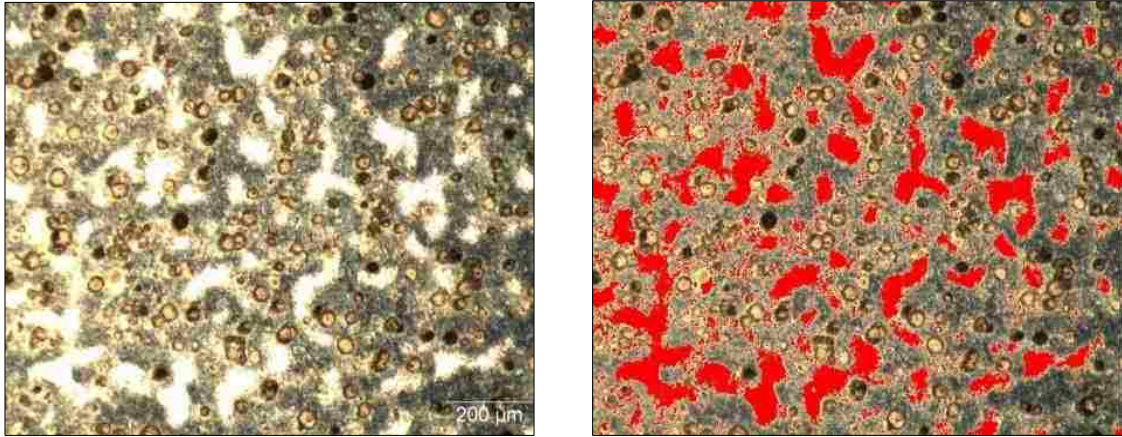


Figure 3.13 Retained austenite determination: (a) image: 2% Nital etching (b) image analysis.

3.8 Hardness Test:

Hardness was determined using a Rockwell C scale (150 kg load; Brale indenter), Figure 3.14. The surfaces of the etched samples were cleaned and checked for surface impurities. Five indentations were done on each sample, and the average hardness result was calculated.



Figure 3.14 Rockwell hardness testing machine.

CHAPTER IV

MICROSTRUCTURE CHARACTERIZATION

This chapter discusses the microstructural observation and characterization of the induction hardened ductile iron samples. Both qualitative and quantitative analysis was performed on the data gathered from optical micrographs for retained austenite and from the software image analysis.

4.1 Graphite Content:

The nodular graphite content measurement was done prior to the retained austenite measurement, Figure 4.1 (a) and (b) show samples B2 and C2 sample for comparison. Both the samples were examined at 50X magnification because the lowest magnification image is useful in more accurately understanding the graphite nodule distribution.

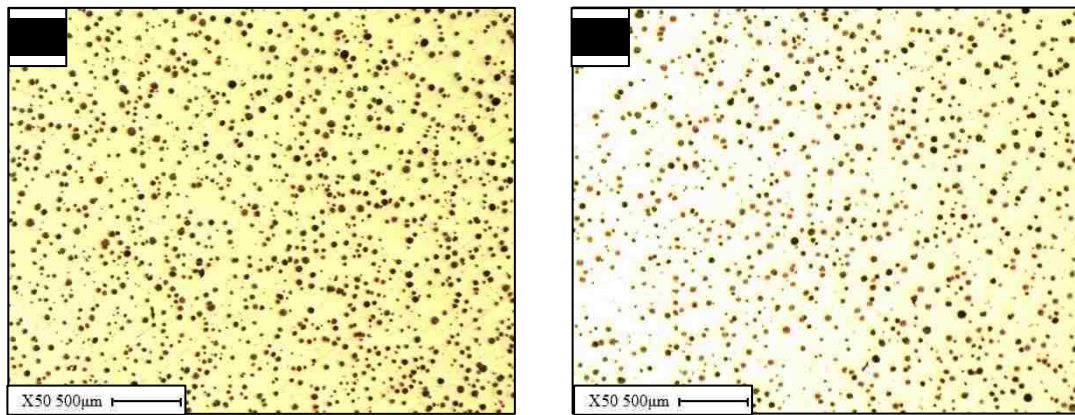


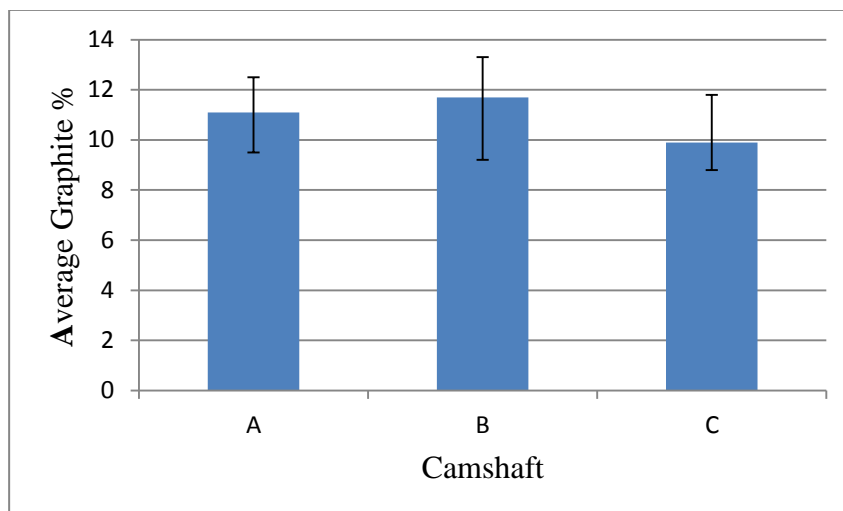
Figure 4.1 Visual inspection of micrographs of the graphite distribution in (a) B2 (b) C2 shows that B2 has a higher graphite density than C2.

The graphite content for all the 18 samples and the average of the three camshafts have been given in Table 4.1 and Figure 4.2. Ten images were used for each sample and an average value has been calculated. It can be seen that although the three camshafts

share the same nominal chemistry, there are differences both from lobe to lobe on the same camshaft as well as from camshaft to camshaft. The difference between the different camshafts is assumed to be due to the difference in induction heating time. Under a longer austenizing time, the carbon that constitutes graphite may be dissolved into the austenite matrix.

Table 4.1 Graphite content of 18 samples by image analysis

Sample	Graphite Content %	Sample	Graphite Content %	Sample	Graphite Content %
A1	11.74 ±0.4	B1	12.34 ±0.3	C1	10.58 ±0.4
A2	10.1 ±0.5	B2	12.76 ±0.4	C2	9.64 ±0.3
A3	11.18 ±1.0	B3	12.46 ±0.7	C3	9.8 ±0.5
A4	11.42 ±0.5	B4	12.82 ±0.5	C4	10.32 ±1.5
A5	11.4 ±1.1	B5	10.39 ±0.3	C5	9.7 ±1.2
A6	10.86 ±0.6	B6	9.76 ±0.5	C6	9.46 ±0.2
A(Average)	11.1	B(Average)	11.7	C(Average)	9.9



*Note: Error bars represent range of data

Figure 4.2 Average graphite content for A, B and C camshafts

4.2 Induction Hardened Ductile Iron Microstructures:

Optical micrographs of the as-cast sample are shown in Figure 4.3. For each sample, two images at 1000x and 200x magnifications are presented. The lower magnification image is useful in understanding the overall phase and graphite nodule distribution. The higher magnification image is required to understand the detailed microstructure.

Figures 4.3 (a-b) show that the as-cast microstructure does not contain any acicular bainitic ferrite or martensite. The as-cast microstructure is predominantly pearlitic (85%). The graphite is mainly nodular in shape and is surrounded by a bright halo of ferrite. This formation of bright ferrite surrounding the dark graphite nodule is often referred to 'Bull's Eye' [54]. There is some ferrite present that is divorced from the graphite nodules, and some present in the pearlite grain boundary regions.

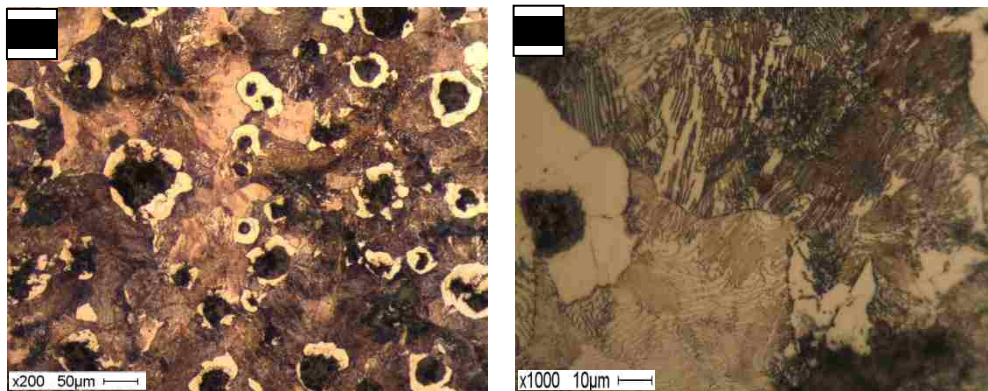


Figure 4.3 Optical micrographs of as-cast samples (a) 200x (b) 1000x.

Figures 4.4-4.13 presents the microstructures of the induction hardened ductile iron samples. These micrographs are presented in order of increasing RA content from 7%-9% through 23%-27%. For each sample, images at 200x and 1000x magnification are presented. Large microstructural differences between lobes and between camshafts can be noted.

Figure 4.4 (a) shows that white retained austenite island lies inside the brown colored martensite matrix. Nodular graphite exhibits a grey-white color which makes it near transparent. At high magnification, Figure 4.4 (b) reveals the matrix to contain needle-like martensite; there are additional martensite needles in the retained austenite island. Figures 4.4 (c) to (g) shows similar microconstituents; the color of the matrix was noted to vary from brown to blue depending on the extent of the etching.

From Figure 4.5 to Figure 4.12, the white areas of micrographs are noted to increase with increasing retained austenite content. Also, they are evenly distributed in the martensite matrix. The same camshafts can exhibit large differences in %RA; camshaft lobes A3 and A1 contain 10.9 % RA vs 23.2 %, respectively. Even the same sample, B4, had % RA values ranging from 12.0% to 26.7%. An average value from at least 20 micrographs was used to increase the accuracy of the average value.

Figure 4.5 (b) shows that microconstituents other than martensite can exist in retained austenite island, such as pearlite and possible ferrite. This situation was noted to just occur in a small amount of micrographs; however, it could obscure the retained austenite island and make it difficult to measure for the software. The causes of these microconstituents include interrupted or slack quenching or incomplete dissolution of the pearlite during austenization.

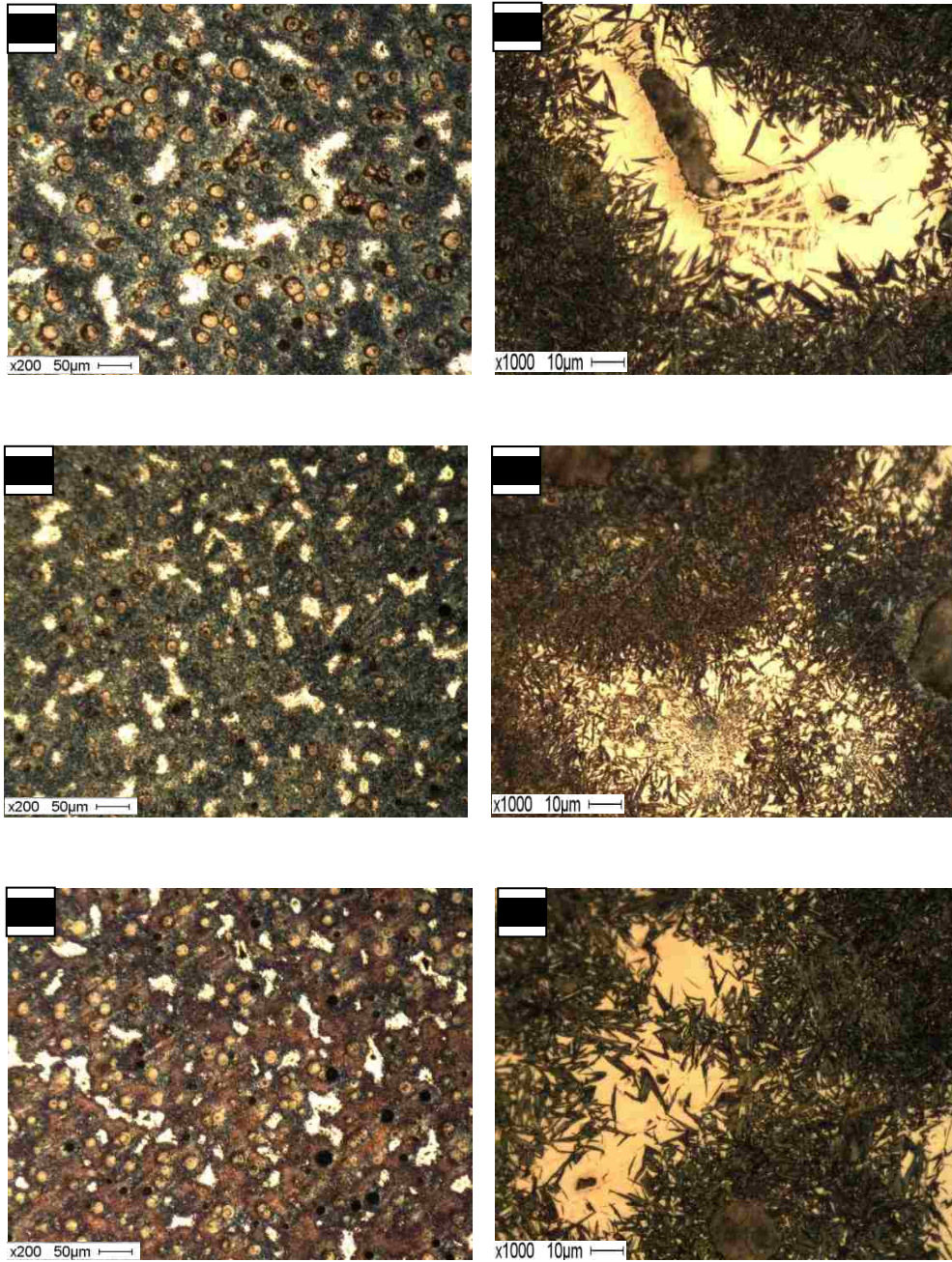


Figure 4.4 Optical micrographs of samples containing RA from 7%-9%, a-b) Sample A1, 7.1 % RA, c-d) Sample B1, 8.2%RA e-f) Sample B2, 8.9% RA

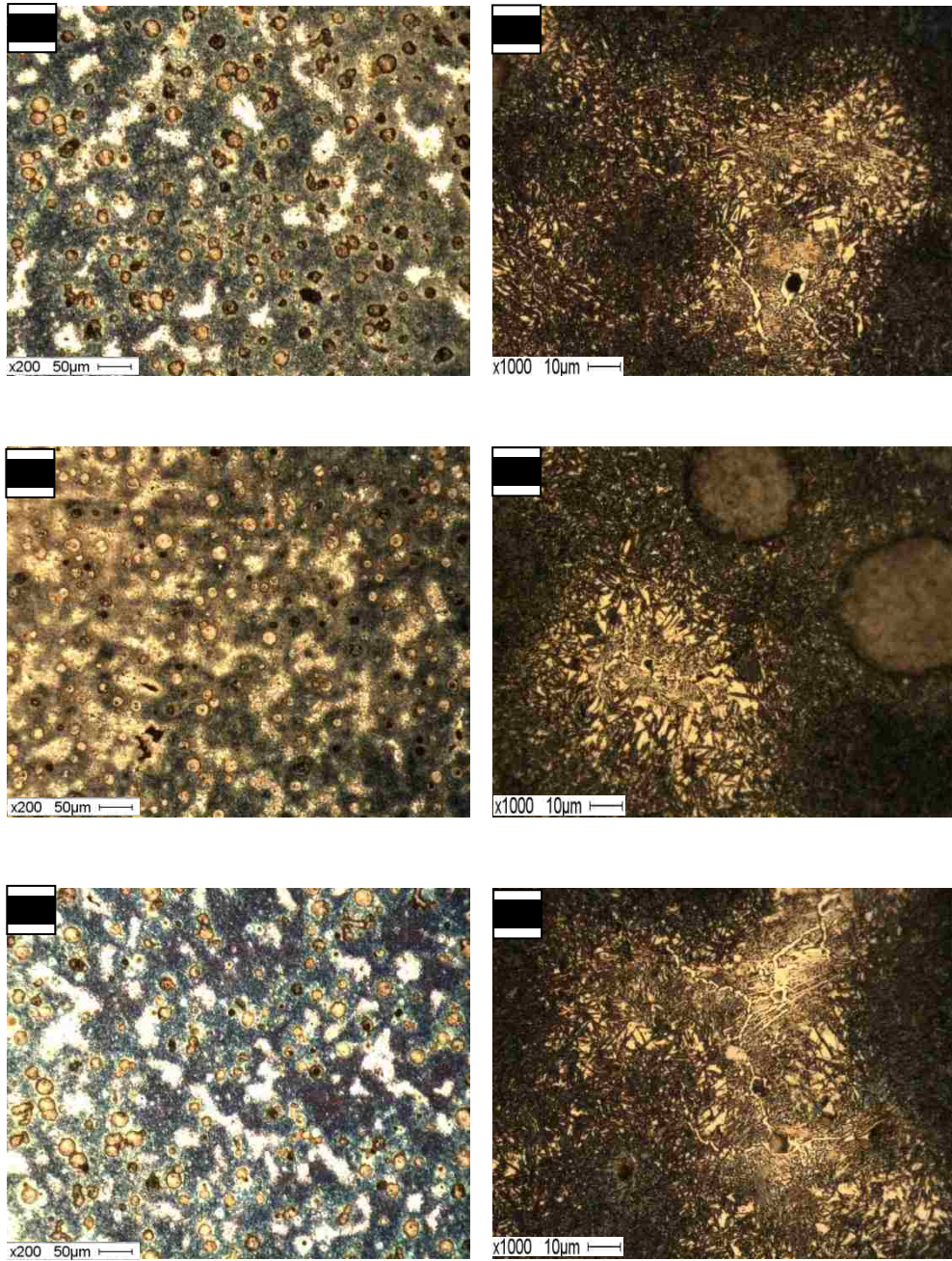


Figure 4.5 Optical micrographs of samples containing RA from 9%-11%, a-b) Sample A3, 9.8 % RA, c-d) Sample C5, 10.3%RA e-f) Sample B2, 10.9% RA

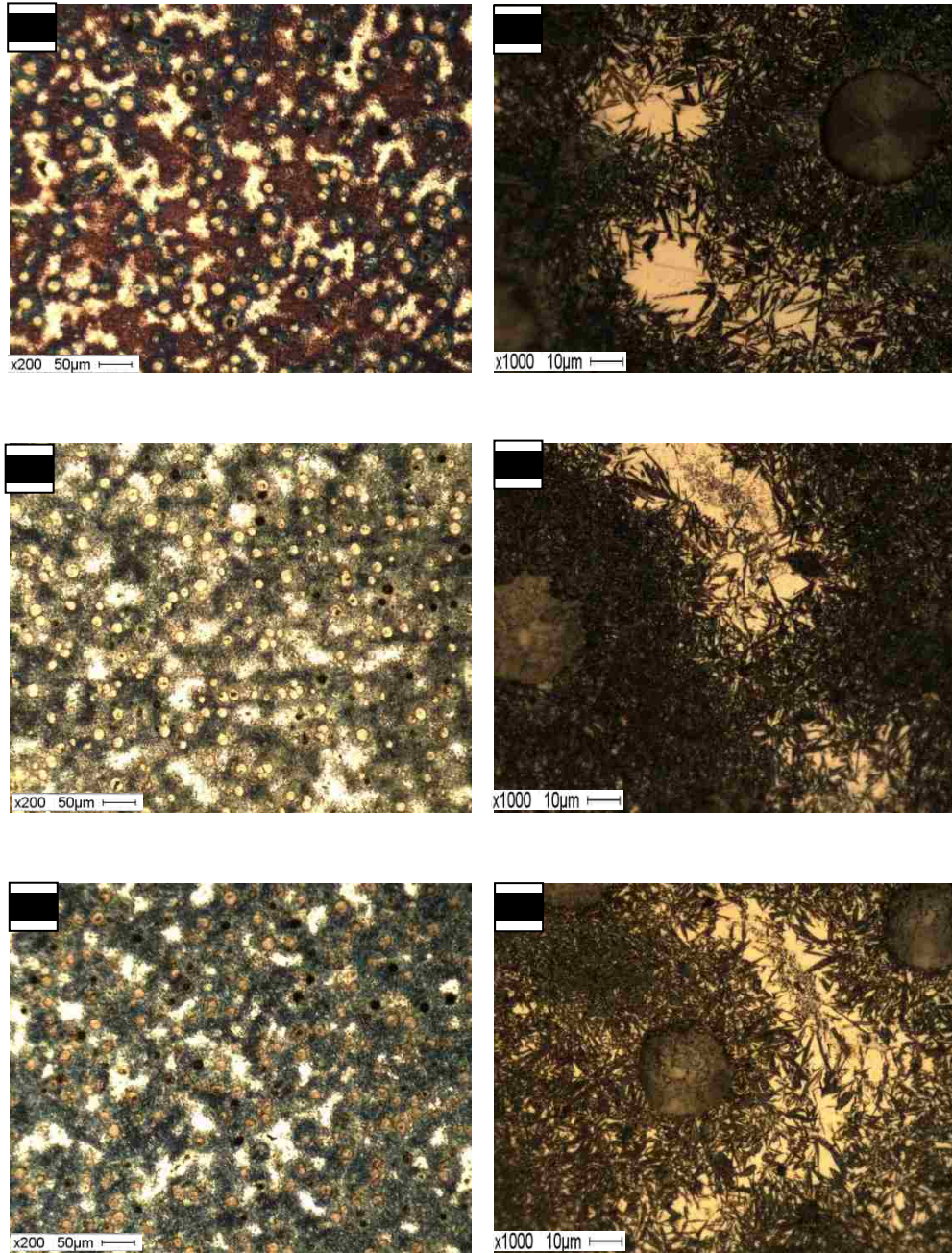


Figure 4.6 Optical micrographs of samples containing RA from 11%-13%, a-b) Sample A5, 11.7 % RA, c-d) Sample C2, 12.3%RA e-f) Sample B2, 12.9% RA

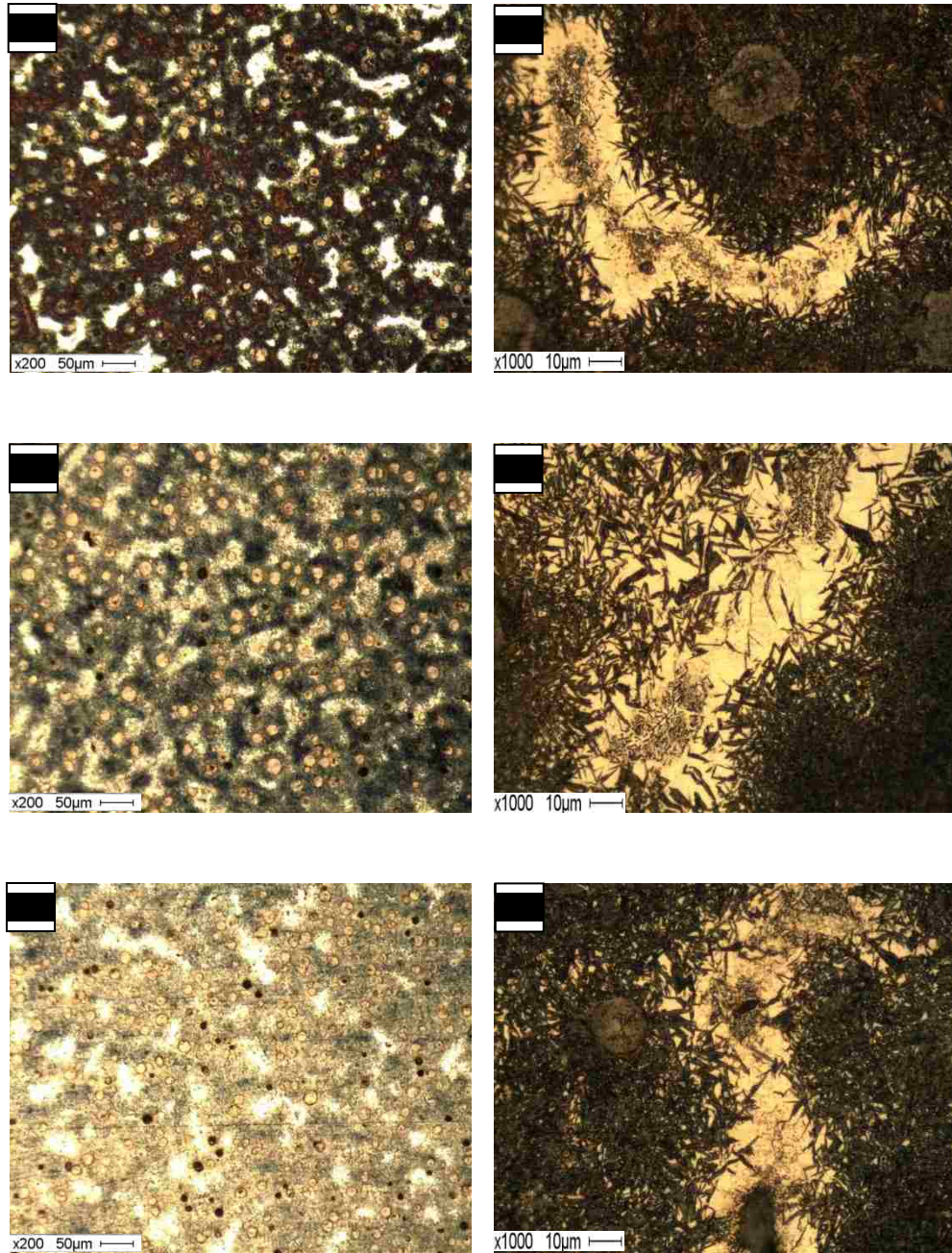


Figure 4.7 Optical micrographs of samples containing RA from 13%-15%, a-b) Sample B6, 13.7 % RA, c-d) Sample C5, 14.1%RA e-f) Sample C4, 15.0% RA

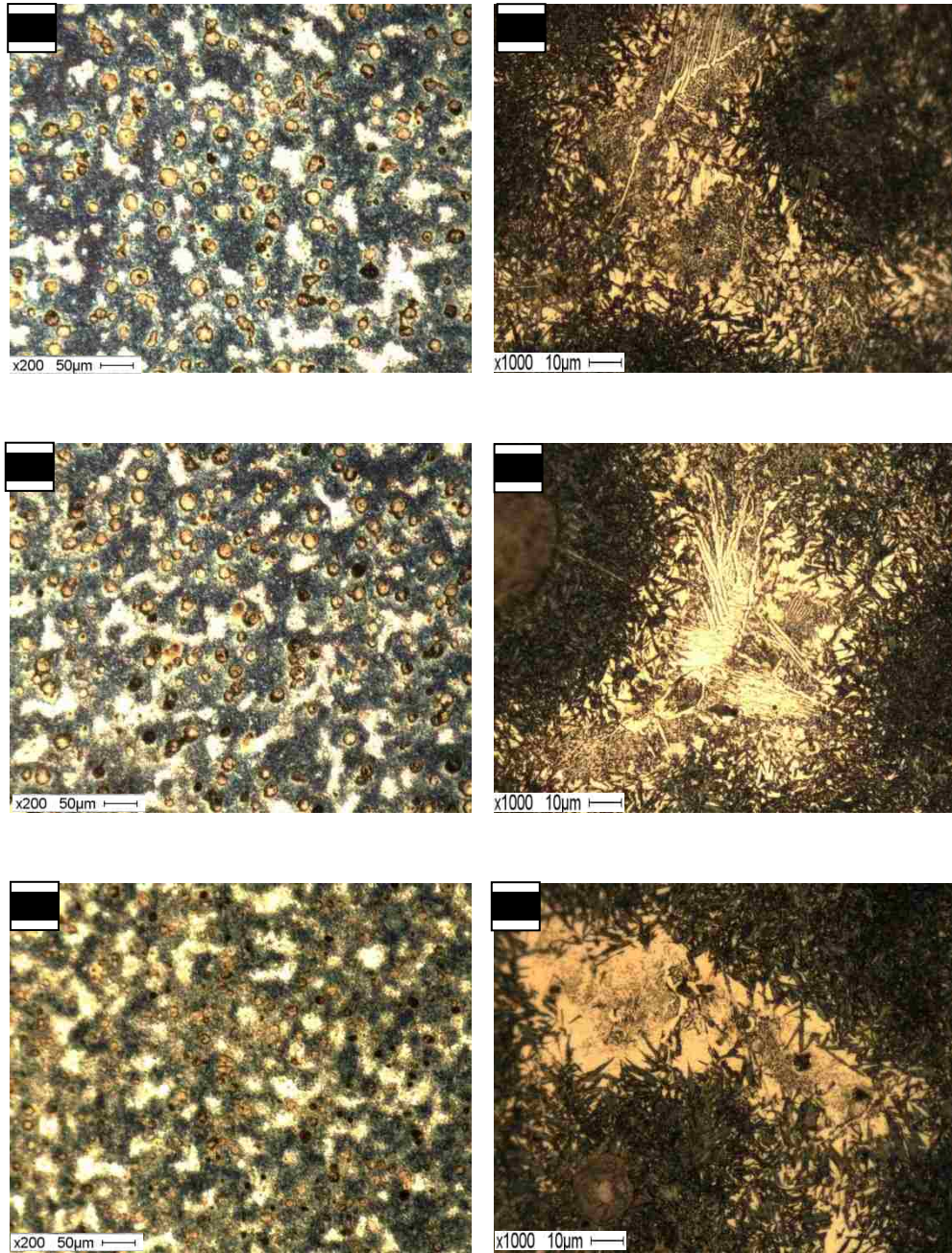


Figure 4.8 Optical micrographs of samples containing RA from 15%-17%, a-b) Sample A2, 15.2 % RA, c-d) Sample A3, 16.1%RA e-f) Sample B4, 16.9% RA

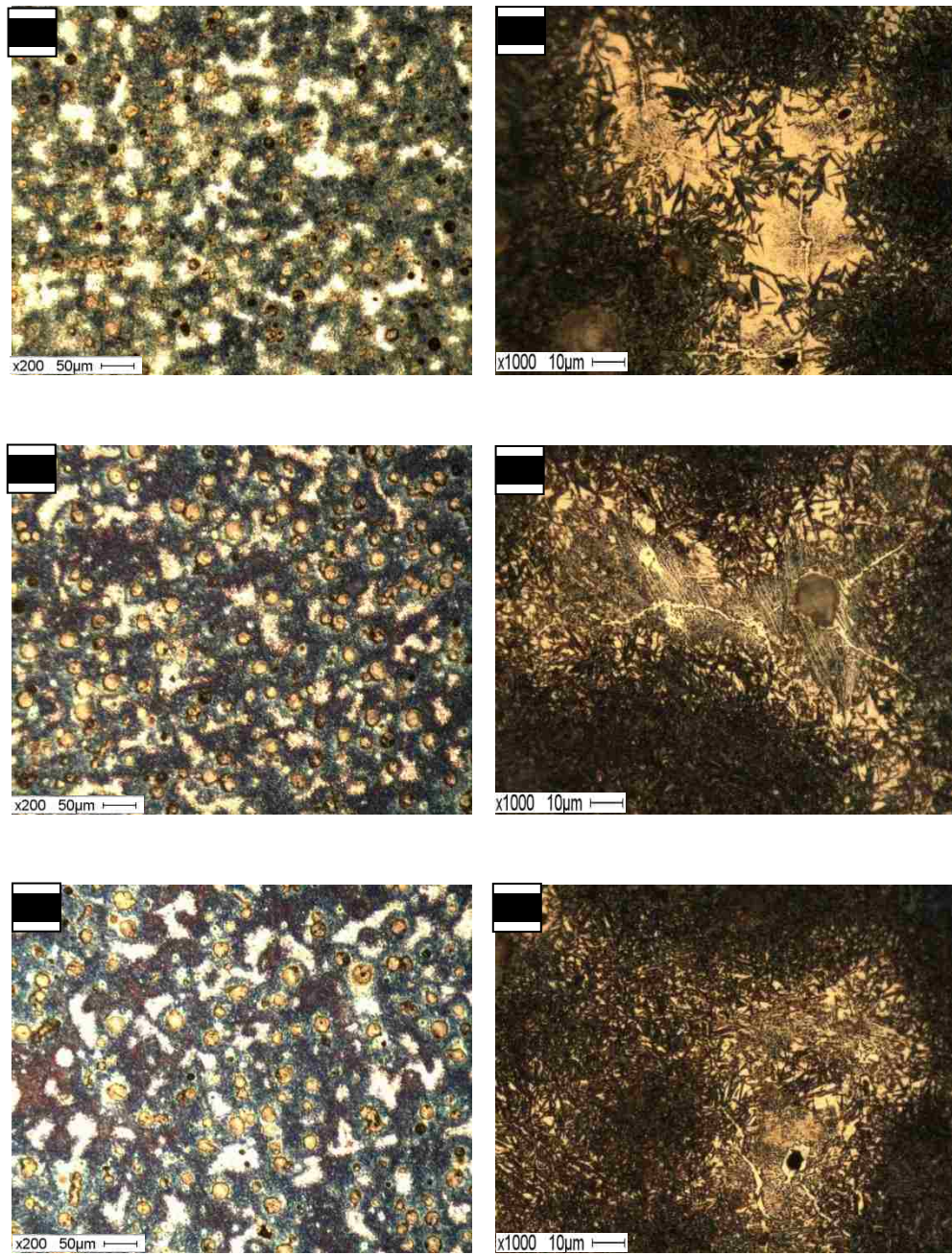


Figure 4.9 Optical micrographs of samples containing RA from 17%-19%, a-b) Sample B4, 17.8 % RA, c-d) Sample A3, 18.3%RA e-f) Sample A2, 18.9% RA

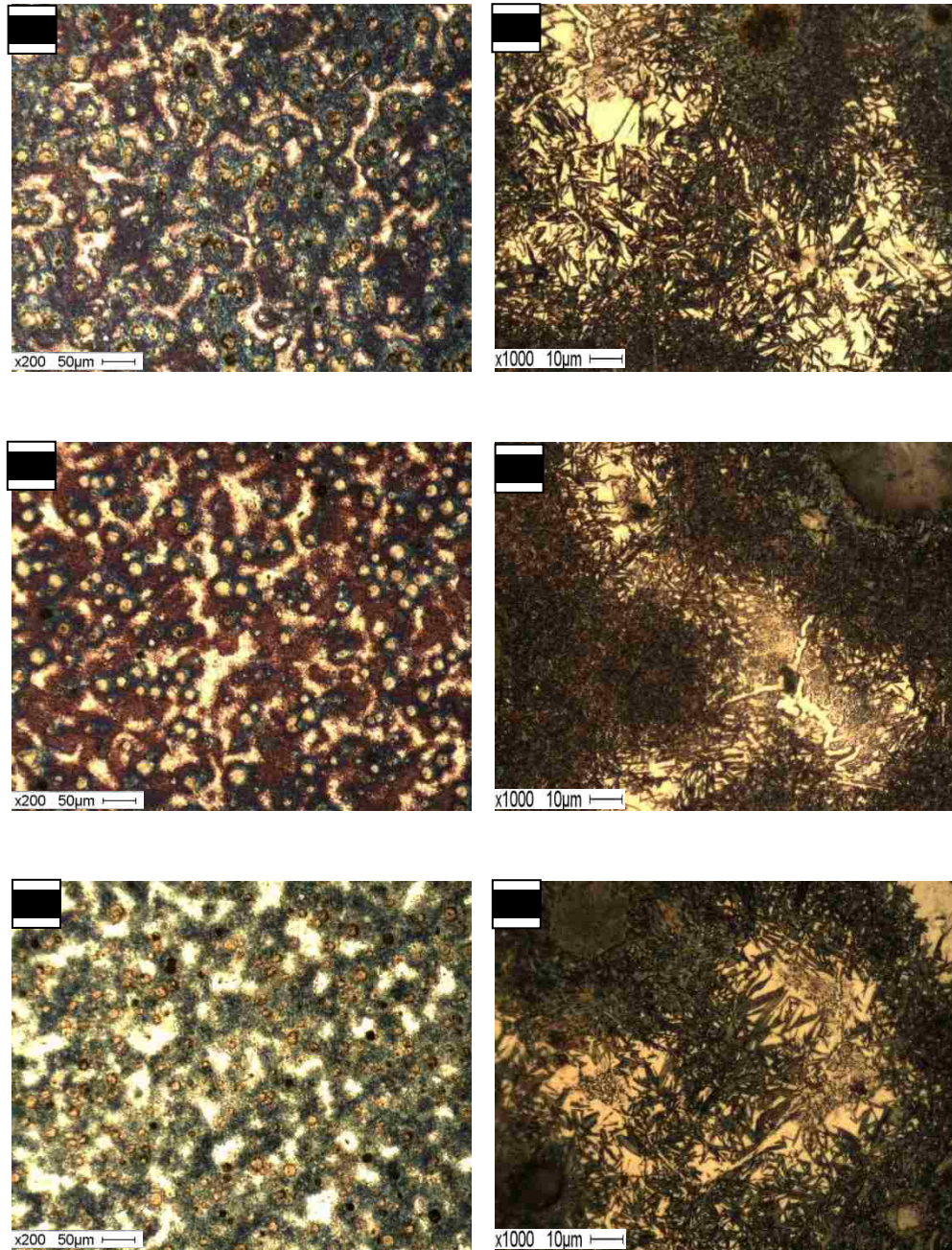


Figure 4.10 Optical micrographs of samples containing RA from 19%-21%, a-b) Sample A2, 19.4 % RA, c-d) Sample A5, 20.6%RA e-f) Sample B4, 21.0% RA

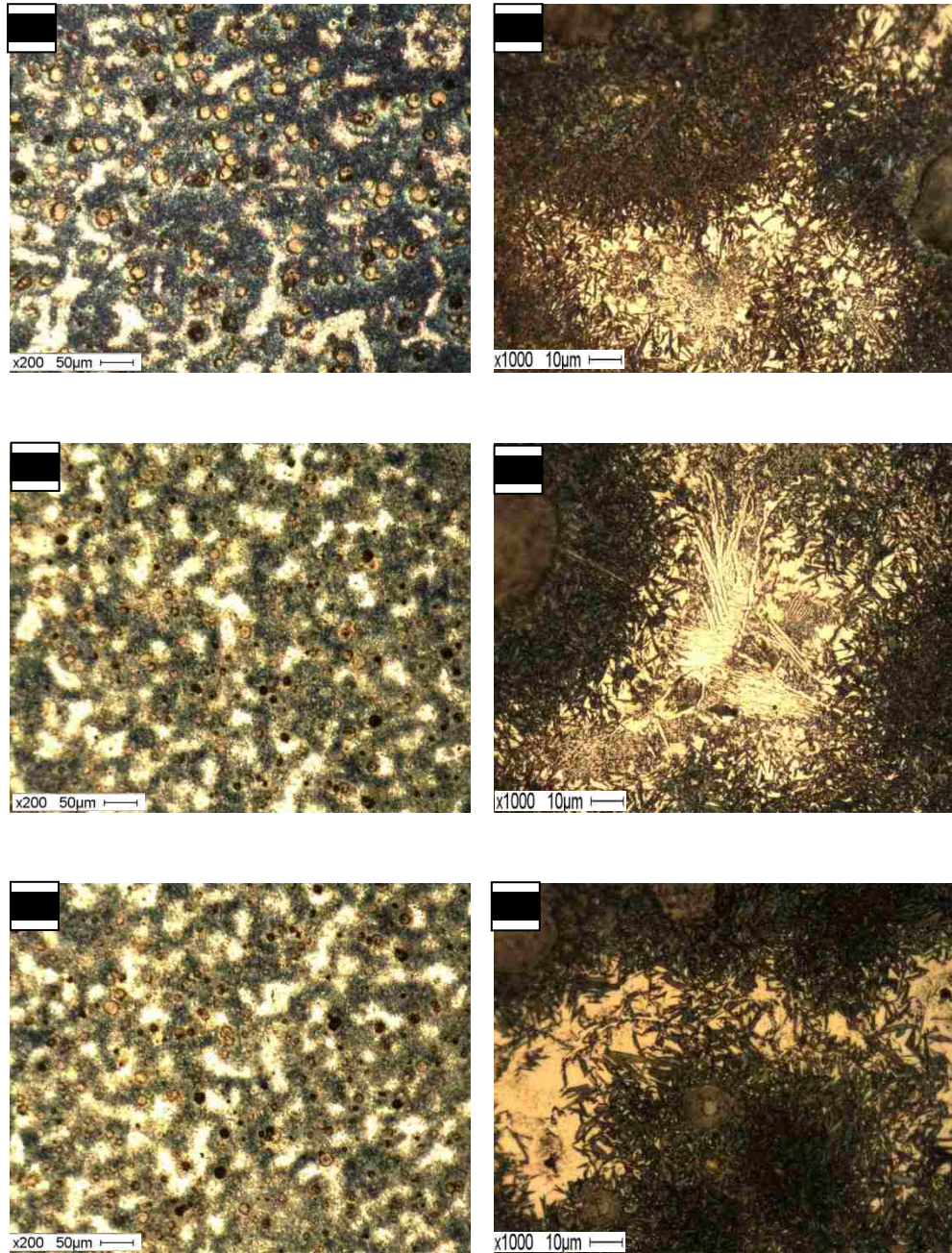


Figure 4.11 Optical micrographs of samples containing RA from 21%-23%, a-b) Sample A3, 21.2 % RA, c-d) Sample B4, 22.3%RA e-f) Sample B4, 23.0% RA

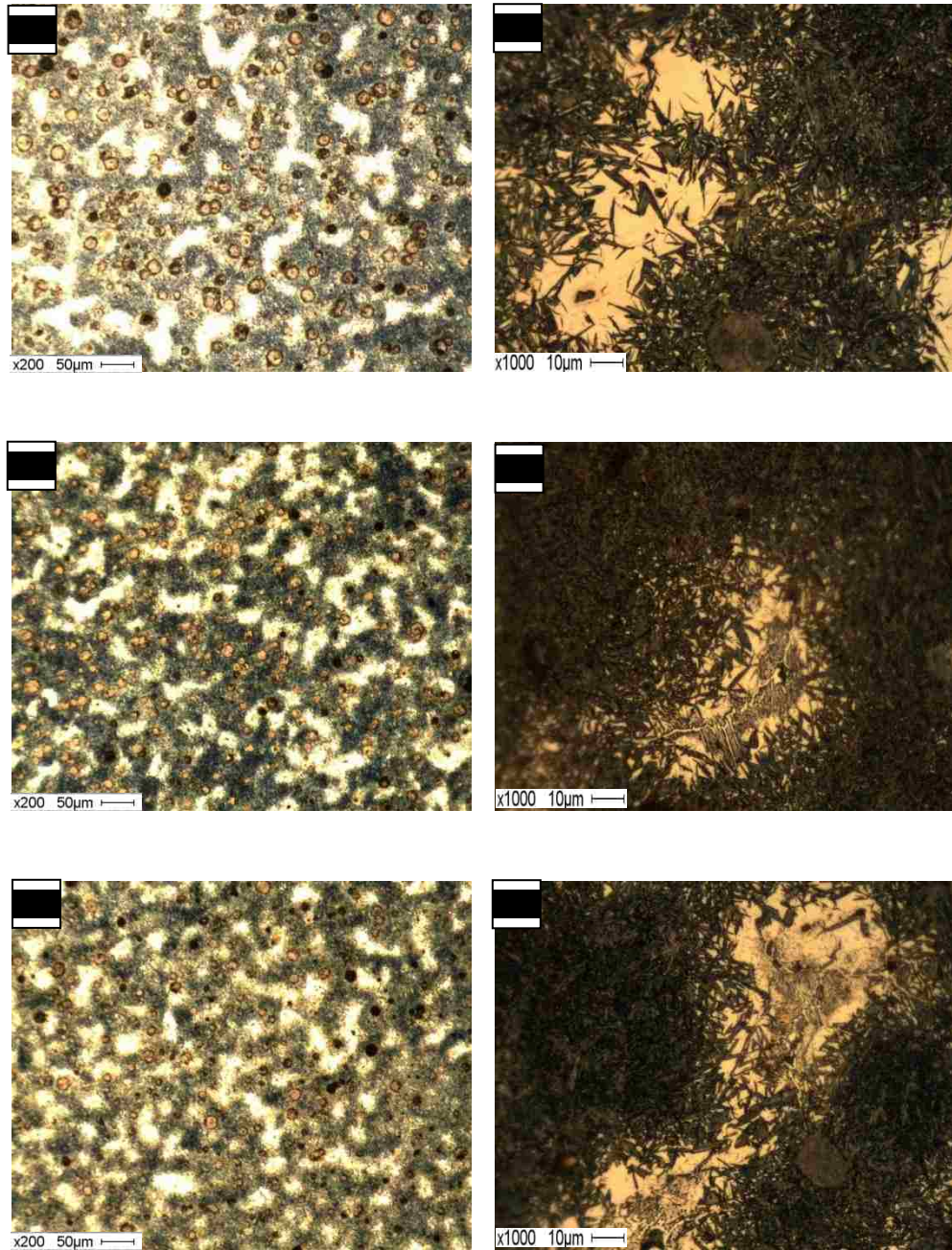


Figure 4.12 Optical micrographs of samples containing RA from 23%-27%, a-b) Sample A3, 23.3 % RA, c-d) Sample B4 , 23.6%RA e-f) Sample B4, 26.1% RA

4.3 Retained Austenite Analysis:

The retained austenite content values measured by optical metallography are summarized in Table 4.2. An average value of 20 micrographs was used when calculating the RA content; the standard deviation is provided for each average.

Table 4.2 Volume % retained austenite for 18 samples by OM.

Sample	RA Content %	Sample	RA Content %	Sample	RA Content %
A1	13.3 ±2.9	B1	12.9 ±3.2	C1	11.7 ±3.8
A2	15.7 ±1.2	B2	15.1 ±2.1	C2	12.8 ±2.4
A3	13.2 ±1.8	B3	12.7 ±3.7	C3	12.0 ±3.7
A4	14.2 ±2.5	B4	19.1 ±7.4	C4	11.3 ±1.5
A5	15.5 ±3.2	B5	13.7 ±4.2	C5	12.8 ±1.2
A6	11.4 ±4.1	B6	12.1 ±2.7	C6	11.5 ±1.9
A(Average)	14.2	B(Average)	14.4	C(Average)	12.0

The average % retained austenite on each camshaft is plotted in Figure 4.13.

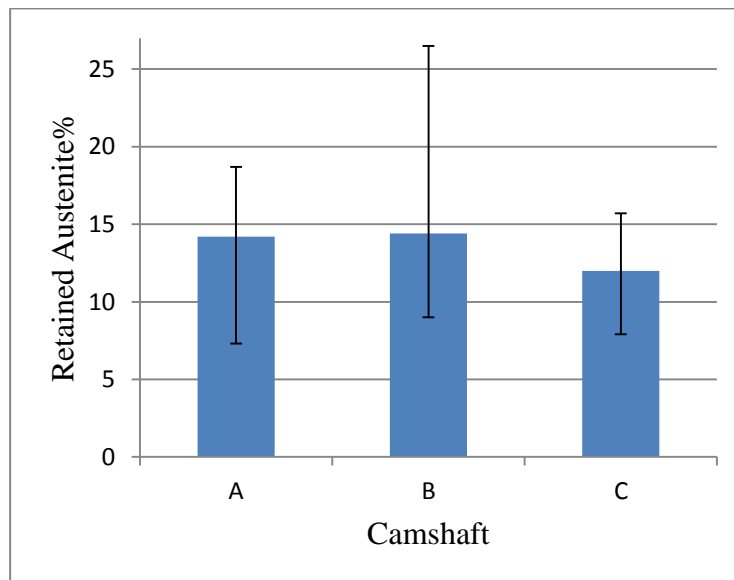


Figure 4.13 Average retained austenite content for camshafts A, B and C

Camshafts A and B have similar RA contents, which is 2 % higher than that for camshaft C. As previously noted, camshafts A and B also have similar graphite contents, which were also higher than that for camshaft C. The relationship between retained austenite content and nodular graphite content is given in Figure 4.14:

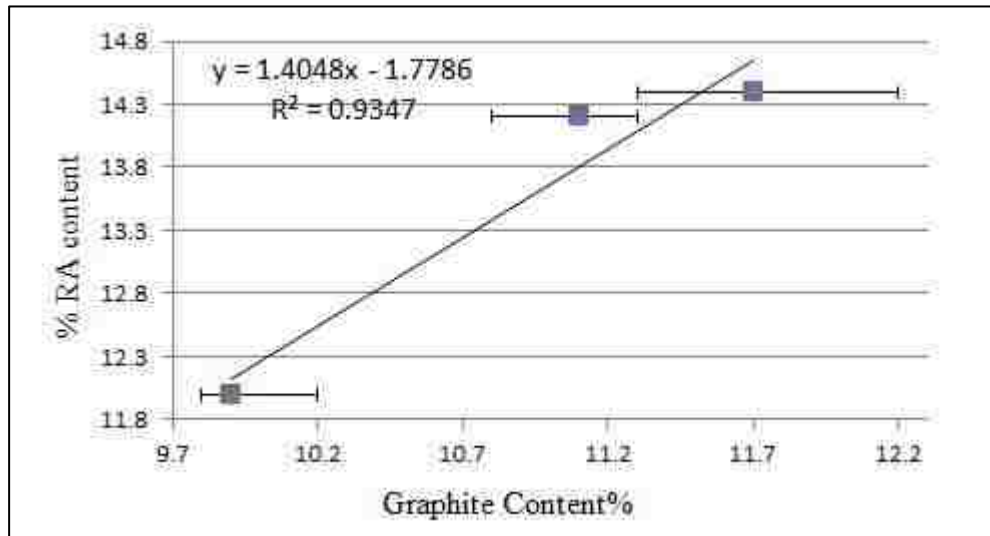


Figure 4.14 Relationship between average retained austenite content and graphite content in camshafts A, B and C

It can be seen from Figure 4.14 that the amount of retained austenite increases with an increase in nodular graphite content, according to Equation 4.1:

$$Pct_{\gamma} = 1.4048 * Pct_{graphite} - 1.7786 \quad \text{Equation 4.1}$$

Theory tells us that during the cooling process of steels, a higher amount of carbon in the austenite matrix stabilizes the austenite phase and prevents it from transforming into martensite. However, the reason why it behaves like this is because the samples used are ductile iron, and there might be carbides and pearlite present in the retained austenite island after the cooling process. Given the large variations in RA content, it is difficult to explain why the RA content is apparently dependent on the nodular graphite content.

It is illustrative to examine the retained austenite profile of each camshaft, since all the camshafts have six lobes (A1-A6, B1-B6, C1-C6) and the same dimensions: the only difference is the induction heating time. The comparison of RA content of all lobes with error bars in camshafts A,B and C is shown in Figures 4.15(a) and (b).

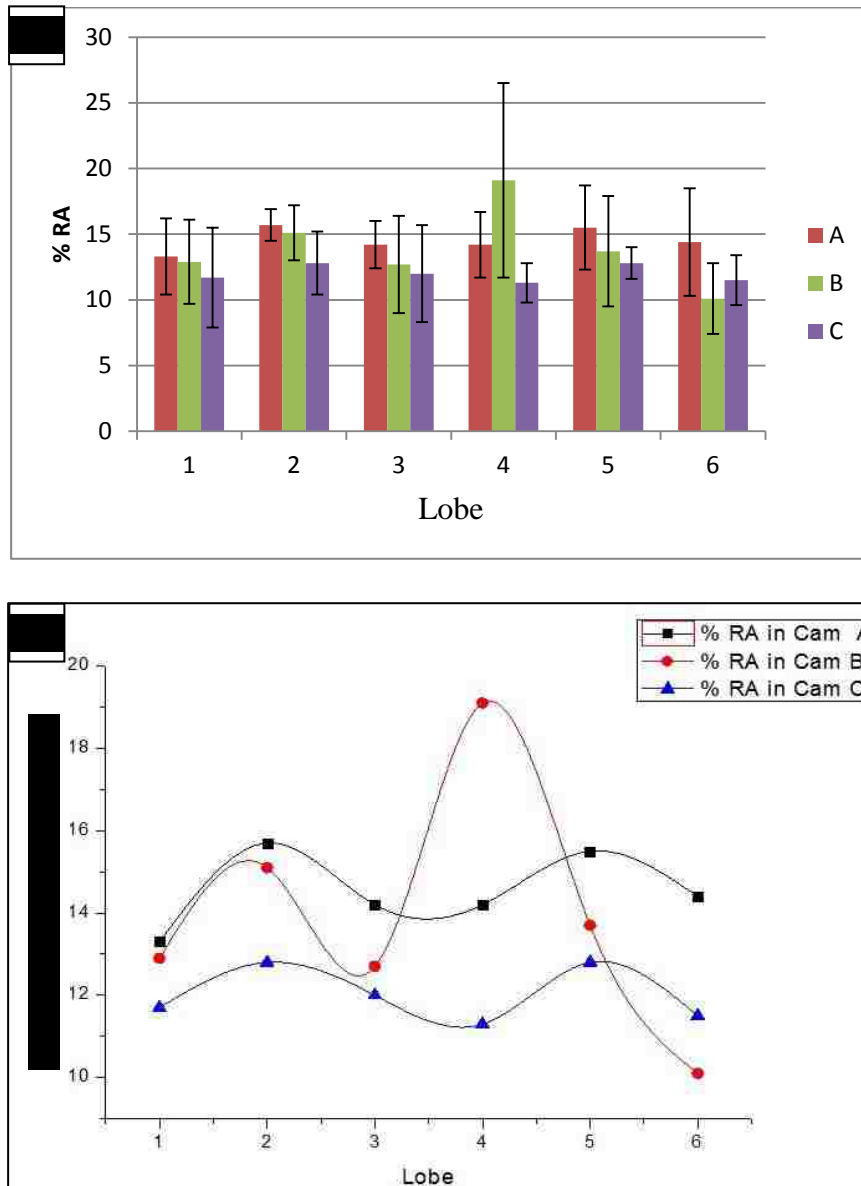


Figure 4.15 (a) RA% for all the samples (b) retained austenite content in three camshafts

From Figure 4.15 (a), we can see that all samples have a fluctuation of RA content.

Figure 4.15 (b) shows that camshafts A and C show a similar variability of retained

austenite content with lobe number, although camshaft C always has a lower retained austenite content than camshaft A. However, camshaft B shows a somewhat different behavior although it is only the RA content of Lobe B4 that is very much higher. B4 exhibits a wide range of retained austenite values from 11.7% to 26.5%, with an average value 19.1%.

4.4 Summary

The main conclusions drawn from the microstructural analysis are as follows:

1. Induction hardened samples have a microstructure consisting of a needle-like martensite matrix, retained austenite islands, and nodular graphite. In some instances, the retained austenite contains lamellar pearlite.
2. Different camshafts contain varying nodular graphite and retained austenite contents and the RA content can vary from lobe to lobe in the same camshaft.
3. An increase in nodular graphite seems to be associated with the formation of retained austenite. However, scatter in the data and a multicomponent makes it difficult to determine a simple cause and effect mechanism.

CHAPTER V

ANALYSIS OF RELATIONSHIPS BETWEEN RA, RS AND HARDNESS

This chapter first examines the relationship between RS (XRD) and RA (XRD & OM), then the relationship between RA (XRD) & RA (OM) and finally RA (OM) and hardness.

5.1 RA and RS by XRD:

Table 5.1 gives the RA contents of all 18 samples measured by X-ray diffraction in two laboratories (A and B), From Table 5.1 it can be seen that the data differs on the same sample between the two laboratories.

Table 5.1 RA content for 18 samples measured by laboratories A and B

Sample	% RA in Lab		Sample	% RA in Lab		Sample	% RA in Lab	
	A	B*		A	B*		A	B*
A1	12.0 ±2.0	17.7	B1	23.0 ±2.0	22.6	C1	15.0 ±2.0	20.9
A2	14.0 ±2.0	19.8	B2	19.0 ±2.0	26.5	C2	17.0 ±2.0	18.0
A3	14.0 ±1.0	20.6	B3	19.0 ±1.0	24.9	C3	18.0 ±1.0	21.6
A4	13.0 ±1.0	17.6	B4	23.0 ±2.0	34.7	C4	17.0 ±1.0	23.8
A5	16.0 ±2.0	22.9	B5	18.0 ±2.0	23.7	C5	16.0 ±2.0	22.1
A6	14.0 ±2.0	24.1	B6	18.0 ±1.0	26.2	C6	15.0 ±2.0	18.5

* Average of 3 values

It can be seen that the largest differences in the values of RA by the two independent laboratories are for samples A6 and B4. The data in Table 5.1 are plotted in Figure 5.1 to aid in the comparison:

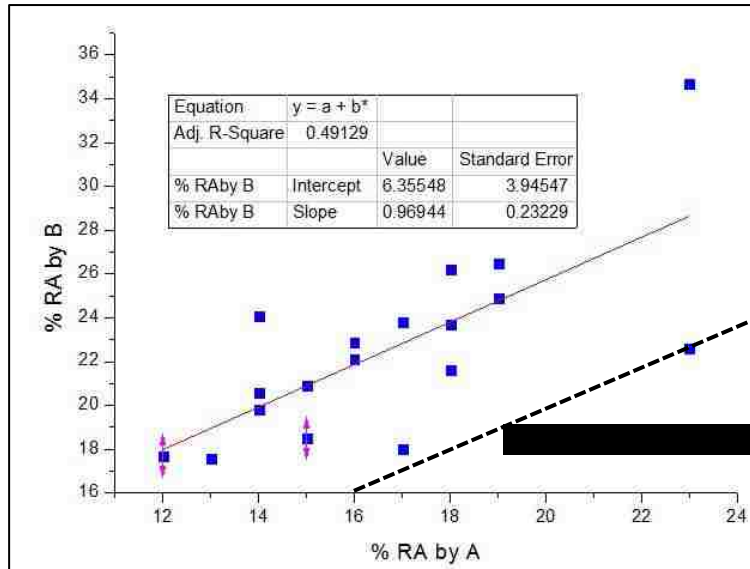


Figure 5.1 Relationship of RA valued measured from two independent laboratories named A and B

It can be seen that from Figure 5.1 although RA measured by Lab B is always larger than that measured by Lab A, there is a relationship which is given by Equation 5.1:

$$RA_{lab\ B} = 0.9694 * RA_{lab\ A} + 6.3555 \quad \text{Equation 5.1}$$

However, the R^2 value is 0.49, so that the correlation is not that good. The variation in RA contents determined by different laboratories is not unusual [51, 52] and has, at least partially, been related to specimen preparation [52].

Then residual stresses have also been measured by X-ray diffraction. Values for the 18 samples are given in Table 5.2

Table 5.2 RS for 18 samples measured by laboratories A and B

Spl	RS (ksi)		Spl	RS (ksi)		Spl	RS (ksi)	
	Lab A	Lab B		Lab A	Lab B		Lab A	Lab B
A1	-68±1	-70.0±3.74	B1	-57±1	-96.2±8.40	C1	-78±1	-106.1±4.60
A2	-56±1	-78.5±4.55	B2	-70±1	-94.1±5.45	C2	-73±2	-110.4±3.90
A3	-61±2	-75.1±4.61	B3	-69±2	-67.1±4.42	C3	-69±2	-68.9±3.54
A4	-62±1	-82.8±3.00	B4	-50±1	-62.4±8.06	C4	-79±2	-77.0±4.93
A5	-62±1	-82.0±3.96	B5	-69±2	-64.4±4.13	C5	-69±2	-83.1±3.74
A6	-63±1	-70.7±3.41	B6	-96±3	-79.2±8.25	C6	-72±1	-72.5±6.32

All the RS values are negative, which means that after induction hardening, all surface stresses are compressive stresses. This is beneficial in terms of contact fatigue performance [2, 27]. A correlation of the RS values obtained from laboratories A and B is shown in Figure 5.2:

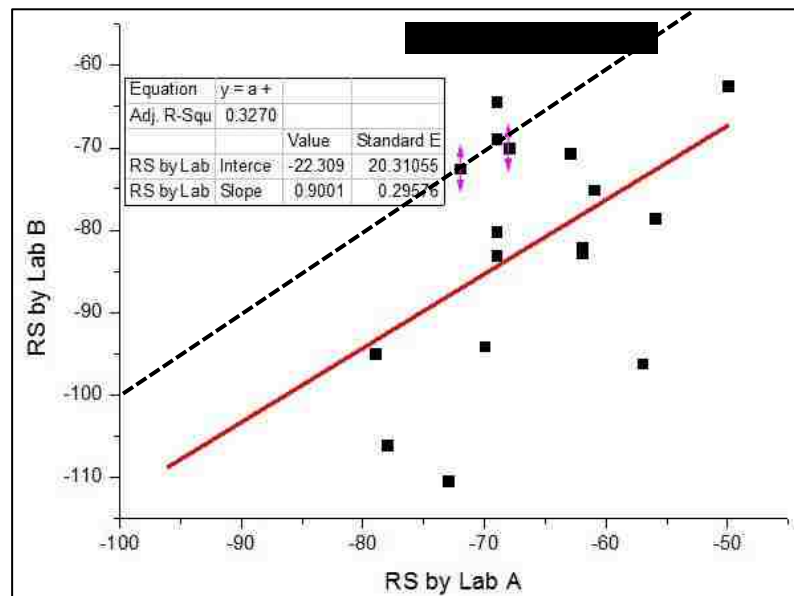


Figure 5.2 Relationship of RS measured by two independent laboratories A and B(ksi)

It can be seen from Figure 5.2 that RS values from Lab B are in general higher magnitude than for Lab A, although there are variations between sample to sample. The trend is similar to that for RA shown in Figure 5.1. The relationship between the two values of RS is given by Equation 5.2:

$$RS_{lab\ B} = 0.9001 * RS_{lab\ A} - 22.309 \quad \text{Equation 5.2}$$

It should be noted that R² value is 0.33. In order to compare the two independent laboratories, the measured residual stresses have been divided into 5 ranges: -50 to -65 ksi (R1), -65 to -75 ksi (R2), -75 to -85 ksi (R3), -85 to -95 ksi (R4) and -95 to -115 ksi (R5). The average RA values corresponding to these RS values plotted against RS (range) values between laboratories A and B in Figure 5.3:

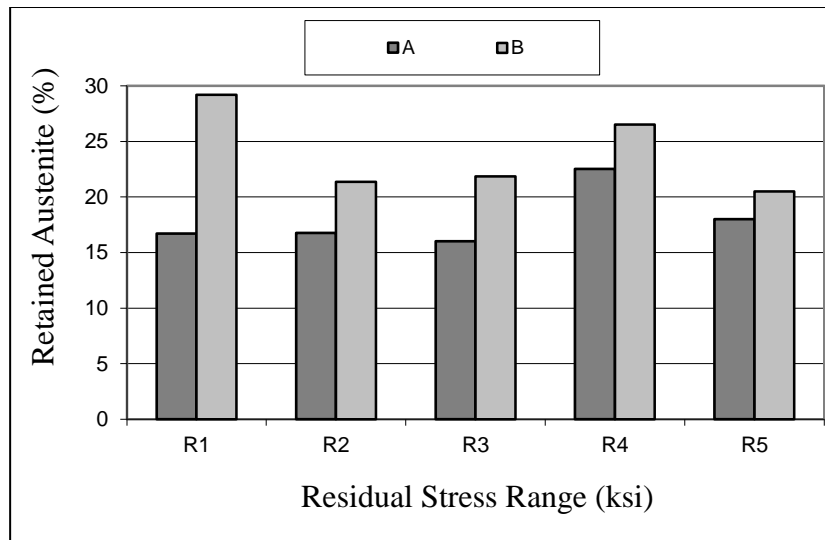


Figure 5.3 Comparison of RA-RS values between laboratories A and B

Figure 5.3 shows that, at the same level of residual compressive stress. Laboratory B consistently reports higher values of RA than laboratory A.

In order to further investigate the relationships between RA and RS, the general relationships between RS (XRD) and RA (XRD) are given in Figures 5.4 (a) & (b) for Laboratories A and B, respectively.

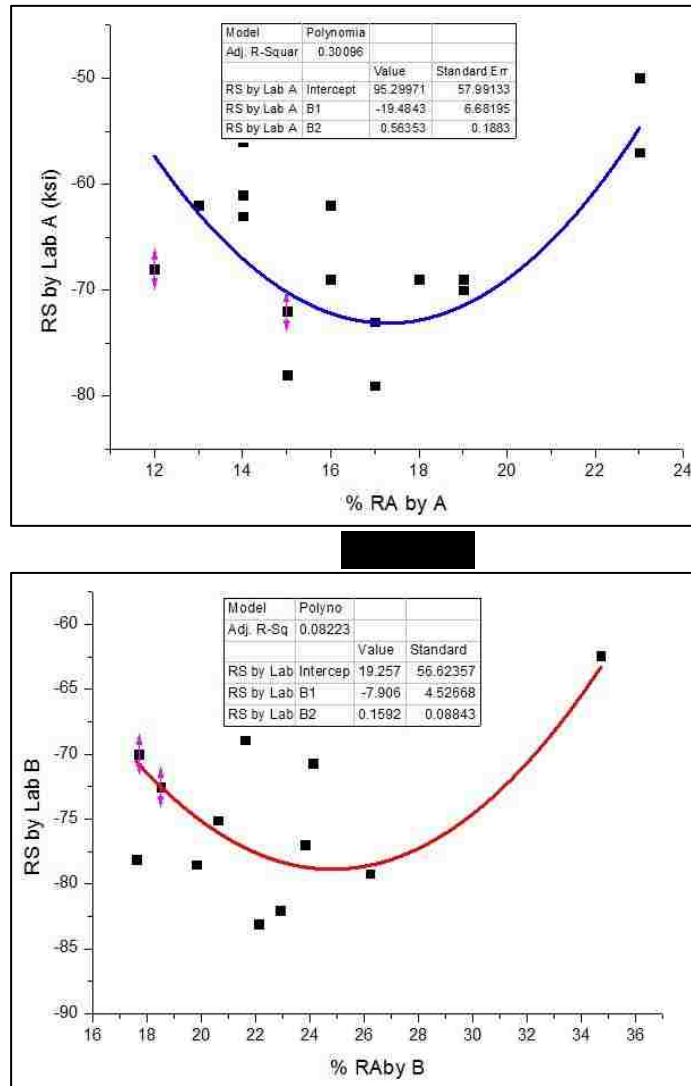


Figure 5.4 Relationships between RA (XRD) and RS (XRD) for (a) Laboratory A (b) Laboratory B.

Figure 5.4 suggests that the relationship between RA and RS, as determined by XRD, is not a linear relationship. Initially, the residual compressive stress increases with an increasing amount of retained austenite, reaching a maximum value, then decreases

with the RA increasing and reaches a maximum. From Figure 5.4, Equation 5.3 (Lab A) & 5.4 (Lab B) were derived for the relationship between RA and RS by XRD:

$$RS_{lab A} = 0.564 * RA_{lab A}^2 - 19.484 * RA_{lab A} + 95.2997 \quad \text{Equation 5.3}$$

$$RS_{lab B} = 0.131 * RA_{lab B}^2 - 6.319 * RA_{lab B} - 2.4556 \quad \text{Equation 5.4}$$

For laboratory A's results, there is a maximum in compressive residual stress when RA is about 18%. For laboratory B, the maximum is when RA is about 25%. However, to test the creditability of the values, a linear regression analysis is necessary. The RS value divided by RA value is used to obtain a ratio for each sample (lab A and B). These RS/RA ratios are given in Table 5.3

Table 5.3 RS/RA ratios for all 18 samples for labs A and B

Spl	RS/RA ratio		Spl	RS/RA ratio		Spl	RS/RA ratio	
	A	B		A	B		A	B
A1	-5.66	-3.95	B1	-2.47	-4.25	C1	-5.20	-5.07
A2	-4.11	-3.96	B2	-3.68	-3.55	C2	-4.29	-4.13
A3	-4.35	-3.64	B3	-3.63	-3.21	C3	-3.83	-3.18
A4	-4.76	-4.70	B4	-2.17	-1.79	C4	-4.64	-3.99
A5	-3.87	-3.58	B5	-3.83	-2.71	C5	-4.31	-3.76
A6	-4.50	-2.93	B6	-5.33	-4.45	C6	-4.80	-3.91

We then obtain a straight line relationship between the ratios for the two laboratories; Figure 5.5:

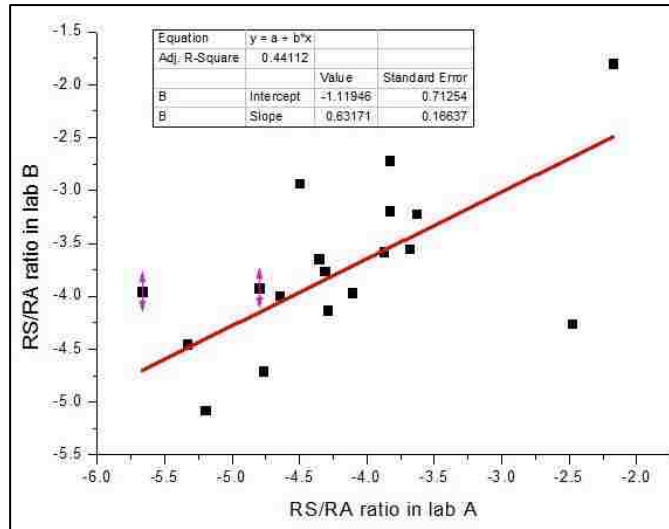


Figure 5.5 Relationships between RS/RA ratios in laboratories A and B

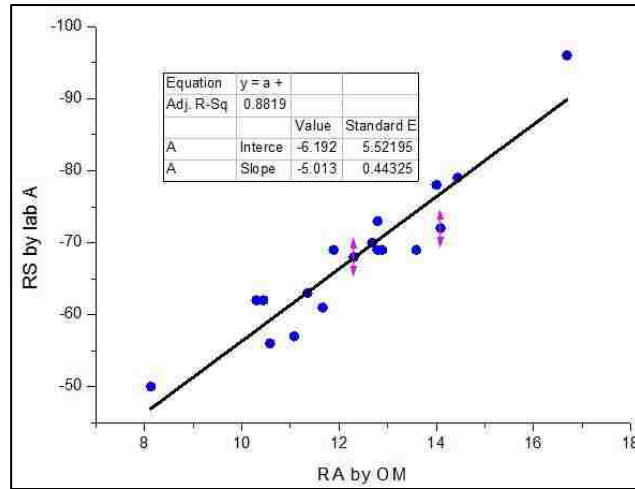
Equation 5.5 gives the ratio relationship between the two laboratories:

$$r_{RS/RA}^A = 0.6317 * r_{RS/RA}^B - 1.1946 \quad \text{Equation 5.5}$$

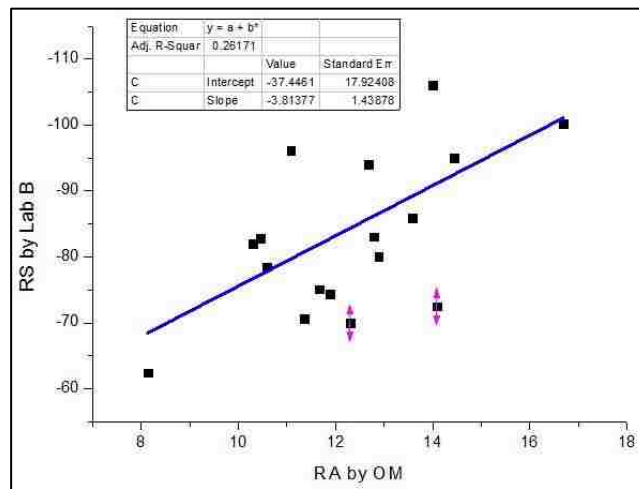
There is a linear relationship although the data correlated only to an R^2 value of 0.44.

5.2 Relationship between RS (XRD) and RA by Optical Microscopy

Using the retained austenite values obtained in our laboratory by image analysis, the relationship between RA (OM) and RS (XRD) from laboratories A and B can be determined and is shown in Figures 5.6 (a) and (b) . The plots reveal an approximately linear relationship between the compressive residual hoop stress and the RA content as measured by the OM. The magnitude of the compressive stress increases with increasing RA content.



(a)



(b)

Figure 5.6 The relationship between RS (XRD) and RA (OM) for RS data obtained in (a) Laboratory A (b) Laboratory B

The relationship between RS (XRD) from two laboratories and RA (OM) is given by Equation 5.6 for laboratory A and Equation 5.7 for laboratory B :

$$RS_{XRD}^A = -5.013 * RA_{OM} - 6.192 \quad \text{Equation 5.6}$$

$$RS_{XRD}^B = -3.813 * RA_{OM} - 37.446 \quad \text{Equation 5.7}$$

where RS_{XRD}^A stands for the RS value obtained by XRD in laboratory A, and RS_{XRD}^B stands for the RS value obtained by XRD in laboratory B.

As noted, the magnitude of the compressive stress with increasing RA content, This is inconsistent with the data in which show an optimum RA content for maximum compressive residual stress: 17% for Lab A, and 26% for Lab B. These RA values are obtained by XRD. It should be pointed out that the maximum RA content measured by OM is around 18%, which is less, or equal to the optimum RA (XRD) content corresponding the maximum RS in Figure 5.4. An assumption has been made that retained austenite may either be harmful or beneficial for the improvement of residual stress distributions. Under a certain amount, or threshold , increasing amounts of RA aid the formation of compressive stress in a nearly linear relationship. Beyond the threshold, any further increase in retained austenite only decreases the compressive stress. Also from the comparison of Fig 5.4, it can be seen that larger grouping islands (found by OM) are the primary indication of RS, the small γ not picked up are not affecting RS.

5.3 Relationship between RA Values Obtained From OM and XRD

The relationship between RA (XRD) and RA (OM) is shown in Figure 5.7. The values of RA (XRD) are taken from laboratory A only. It can be seen that RA (XRD) is generally higher than RA (OM). It is likely due to the fact that some of the “white” retained austenite is “hidden” within the black martensite matrix in the micrographs and was below the white threshold of the image analysis. The RA (XRD) values given in Figure 5.7 are calculated without taking the graphite nodules into account.

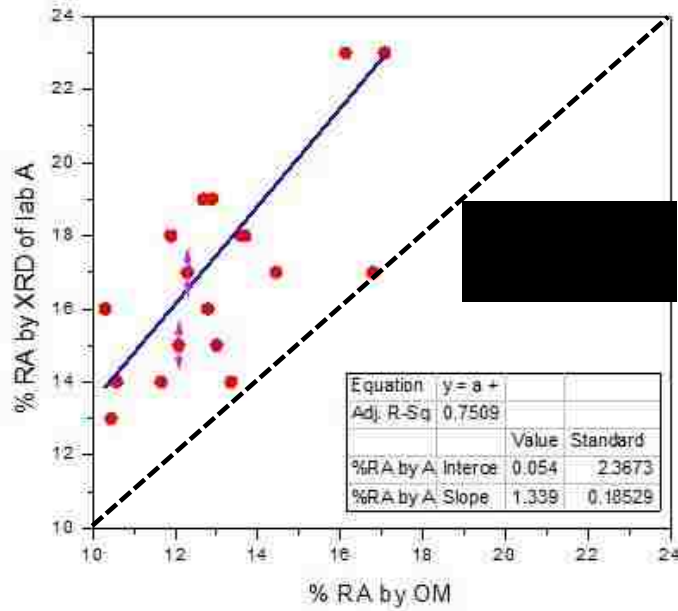


Figure 5.7 Relationship between RA (XRD) and RA (OM)

The relationship between RA (XRD) and RA (OM) can be described by Equation 5.8:

$$Pct_{RA}^{XRD} = 1.339 * Pct_{RA}^{OM} + 0.054 \quad \text{Equation 5.8}$$

where Pct_{RA}^{XRD} stands for the volume percent of RA measured by XRD, Pct_{RA}^{OM} stands for the volume percent of RA measured by OM. The R^2 value is 0.75.

According to ASTM E975 Standard [60], for any retained austenite measurement by XRD, microconstituents such as carbides and graphite should be accounted for prior to the calculation of RA by the “4-peak method”. The graphite content data was obtained by microscopy and image analysis. Equation 3.2 can be written as Equation 5.9 to take the graphite content into consideration:

$$V_{\gamma} = (1 - V_{\text{graphite}}) \cdot \frac{\frac{1}{2} \left(\frac{I_{\gamma(200)}}{R_{\gamma(200)}} + \frac{I_{\gamma(220)}}{R_{\gamma(220)}} \right)}{\frac{1}{2} \left(\frac{I_{\gamma(200)}}{R_{\gamma(200)}} + \frac{I_{\gamma(220)}}{R_{\gamma(220)}} \right) + \frac{1}{2} \left(\frac{I_{\alpha(200)}}{R_{\alpha(200)}} + \frac{I_{\alpha(211)}}{R_{\alpha(211)}} \right)} \quad \text{Equation 5.9}$$

where V_{graphite} is the volume fraction of graphite that we have determined from OM image analysis. Figure 5.8 is a revised plot of RA (XRD) vs. RA (OM), where RA (XRD) is calculated using Equation 5.9. Equation 5.10 describes the revised relationship between RA (XRD) and RA (OM):

$$Pct_{RA}^{XRD} = 1.166 * Pct_{RA}^{OM} + 0.161 \quad \text{Equation 5.10}$$

As already noted, it is believed the fact that RA (XRD) > RA (OM) is because of an inability to identify the retained austenite in a mixed-microstructure (typically martensite-austenite).

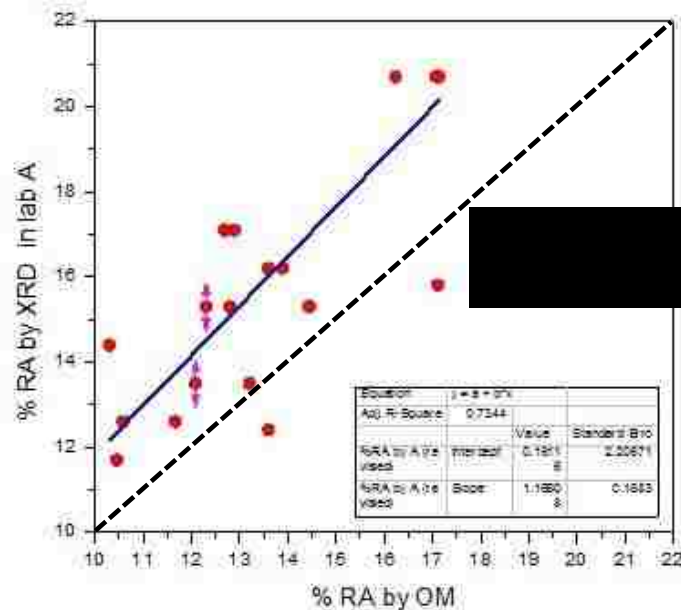


Figure 5.8 RA (XRD), as calculated using Equation 5.9, as a function of RA (OM)

Although the data are now closer to the RA (XRD) = RA (OM) line, RA (XRD) are still higher than RA (OM). The R^2 value is not changed significantly: it is now 0.73.

5.4 Relationship between Hardness and RA content

Table 5.4 summarises the macrohardness data obtained from the Rockwell hardness tests. A comparative value for the as-cast sample is 23 HRC, due to the pearlite-ferrite microstructure which is soft.

Table 5.4 Macrohardness values (HRC) for all the 18 samples.

Sample	Hardness (HRC)	Sample	Hardness (HRC)	Sample	Hardness (HRC)
A1	55.3	B1	57.1	C1	54.7
A2	50.2	B2	50.2	C2	58.3
A3	56.8	B3	58.2	C3	56.0
A4	54.2	B4	49.8	C4	52.3
A5	51.7	B5	54.2	C5	58.4
A6	57.2	B6	61.1	C6	60.2
A(Aver)	54.2	B(Aver)	55.1	C(Aver)	56.1

It can be seen that the samples have hardness values ranging from 49.8 to 61.2, making it useful for such applications as the current application for automotive camshafts. These hardness variations reflect the RA & RS variations seen for the various lobes. Figure 5.9 illustrates the hardness distribution of all 18 samples:

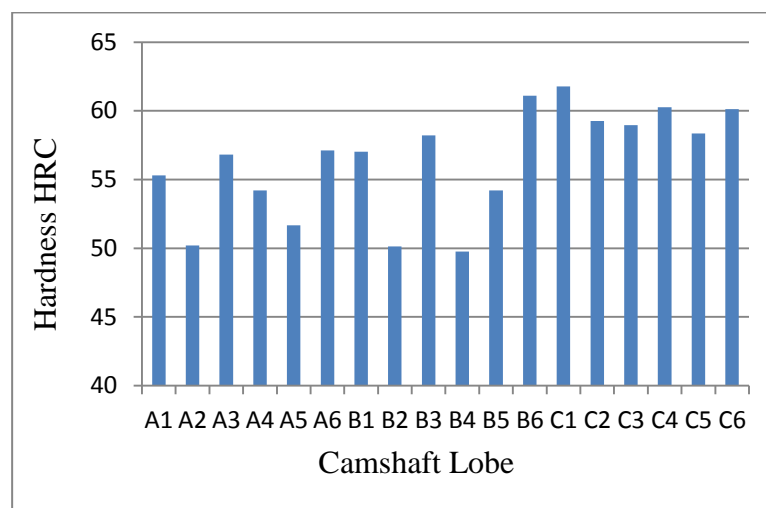


Figure 5.9 Hardness (HRC) of all 18 samples

A comparison of the hardness of the three camshafts is given in Figure 5.10, which calculates an average value from the six lobes. Although the hardness values in different lobes vary from 50 to 60, the average hardness of the three camshafts is almost the same. Camshaft A has the lowest average hardness at 54.2 HRC; camshaft B has a hardness of 55.1 HRC and camshaft C has the highest average hardness of 56.7 HRC. A possible reason why camshaft C has a higher average hardness could be related to what was discussed in section 4.1: It had the lowest amount of retained austenite, and therefore the highest amount of hard martensite.

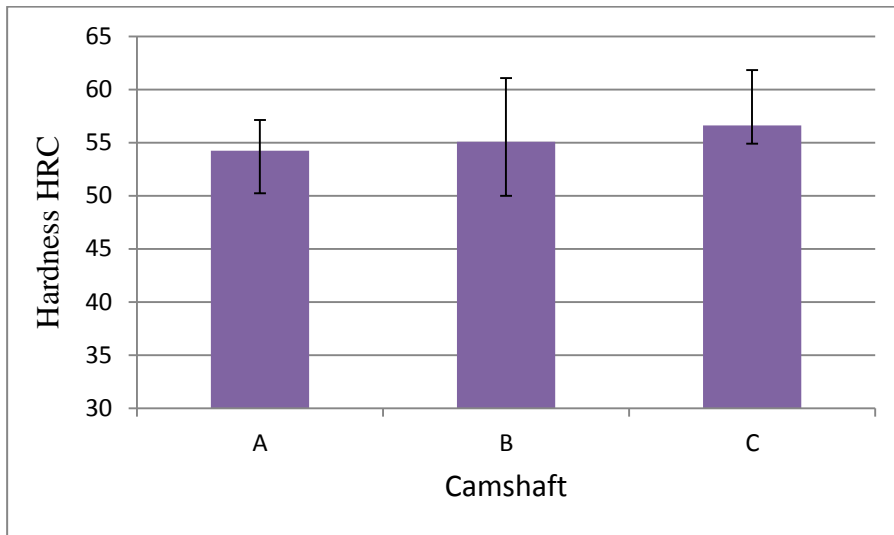


Figure 5.10 Average hardness of camshafts A, B and C

The relationship between hardness and % retained austenite is shown in Figure 5.11. There is a fairly linear, inverse relationship between the hardness level and the % retained austenite.

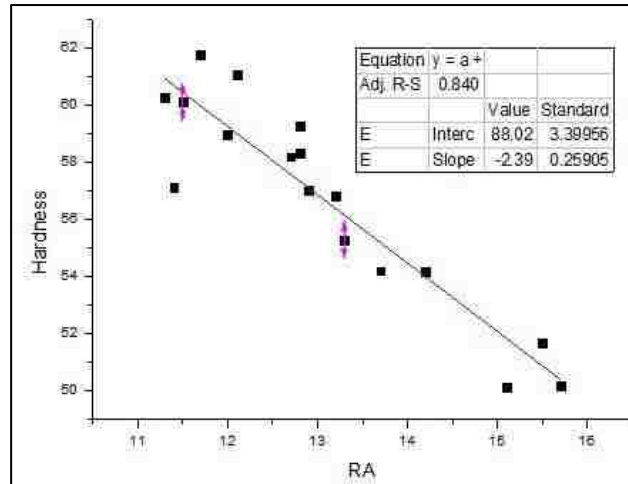


Figure 5.11 Relationship between hardness and % RA

It could be seen that hardness reaches maximum of 62 HRC when RA content is 11%, and decreases to 49 HRC when RA content is around 19 %.The relationship between hardness and RA content is given in Equation 5.9:

$$H = -2.39 * RA + 88.02 \quad \text{Equation 5.9}$$

where **H** is the hardness of the sample, and **RA** stands for the retained austenite content . The R²value is 0.84. Although there is basic a linear relationship, when the RA content exceeds 16%, the hardness trends to a constant value of around 49 HRC.

CHAPTER VI

CONCLUSIONS AND RECOMMENDATIONS

The target application of the induction hardened ductile iron in this research was an automotive camshaft with a desired hardness of 55 HRC. The hardness values of all three camshafts were 55, 55 and 56 HRC. The induction heating process should thus be able to produce camshafts capable of handling high loads and be suitable for large scale manufacturing. Through the determination of retained austenite, residual stress and hardness, the following conclusions could be drawn from this study.

1. The microstructures of as-cast samples consist of mainly lamellar pearlite and nodular graphite surrounded by “bull’s eye” ferrite. However, after the induction heating process, the microconstituents change to mainly martensite with retained austenite, and sometimes pearlite. The retained austenite ranges from 10 % to 30%.
2. Due to the skin effect, electromagnetic ring effect, and electromagnetic proximity effect in the induction hardening process, compressive stress develop at the surface when austenite transforms into martensite. The compressive stresses developed depend on the nature of the hardened case and stresses introduced during quenching. The measured compressive stresses ranged from -70 ksi to -110 ksi.
3. Camshaft C has lower average nodular graphite and lower average retained austenite level than the two other camshafts. A linear relationship between the nodular graphite content and retained austenite was made. However, scatter of data and a multicomponent microstructure makes it difficult to provide a simple cause and effect mechanism.
4. XRD results showed that retained austenite influences the magnitude of the compressive residual stresses. The residual compressive stress first increases with

increasingly retained austenite when the retained austenite content is lower than 18%. However, when the RA content exceeds 18%, the residual compressive stress is decreased.

5. Measurement of the retained austenite and residual stress by XRD by two different laboratories gave different values. The correlation was $R^2=0.32$.
6. Optical Metallography is proven to be an effective way to measure the retained austenite content. Generally, RA contents obtained by OM were noted to increase along with the data obtained by XRD, except RA (XRD) is always higher than RA (OM). This difference is believed to be due to an inability to identify optically the retained austenite in a mixed-microstructure, typically martensite-austenite.
7. ASTM E975 Standard uses a “4-peak method” in measuring the amount of retained austenite for steels. For ductile iron, the amount of nodular graphite must be determined by optical metallography prior to calculating the RA content using XRD. A modified equation is presented, Equation 5.9.
8. The hardness of the induction treated samples decreases with increasing RA contents up to 16%. The relationship is with a R^2 value of 0.75. For RA contents above 16%, the hardness trends to level out at a constant value of around 49 HRC.

6.1 Recommendations for Future Work:

The following work is suggested to further understand and improve the properties of induction hardened ductile iron.

1. The effect of alloying elements should be studied along with the induction heating schedules. Alloying elements such as Cu, Mo, Ni could alter the induction heating response and influence microstructure and, thereby, properties.
2. The effect of induction heating time and heating power on the retained austenite content and residual stress level should be studied.
3. Subsequent heating processes such as tempering should be investigated as a means of improving the mechanical properties.
4. Other mechanical property tests such as the fatigue test, impact toughness and tribology tests should be done to obtain a full view of the influence of retained austenite on the mechanical properties that are relevant to camshaft performance.
5. Microhardness tests should be done in order to identify the influence of different microconstituents such as retained austenite, martensite and pearlite on the mechanical properties.
6. SEM should be done in order to investigate the existence of bainite or ferrite in the induction hardened ductile iron samples. The maximum magnification in optical microscopy is limited to 1000 X, which restricts the microstructural analysis of finer components.
7. The retained austenite and residual stress distribution along the induction hardened ductile iron samples from the surface to the core should be investigated to provide a

robust processing window in instances when RA or RS contents are required to optimize manufacturing process.

8. The measurement of RA and RS on other ductile irons, such as austempered ductile iron, should be included. It will enlarge the database for RA and RS measurement by XRD and OM.

REFERENCES

1. Lyle.R.Jenkins and R.D. Forrest, Ductile Iron, Properties and Selection: Irons, Steels, and High-Performance Alloys, Vol 1, ASM Handbook, ASM International, Materials Park, OH, U.S.A., pp. 33-55, 1990.
2. V.Rudnev, D.Loveless, R.Cook and M.Black, Handbook of Induction heating, Marcel Dekker Inc, New York, U.S.A., pp. 11-14, 2003.
3. H.K.D.H.Bhadeshia, Steel for Bearings, Progress in Materials Science, Vol. 57, pp. 268-435, 2012.
4. Daniel H.Herring, A Discussion of Retained Austenite, Industrial Heating, Vol. 72, no.3, pp. 14-16, March 2005.
5. B.B. Vinokur and A.L.Geller, The Effect of Retained Austenite on Contact Fatigue in Cr-Ni-W Carburized Steel, JOM Journal of the Minerals, Metals and Materials Society, Vol 49, no.9, pp. 69-71, 1997.
6. C.F.Jaczak, J.A.Larson, and S.W.Shin, Retained Austenite and Its Measurements by X-ray Diffraction, Society of Automotive Engineers, Inc., Warrendale, PA, U.S.A, pp. 1-55, 1980.
7. V.M Zinchenko, B.V. Georgievskaya, and V.A. Olovyanishnikov, Effect of Residual Austenite on the Mechanical Properties of Carburized Steels, Metal Science and Heat Treatment, Vol. 9, no. 11-12, pp .919-925, 1987.
8. T. Gnäpel-Herold and A. Creuziger, Diffraction Study of the Retained Austenite Content in TRIP Steels. Materials Science and Engineering: A, Vol. 528, no.10–11, pp. 3594-3600, 2011.
9. B. L. Bramfitt, Arlan O. Benschoter, Metallographer's Guide: Practices and Procedures for Irons and Steels, ASM International, Materials Park, OH, U.S.A. pp. 88-151, 2002.
10. GearsHub, Supplier, Manufacturer and Exporter of Industrial Gears and Custom Made Gears, Available from: <http://www.gearshub.com/ductile-iron-gears.html>. [D.O.A-2 April 2012]
11. B. C. Macdonald and Company, Available from: http://www.bcmac.com/pdf_files/surface%20finish%20101.pdf. [D.O.A-5 May 2012]
12. George T.Eldis, Correlation of Measurements of Retained Austenite in Carburized Steels by X-Ray Diffraction and Quantitative Metallography, Journal of Heat Treating, Vol. 1, no. 3, pp. 3-25, 1980.

13. Wikipedia Foundation, Introduction to Steel, Available from: <http://en.wikipedia.org/wiki/Steel>. [D.O.A-14 April 2012]
- 14 . R.W.K. Honeycombe, H. K. D. H. Bhadeshia, Steels Microstructure and properties, Elsevier, Jordan Hill, Oxford, UK. pp. 33-41, 2006.
15. Erin Boyle, Microstructural Effects on the Mechanical Properties of Carburized Low-Alloy Steels. Mechanical, Automotive and Materials Engineering Department (Master Thesis), University of Windsor, Windsor, pp. 4-102, 2007.
- 16 . G.F Vander Voort, Vac Aero Inc. Martensite & Retained Austenite, Available from: <http://www.vacaero.com/Metallography-with-George-Vander-Voort/Metallography-with-George-Vander-Voort/martensite-and-retained-austenite.html> [D.O.A-1 May 2012]
17. BOC Company, AU:IPRM 2007: Section 8, Available from : <http://www.bocworldofwelding.com.au/media/pdf/WELDING%20CONSUMABLES-Cast%20Iron.pdf> [D.O.A-21 April 2012]
18. S.D. Kiser, P.E., FAWS and M.Northey, Welding Cast Iron, Canadian Welding Association Journal, pp.1-4, 2005.
- 19 . Key to Metals AG. Classification of Cast Iron, Available from: <http://steel.keytometals.com/articles/art63.htm>. [D.O.A-13 April 2012]
20. M. A. Kenawy, A. M. Abdel-Fattah, N. Okasha, M. El-Gazery, Mechanical and Structural Properties of Ductile Cast Iron. Egyptian Journal of Solids, 24(2), pp. 151-159, 2001.
- 21 . A. Leiro, Tribological Studies on Various Materials Under Mixed-Boundary Lubrication Regime (M. A. Sc Thesis), Department of Materials Science, Lulea University of Technology, Lulea, Sweden, 2009.
22. W. D. Callister, Materials Science and Engineering-An Introduction, 7th Edition, York, PA, U.S.A, John Wiley and Sons, pp. 253-360, 2007.
23. K. B. Rundman, "It's About Austenite and Carbon, Mate"- A Story of the Physical Metallurgy of ADI-Part II, 35th Australian Foundry Institute National Conference Proceeding; Adelaide, Australia. pp. 1-10. Nov. 2004.
24. M. A. Y. Gonzalez, Modelling the Microstructure and Mechanical Properties of Austempered Ductile Irons, Department of Materials Science and Metallurgy (PhD Thesis), University of Cambridge, Cambridge, pp. 5-183, 2001.
- 25 . Tanzim Nasir, Design of Heat Treatment for Production of Austempered Ductile Iron (ADI) with Targeted Automotive Applications, Mechanical, Automotive and Materials

Engineering Department(M.A.Sc Thesis), University of Windsor, Windsor, pp. 10-76, 2011.

26. A.P. Druschitz and S.Thelen, Induction Hardened Ductile Iron Camshaft, SAE 2002 World Congress, Reprinted From: Designing and Achieving Lightweight Vehicles, Detroit, MI, U.S.A., 2002.

27. Richard E. Haimbaugh, Practical Induction Heat Treating, ASM International, Materials Park, OH, U.S.A., pp. 3-284. 2001.

28. C.A.Tudbury, Basics of Induction Heating, Rider, New York, U.S.A. pp. 12-19. 1960.

29. A.E. Slukhotskii and S.E Ryskin, Inductors for Induction Heating, Energy Publications, St. Petersburg, Russia, 1974.

30. V.Rudnev and K. Schweigert, Designing Induction Equipment for Modern Forge Shops, Forging, pp. 56-58. 1994.

31. V. Rudnev, Mathematical Simulation and Optimal Control of Induction Heating of Large-Dimensional Cylinders and Slabs, Ph.D Thesis, Department of Electrical Technology, St. Petersburg Electrical Engineering University, Russia, 1986.

32. V. Rudnev, Characteristics of Transverse Electromagnetic Edge Effect in Induction Heating of Magnetic and Nonmagnetic Slabs. The Study of Electrothermal Processes, Cheboscary, Russia, pp. 30-34, 1985.

33. V.Rudnev and R.Cook, Magnetic Flux Concentrators: Myths, Realities and Profits, Metal Heat Treating, pp.31-35, 1995.

34. V.Rudnev, Be Aware of the “Fine Print” in the Science of Metallurgy of Induction Hardening: Part 2, Available From: <http://www.inductoheat.com/pdf/121.pdf> [D.O.A-2 May 2012]

35. C. Walton, Introduction to Heat Treating of Cast Irons, ASM Handbook, Vol.4, Heat Treating, ASM International, Materials Park, OH, U.S.A., 1991.

36. R.Ruffini, Production and Concentration of Magnetic Flux for Eddy Current Heating Applications, Report presented to the 1992 International Federation of Heat Treatment and Surface Engineering, Beijing, China, 1993.

37. Gear Import Company in India, Available From: <http://www.indiabizclub.com/> [D.O.A-2 May 2012]

38. Engineering Capacity Website, Available From: <http://www.engineeringcapacity.com/features101/treatments/hardening-partnership>. [D.O.A-2 May 2012]

39. Speedway Motors Company, Available From: <http://www.speedwaymotors.com/chevy-performance-engine-block-th.html>[D.O.A-2 May 2012]
40. Motorator- Yours to build Company, Available From: <http://www.motorator.com/blog/mopar/lunati-vooodoo-hemi-5-7-and-6-1-cams>[D.O.A-2 May 2012]
- 41 . V.I. Rudnev, Induction Hardening Cast Iron, Heat Treating Progress, ASM International, Materials Park, OH, U.S.A., 2003.
- 42 .Ductile Iron Society, Heat Treatment, Section VII, Available From: <http://www.ductile.org/didata/pdf/data7.pdf>. [D.O.A-15 April 2012]
43. Robert Bigge, Tramp Elements in Grey and Ductile Iron, Iron Casting Research Institute, pp. 3-12. 2010.
44. G.E. Totten (Editor), Steel Heat Treatment Handbook, 2nd Edition, Vol 1. CRC Press- Taylor and Francis, 6000 Broken Sound Parkway NW, Boca Raton, FL, pp. 1-144. 2006.
- 45 . K. Ogawa, S. Kajiwara, Basic Differences Between Martensitic and Bainitic Transformation Revealed by High-Resolution Electron Microscopy, Material Science and Engineering, A438 (440), pp. 91-94, 2006.
46. Gall, K., Lim, T.J., McDowell, D.L., Sehitoglu, H., Chumlyakov, Y.I.. The Role of Intergranular Constraint on the Stress-induced Martensitic Transformation in Textured Polycrystalline NiTi. Int. J. Plasticity 16 (10–11), pp. 1189–1214, 2000.
47. Levitas, V.I, Thermomechanical Theory of Martensitic phase Transformations in Inelastic Materials. Int. J. Solids Structures 35 (9–10), pp. 889–940, 1998.
48. G. Krauss, Martensitic Transformation, Structure and Properties in Hardenable Steels, in Hardenability Concepts with Applications to Steel, D.V. Doane and J.S. Kirkaldy, eds., AIME, Warrendale, PA, pp. 229-248, 1978.
49. J. Pacyna, Retained Austenite in the Cracking Process of Steel on the Working Rolls of the Cold Sheet Rolling Mill, Steel Research 63, pp. 500-503.1992.
50. Creuziger A, Foecke, Transformation Potential Predictions for the Stress-induced Austenite to Martenite Transformation in Steel. Acta Materialia, 58:85-91, 2010.
51. Wang X D, Huang B X, Rong Y H, et al. Microstructures and Stability of Retained Austenite in TRIP Steels. Materials Science and Engineering A, 438-440:300-305, 2006.

52. Bhadeshia HKDH. Carbon Content of Retained Austenite in Quenched Steels. *Metal Science*, 17(March):151–2. 1983.
53. Kalish D, Cohen M. Structural Changes and Strengthening in the Strain Tempering of Martensite. *Materials Science and Engineering* 6:156–66. 1970.
54. B.D. Cullity, *Elements of X-Ray Diffraction*, Second Edition, Addison-Wesley Publishing Company, Inc., U.S.A., pp. 447-477, 1978.
55. W. Bowen, *X-Ray Diffraction – Microstructural Characterisation*, E. Metcalfe (Editor), The Institute of Metals, U.K, pp. 227-302, 1988.
56. I.C. Noyan and J.B. Cohen, *Residual Stress: Measurement by Diffraction and Interpretation*, Springer-Verlag, New York, U.S.A., pp. 4-7, 75-130, 1986.
57. J.A. Pineault, M. Belassel, and M.E. Brauss, “X-Ray Diffraction Residual Stress Measurement in Failure Analysis”, *ASM Handbook Vol. 11 – Failure Analysis and Prevention*, W.T. Becker and R.J. Shipley (Editors), ASM International, Materials Park, OH, U.S.A., pp. 484-497, 2002
58. J. Pineault, M. Belassel, M. Brauss, and J. Ladouceur, *Mapping Residual Stress Gradients in Automotive Components via X-Ray Diffraction*, SP-2094: *Experiments in Automotive Engineering*, Paper No. 2007-01-0802, SAE International, Warrendale, PA, U.S.A., pp. 23-26, 2007
59. M. Belassel, J. Pineault, and M.E. Brauss, *Review of Residual Stress Determination and Exploitation Techniques Using X-ray Diffraction Method*, *Materials Science Forum*, Vol. 524-525, pp. 229-234, 2006.
60. “ASTM E975-03 Standard Practice for X-Ray Determination of Retained Austenite in Steel with Near Random Crystallographic Orientation”, ASTM International, West Conshohocken, PA, U.S.A., 2008.
61. C.F. Jaczak, J.A. Larson, and S.W. Shin, *Retained Austenite and Its Measurements by X-Ray Diffraction*, Society of Automotive Engineers, Inc., Warrendale, PA, U.S.A., pp. 1-55, 1980.
62. B.L.Averbach and M.Cohen: *Trans. AIME*, Englewood, CO, U.S.A. vol. 176, pp.401-15, 1948.
63. J. A. Klosterman and W. G. Burgers: *Acta Metall*, Elsevier, vol. 12, pp. 355-362, 1964.
64. D.Kirk, *Residual Stress and Retained Austenite in Shot Peened Steels*, 1st International Conference on Shot Peening, Pairs, France, 1981.

65. M. Tisza, Physical Metallurgy for Engineers, ASM International, Materials Park, OH, pp. 338, 2001.
66. “ASTM E915-10 Standard Test Method for Verifying the Alignment of X-Ray Diffraction Instrumentation for Residual Stress Measurement”, ASTM International, West Conshohocken, PA, U.S.A., 2010.
67. “ASTM E1245-03 Standard Practice for Determining the Inclusion or Second-Phase Constituent Content of Metals by Automatic Image Analysis”, ASTM International, West Conshohocken, PA, U.S.A., 2008.
68. T.W.Curry, Production of Ductile Iron Castings, Metals Handbook, Vol 5: Forging and Casting, 8th edition, American Society for Metals, Metals Park, Ohio, U.S.A., pp. 373-374, 1970.

VITA AUCTORIS

NAME	Hao Ma
PLACE OF BIRTH	Suzhou, China
DATE OF BIRTH	July 18 th , 1987
EDUCATION	High School Diploma (HSD) Xuzhou No.1 Middle School Jiangsu, China 2005 Bachelor of Engineering Chemistry and Chemical Engineering Nanjing University of Technology Jiangsu, China 2009 Masters of Applied Science Engineering Materials University of Windsor Windsor, Ontario 2012

PUBLICATIONS AND PRESENTATIONS

Publications

Hao Ma, Randy J.Bowers, Derek O. Northwood, Xichen Sun and Peter J.Bauerle, Residual Stress and Retained Austenite in Induction Hardened Ductile Iron Camshaft, WIT Transactions of Engineering Science, TBA.

Presentations

“Residual Stress and Retained Austenite in Induction Hardened Ductile Iron Camshaft”, Hao Ma, R.J. Bowers, D.O.Northwood, X. Sun and P.Bauerle. Presented at 4th International Conference on Tribology and Design, Kos, Greece, 3-5 September, 2012.